1988SSRv...48..195D

COMPUTER MODELING OF TEST PARTICLE ACCELERATION AT OBLIQUE SHOCKS

ROBERT B. DECKER

Applied Physics Laboratory, The Johns Hopkins University, Laurel, Maryland 20707-6099, U.S.A.

(Received 18 July, 1988)

Abstract. We review the basic techniques and results of numerical codes used to model the acceleration of charged particles at oblique, fast-mode, collisionless shocks. The emphasis is upon models in which accelerated particles (ions) are treated as test particles, and particle dynamics is calculated by numerically integrating along exact phase-space orbits. We first review the case where ions are sufficiently energetic so that the shock can be approximated by a planar discontinuity, and where the electromagnetic fields on both sides of the shock are defined at the outset of each computer run. When the fields are uniform and static, particles are accelerated by the scatter-free drift acceleration process at a single shock encounter. We review the characteristics of scatter-free drift acceleration by considering how an incident particle distribution is modified by interacting with a shock. Next we discuss drift acceleration when magnetic fluctuations are introduced on both sides of the shock, and compare these results with those obtained under scatter-free conditions. We describe the modeling of multiple shock encounters, discuss specific applications, and compare the model predictions with theory. Finally, we review some recent numerical simulations that illustrate the importance of shock structure to both the ion injection process and to the acceleration of ions to high energies at quasi-perpendicular shocks.

Table of Contents

Space Science Reviews **48** (1988) 195–262.

1988SSRv...48..195D

1. Introduction

This review is concerned primarily with particle acceleration at collisionless, oblique, fast-mode shocks. The emphasis is upon results from computer models in which accelerated particles are treated as test particles and particle dynamics is calculated by numerically integrating along exact phase-space trajectories. With the exception of Section 5, we concentrate on the situation where particles are sufficiently energetic so that the shock can be treated as a discontinuity, and where the electromagnetic fields on both sides of the shock are defined at the outset of each computer run.

The acceleration of energetic ions and electrons continues to attract considerable theoretical and observational attention, as is evident in proceedings from several recent conferences, including the past few International Cosmic-Ray Conferences, the 1984 Napa conference on Collisionless Shocks in the Heliosphere, the 1987 Balatonfüred conference on Collisionless Shocks, and the Sixth International Solar Wind Conference. Particle acceleration at shocks has been studied using a variety of techniques. These include: (i) numerical simulations that incorporate the self-consistent coupling between the plasma particles and the electromagnetic fields of the shock transition; (ii) computer models that involve orbit integrations of test particles at shocks with transitions that are either infinitesimally thin, or else have a more complicated profile; (iii) Monte-Carlo methods in which particle behavior in field fluctuations (e.g., pitch angle scattering) is modeled through use of a scattering law; and (iv) theoretical analysis to solve the appropriate equations for the particle distribution function, wave amplitude, etc., under various boundary conditions. Each approach has its own advantage and disadvantage, and its own realm of applicability. For example, in proceeding from (i) to (iv), information on the microphysics is progressively lost, but the scale size, duration and energy of phenomena that can be covered generally increases.

Theoretical treatments of shock acceleration have been covered elsewhere, and the reader is referred to several reviews on the subject (e.g., Blandford and Eichler, 1987; Forman and Webb, 1985; Ptuskin, 1985; Drury, 1983; Axford, 1981; Toptyghin, 1980). The techniques and results of Monte-Carlo models of acceleration at parallel shocks have also been dealt with elsewhere (e.g., Ellison, 1981; Ellison and Eichler, 1984; Kirk and Schneider, 1987; Blandford and Eichler, 1987). Relevant references to plasma simulations concerned with particle acceleration can be found in Section 5 of this review.

The contents of this review are summarized as follows. Section 2 is a description of the shock geometry, various useful reference frames, and terminology that is used in subsequent sections. We also write down the magnetic Rankine–Hugoniot conditions and describe how they are used to calculate the jump in plasma parameters across the shock.

Section 3 is a review of the techniques and predictions of scatter-free drift acceleration (also known as shock drift acceleration or SDA) after a single encounter with a shock. Our purpose here was to collect the various bits and pieces from earlier work, much of which is contained in conference proceedings or theses, and develop a coherent picture.

We summarize how results from the modeling compare with theoretical expressions based upon magnetic moment conservation, and describe briefly how features of both the numerical and theoretical work compare with some observations. We do not make any detailed comparisons with the observations. Observations of accelerated particle distributions at planetary bow shocks and interplanetary shocks have been reviewed elsewhere (e.g., Scholer, 1985, 1988; Krimigis, 1987; Armstrong *et al.*, 1985; Lee, 1983).

In Section 4 we discuss effects produced when fields of transverse magnetic fluctuations are superposed upon the mean fields on both sides of the shock. We describe how fluctuations with specified statistical properties are synthesized, and show how single-encounter drift acceleration is modified by the presence of the fluctuations. For longer run times, a small fraction of the injected particles encounter the shock many times, and are accelerated to high energies by both the drift and first-order Fermi processes. This code enables one to study time-dependent shock acceleration when the angle θ_1 between the shock normal and upstream magnetic field, the level of magnetic fluctuations, and the energy of injected particles can assume a range of values. We describe applications of the multiple-encounter code to ion acceleration at shocks in the lower solar corona and in interplanetary space. We illustrate how both the acceleration rate and drift distance along the shock increase as θ_1 increases. Finally, we compare the modeled energy distributions with predictions based upon time-dependent diffusive shock acceleration theory.

Section 5 contains summaries of three numerical simulations to illustrate the importance of shock structure to both the ion injection process and to the acceleration of ions to high energies at quasi-perpendicular shocks. The examples covered include the drift acceleration of low energy ($\gtrsim 1$ keV) protons, $\mathbf{V}_p \times \mathbf{B}$ acceleration at shocks with $\theta_1 \lesssim 90°$, and ion injection and acceleration associated with head-on collisions of two supercritical shocks. Section 6 contains a brief summary and partial list of remaining problems.

2. Conditions at the Shock

2.1. GEOMETRY AND USEFUL REFERENCE FRAMES

Computer models dealing with test particle acceleration to high energies at oblique, fast-mode, collisionless shock waves have concentrated upon shocks that are locally planar, so that $r_g \ll R_s$, where r_g is the particle gyroradius and R_s the shock radius of curvature. It has proven useful in this situation to introduce four reference frames from which to view the acceleration process. First, let $K[\hat{x}, \hat{y}, \hat{z}]$ denote a coordinate system fixed with the shock, such that unit vector $\hat{x} = -\hat{n}$ ($\hat{n}$ = shock normal), and the shock discontinuity coincides with the $(y - z)$-plane, thereby separating the region upstream ($x < 0$, subscript 1) from that downstream ($x > 0$, subscript 2) (Figure 1(a)). Relative to shock frame K, the plasma bulk flow velocities are

$$\mathbf{U}_i = (U_{ix}, 0, U_{iz}) = (U_i \cos\delta_i, 0, U_i \sin\delta_i)\,, \tag{1}$$

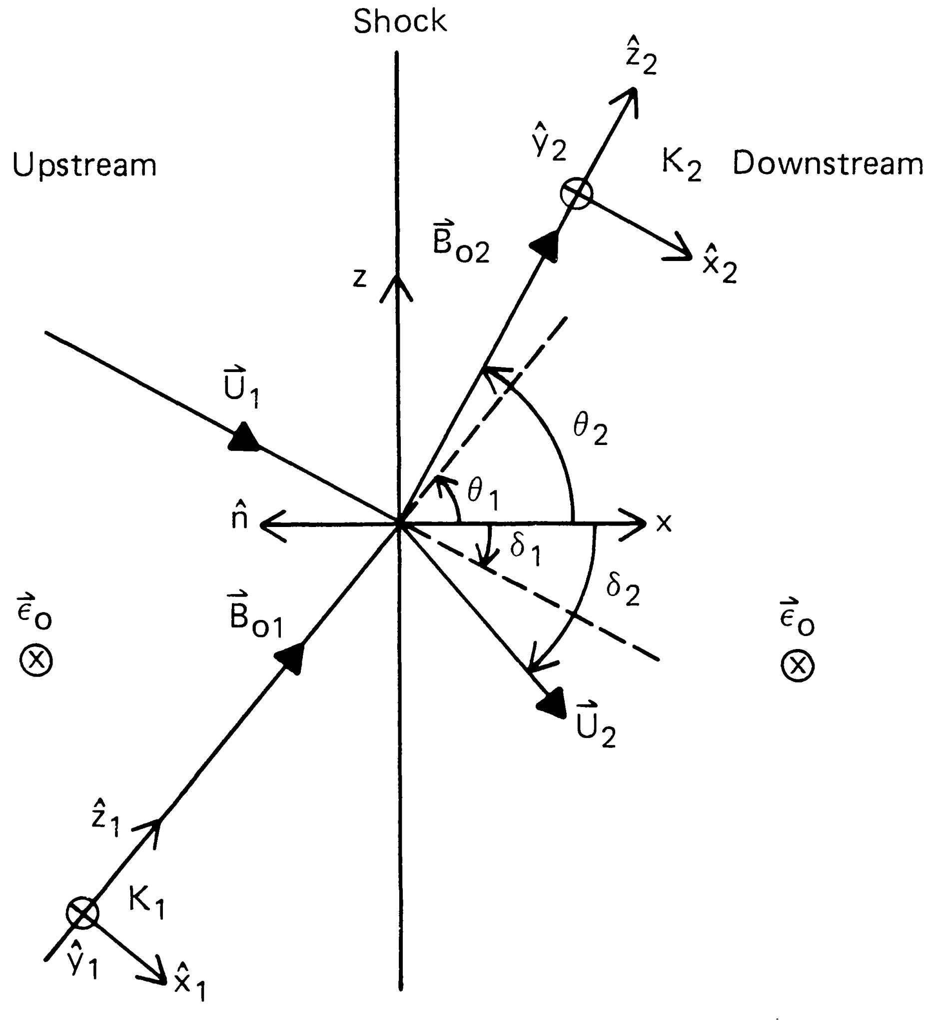

(a) Shock frame K

Fig. 1. (a) Definition of parameters for constant and uniform conditions in shock frame K. Frames K_1 and K_2 are fixed in the upstream and downstream plasmas. (b) de Hoffmann-Teller frame K' where plasma flow is parallel to magnetic field on both sides of shock.

where $-\pi/2 < \delta_i < \pi/2$ ($i = 1$ or 2). For generality, we allow the inflow velocity to have a component (U_{1z}) parallel to the shock surface, as is the case, for example, at planetary bow shocks and corotating shocks.

Next, we denote by $K_i[\hat{x}_i, \hat{y}_i, \hat{z}_i]$ the two coordinate systems comoving with the respective flow velocity $\mathbf{U}_i$, with the constant and uniform magnetic field in frame K_i given by

$$\mathbf{B}_{0i} = (B_{0i_x}, 0, B_{0i_z}) = (B_{0i}\cos\theta_i, 0, B_{0i}\sin\theta_i)\,, \tag{2}$$

where $-\pi < \theta_i \leq \pi$. For nonrelativistic plasma flows $[(U_i/c)^2 \ll 1]$, which are assumed throughout this paper, the fields in (2) transform virtually unchanged from frame K_i to frame K. The assumption of infinite electrical conductivity implies that any static electric fields in frame K_i must vanish, so that in frame K,

$$\varepsilon_{0i} = -\mathbf{U}_i \times \mathbf{B}_{0i}/c \equiv \varepsilon_0 \tag{3}$$

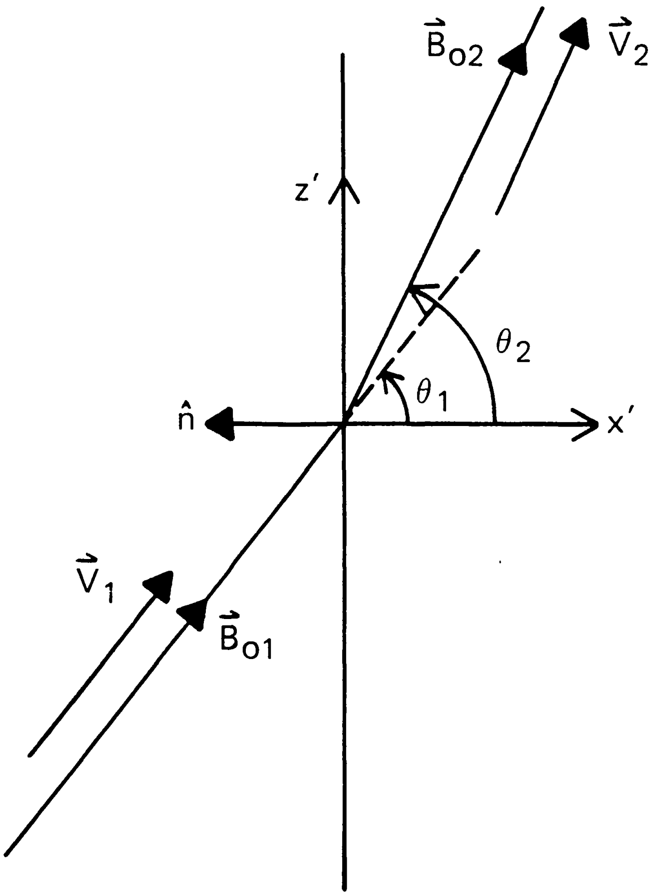

(b) deHoffmann-Teller frame K′

is the constant convection electric field that by Faraday's law ($\nabla \times \varepsilon_0 = 0$) must be continuous across the shock.

Finally, we define the coordinate system $K'[\hat{x}', \hat{y}', \hat{z}']$ such that in frame K' the shock is stationary (as in frame K), but plasma flow is parallel to the magnetic field on both sides of the shock, so the electric field $\varepsilon = 0$ upstream and downstream (Figure 1(b)). Frame K' is often called the de Hoffmann–Teller or HT frame in reference to the early work of de Hoffmann and Teller (1950) on MHD shocks. Relative to shock frame K, the velocity of frame K' is $\mathbf{V}' = -\hat{z}U_1 \sin(\theta_1 - \delta_1) \sec\theta_1$, which, as observed from frame K, is simply the velocity at which the intersection point of a given field line and the shock moves along the shock surface. The transformation from the shock frame K to frame K' is possible provided that V' is subluminal, i.e., $V' < c$, or $\theta_1 < \tan^{-1}[(c/U_1)\sec\delta_1 + \tan\delta_1]$. Otherwise, if V' is superluminal, i.e., $V' > c$, it is impossible to eliminate the electric field on both sides of the shock simultaneously, but it is possible to transform to a frame where $\mathbf{B}_{01}$ and $\mathbf{B}_{02}$ are parallel to the shock surface, i.e., where the shock is perpendicular (e.g., Hudson, 1965). Relative to an observer in K', the plasma flow velocities are

$$\mathbf{V}_i = \hat{x}U_i \cos\delta_i + \hat{z}U_i \tan\theta_i \cos\delta_i = \pm\hat{B}_{0i} U_i \sec\theta_i \cos\delta_i\,, \qquad (4)$$

1988SSRv...48..195D

where $\hat{B}_{0i}$ is the unit vector along $\mathbf{B}_{0i}$, and the upper (lower) sign is for $B_{0x} > 0$ (< 0). Thus, relative to plasma frame K_i, the velocity of frame K' is $-\mathbf{V}_i$, so, one can transform between frames K_i and K' by sliding along $\mathbf{B}_{0i}$ at speed

$$V_i = |\mathbf{V}_i| = U_i \sec\theta_i \cos\delta_i \tag{5}$$

provided that $V_i < c$, or $\theta_i < \cos^{-1}[(U_i/c)\cos\delta_i]$. Note that because $\mathbf{V}_i$ is parallel to the magnetic field, the field's magnitude and direction on either side of the shock does not change when transforming from K_i to K'. We assume that at time $t = 0$, i.e., when a particle is injected at the shock, the origins of the various reference frames coincide, with the unit vectors of the K and K' systems parallel, and those of the K_i systems oriented with respect to $\mathbf{B}_{0i}$ such that $\hat{z}_i = \hat{B}_{0i}$, $\hat{y}_i = \hat{y}$, and $\hat{x}_i = \hat{y}_i \times \hat{z}_i$ (see Figure 1(a)).

2.2. MHD RANKINE–HUGONIOT CONDITIONS

When a charged particle's energy is sufficiently large so that the condition $r_g \gg L_s$ is satisfied, where L_s is the scale length of the shock transition, the fluctuating electromagnetic fields in the shock transition represent a small perturbation on the particle's orbit, and the particle's dynamics is dominated by the macroscopic fields on either side of the shock. When static and uniform conditions prevail in the upstream plasma, the MHD Rankine–Hugoniot (RH) conditions enable one to calculate the macroscopic plasma properties downstream of the shock given those upstream, even if one's knowledge of the complex dissipative processes occurring within the shock transition itself is incomplete. The RH conditions originate from Maxwell's equations and the conservation form of the one-fluid MHD equations that express the conservation of mass, momentum, and energy. Under steady-state conditions in shock frame K when quantities vary with coordinate x only (as in Figure 1(a)), these equations can be integrated across the shock to yield (e.g., Tidman and Krall, 1971; Boyd and Sanderson, 1969) (subscript 0 has been dropped on $\mathbf{B}$ and $\boldsymbol{\varepsilon}$)

$$[B_x]_1^2 = 0\,, \tag{6a}$$

$$[\rho U_x]_1^2 = 0\,, \tag{6b}$$

$$[\rho U_x^2 + P + B_z^2/8\pi]_1^2 = 0\,, \tag{6c}$$

$$[\rho U_x U_z - B_x B_z/4\pi]_1^2 = 0\,, \tag{6d}$$

$$[U_z B_x - U_x B_z]_1^2 = 0\,, \tag{6e}$$

$$\left[\left(\frac{\gamma_r}{\gamma_r - 1}\right) P U_x + \tfrac{1}{2}\rho U_x U^2 + U_x B^2/4\pi - B_x(U_x B_x + U_z B_z)/4\pi\right]_1^2 = 0\,, \tag{6f}$$

where the difference operator $[\ \ ]_1^2$ is defined such that $[F]_1^2 = F_2 - F_1$, and the ideal MHD approximations of an isotropic thermal pressure, zero heat flux, and neglect of the electric field in the electromagnetic stress tensor have been made. Equations (6a) and (6e) follow from $\nabla \cdot \mathbf{B} = 0$ and $\nabla \times \boldsymbol{\varepsilon} = 0$, and express the conservation of the normal component of $\mathbf{B}$ and tangential component of $\boldsymbol{\varepsilon}$ across the shock. The variables ρ,

$P = nk_B(T_e + T_i)$ and $\gamma_r P/(\gamma_r - 1)$ are the mass density, thermal pressure, and enthalpy, respectively, where n = number density, T_e = electron temperature, T_i = ion temperature, and k_B = Boltzmann constant. Also, $U^2 = U_x^2 + U_z^2$ and $B^2 = B_x^2 + B_z^2$. For given values of the upstream parameters U_{1x}, U_{1z}, B_{1x}, B_{1z}, P_1, and ρ_1, Equations (6) represent six equations to solve for the corresponding downstream parameters for a specified ratio of specific heats γ_r.

Equations (6) can be manipulated in a number of ways, depending upon how one chooses to represent the upstream parameters. One method is to use (6b) to define the shock strength

$$r = \rho_2/\rho_1 = U_{1x}/U_{2x} . \tag{7}$$

The upstream Alfvén Mach number is defined by

$$M_{\mathrm{A}1} = U_1/v_{\mathrm{A}1} , \tag{8}$$

where $v_{\mathrm{A}1} = B_1/(4\pi\rho_1)^{1/2}$ is the upstream Alfvén speed, and the upstream plasma beta by

$$\beta_1 = P_1/(B_1^2/8\pi) . \tag{9}$$

Equations (6) can be combined to yield a quartic equation for r. (This is most easily accomplished by first transforming these equations to the K' frame, in which case Equation (6e) vanishes (e.g., Helfer, 1952)). The quartic can be factored into a cubic times the factor $(r - 1)$, whose vanishing implies the solution for no shock, $r = 1$. We are interested in the shock solution, i.e., $r > 1$, since shocks are compressive, which implies that the cubic must vanish:

$$a_3 r^3 + a_2 r^2 + a_1 r + a_0 = 0 , \tag{10}$$

where

$$a_3 = [(\gamma_r - 1)M_{\mathrm{A}1}^2 + \gamma_r \beta_1 \cos^2\theta_1] \cos^2\theta_1 , \tag{11a}$$

$$a_2 = \{[2 - \gamma_r(1 + \cos^2\theta_1)]M_{\mathrm{A}1}^2 - [1 + \gamma_r(1 + 2\beta_1)] \cos^2\theta_1\} M_{\mathrm{A}1}^2 \cos^2\delta_1 , \tag{11b}$$

$$a_1 = [(\gamma_r - 1)M_{\mathrm{A}1}^2 + \gamma_r(1 + \cos^2\theta_1 + \beta_1) + 2\cos^2\theta_1](M_{\mathrm{A}1}^2 \cos^2\delta_1)^2 , \tag{11c}$$

$$a_0 = -(\gamma_r + 1)(M_{\mathrm{A}1}^2 \cos^2\delta_1)^3 , \tag{11d}$$

where $M_{\mathrm{A}1}\cos\delta_1$ is the Alfvén Mach number for the normal component of upstream flow $U_{1x} = U_1 \cos\delta_1$. The shock strength is bounded by $1 \le r \le (\gamma_r + 1)/(\gamma_r - 1)$, which for the adiabatic value $\gamma_r = \frac{5}{3}$ yields $1 \le r \le 4$. After specifying the upstream parameter set $(U_{1x}, U_{1z}, B_{1x}, B_{1z}, P_1, \rho_1)$ or, equivalently, the set $(U_1, \delta_1, B_1, \theta_1, M_{\mathrm{A}1}, \beta_1)$, one evaluates the coefficients (11), solves (10) for the properly bounded root r, and obtains the downstream parameters using relations (6a), (7), and

$$B_{2z} = \frac{M_{\mathrm{A}1}^2 \cos^2\delta_1 - \cos^2\theta_1}{M_{\mathrm{A}1}^2 \cos^2\delta_1 - r\cos^2\theta_1} r B_{1z} = \xi r B_{1z} , \tag{12}$$

1988SSRv...48..195D

$$U_{2z} = U_{1z} + \frac{(r-1)\cos\theta_1 \sin\theta_1}{M_{\mathrm{A}1}^2 \cos^2\delta_1 - r\cos^2\theta_1} U_{1x}\,, \tag{13}$$

$$P_2 = P_1\{1 + [2(r-1)M_{\mathrm{A}1}^2 \cos^2\delta_1 + (1 - \xi^2 r^2) r \sin^2\theta_1]/r\beta_1\} \tag{14}$$

with ξ defined by (12). One can easily verify using (6a), (7), (12), and (13) that $\boldsymbol{\varepsilon}_1 = \boldsymbol{\varepsilon}_2$. Of the three oblique shock solutions permitted by the RH conditions, one, the intermediate mode shock, is noncompressive ($r = 1$), and the other two, the fast and slow mode shocks, are compressive. Upstream of a fast (slow) mode shock, $U_{1x} \geq c_{1F} (c_{1S} \leq U_{1x} < c_{1I})$, while downstream, $c_{2I} < U_{2x} \leq c_{2F} (U_{2x} \leq c_{2S})$ (e.g., Colburn and Sonett, 1966). Here, c_F and c_S are the fast and slow mode speeds of small-amplitude MHD waves, and are given by

$$\begin{matrix} c_F^2 \\ c_S^2 \end{matrix} = \tfrac{1}{2}\{(v_{\mathrm{A}}^2 + v_S^2) \pm [(v_{\mathrm{A}}^2 + v_S^2)^2 - 4v_{\mathrm{A}}^2 v_S^2 \cos^2\theta]^{1/2}\}\,, \tag{15}$$

where $v_{\mathrm{A}} = B/(4\pi\rho)^{1/2}$ and $v_S = (\gamma_r P/\rho)^{1/2}$ are the Alfvén and sound speeds, respectively, and θ is the angle between the direction of wave propagation and $\mathbf{B}$. The speed $c_I = v_{\mathrm{A}} \cos\theta$ is the intermediate mode speed. One can show that across a fast (slow) mode shock, $B_{2z}/B_{1z} > 1$ (< 1), and since $B_{2x} = B_{1x}$, the field is refracted towards (away from) the shock surface and increased (decreased) in magnitude (e.g., Siscoe, 1983).

The many interesting physical implications contained in the RH conditions have been discussed in detail and graphically displayed elsewhere (e.g., Colburn and Sonett, 1966; Tidman and Krall, 1971; Kantrowitz and Petschek, 1966; Kennel *et al.*, 1985; Papadopoulos, 1985). Among those of interest for oblique, compressive shocks are the following (with $\delta_1 = 0$ for illustration). (1) Across either a fast or slow mode shock, $\hat{n}$, $\mathbf{B}_1$ and $\mathbf{B}_2$ are coplanar, i.e., $(\mathbf{B}_1 \times \mathbf{B}_2)\cdot\hat{n} = 0$ (coplanarity theorem). (2) For strong shocks, i.e., as $M_{\mathrm{A}1}^2 \to \infty$, $B_{2z}/B_{1z} = U_1/U_2 = r = (\gamma_r + 1)/(\gamma_r - 1)(= 4$ for $\gamma_r = \frac{5}{3})$, and $P_2 = P_1[1 + 2\gamma_r M_{S1}^2/(\gamma_r + 1)]$, where $M_{S1} = U_1/v_{S1}$ is the sonic Mach number. (3) For a parallel ($\theta_1 = 0°$), non-switch on (i.e., $M_{\mathrm{A}1}^2 \cos^2\delta_1 - r\cos^2\theta_1 \neq 0$, or, $U_{2x} \neq v_{\mathrm{A}2_x}$) shock, the magnetic field, which is parallel to $\hat{n}$ and continuous across the shock, plays a passive role, and r assumes its gas dynamic value $r = (\gamma_r + 1)/(\gamma_r - 1 + 2/M_{S1}^2)$. (4) For a perpendicular ($\theta_1 = 90°$) shock, the magnetic field remains parallel to the shock on both sides, and $B_2/B_1 = U_1/U_2 = r$.

3. Test Particle Interactions with a Shock Discontinuity: Scatter-Free Conditions

In this section we consider the problem of determining exact particle orbits at a planar shock discontinuity ($r_g/L_S \to \infty$), and review how the relevant equations are solved for the case when both the magnetic and electric fields are static and uniform on both sides of the shock. We refer to this case as acceleration under scatter-free conditions to distinguish it from the case where acceleration proceeds in the presence of magnetic fluctuations (e.g., Alfvén waves) that may exist in the shock vicinity. This second case is dealt with in Section 4.

3.1. Equations of motion

In solving for charged particle orbits at a shock, the basic problem is to solve the following set of first-order, ordinary, coupled differential equations

$$\dot{\mathbf{p}}(t) = q[\boldsymbol{\varepsilon}(\mathbf{x}, t) + [\mathbf{p}(t)/m] \times \mathbf{B}(\mathbf{x}, t)/c] , \tag{16}$$

$$\dot{\mathbf{x}}(t) = \mathbf{v}(t) = \mathbf{p}(t)/m \tag{17}$$

for the particle position $\mathbf{x} = (x, y, z)$ and momentum $\mathbf{p} = (p_x, p_y, p_z)$ at time t on either side of the shock, subject to the initial conditions $\mathbf{x}(t_0)$ and $\mathbf{p}(t_0)$ at $t = t_0$. Here, $m = \gamma m_0$, where $\gamma = [1 + (p/m_0 c)^2]^{1/2}$ is the Lorentz factor, and m_0 and q are the particle's rest mass and charge, respectively. The particle's total energy is $W = \gamma m_0 c^2$, and its kinetic energy is $E = (\gamma - 1) m_0 c^2$. The electric and magnetic fields $\boldsymbol{\varepsilon}(\mathbf{x}, t)$ and $\mathbf{B}(\mathbf{x}, t)$ can be arbitrary functions of $\mathbf{x}$ and t, but we will restrict our attention to the situation where the fields consist of the uperturbed or '*DC*' components $\boldsymbol{\varepsilon}_0$ and $\mathbf{B}_0$ upon which is superposed a fluctuating or '*ac*' component due to waves or turbulence in the ambient plasma. The goal to solve Equations (16) and (17) in the generally complex fields on either side of the shock, and monitor the particle's position so that one can accurately determine when the particle crosses the shock, in which case the character of the fields $\boldsymbol{\varepsilon}(\mathbf{x}, t)$ and $\mathbf{B}(\mathbf{x}, t)$ will change abruptly.

Both the procedure and reference frame one chooses to use to solve (16) and (17) depend upon the complexity of the fields. For example, if $\boldsymbol{\varepsilon}$ and $\mathbf{B}$ are given in shock frame K, it is relatively straightforward to numerically integrate (16) and (17) using any of the several standard algorithms to solve coupled differential equations as an initial value problem (e.g., Carnahan *et al.*, 1969). The disadvantage of performing the integrations in frame K is that the convection electric field is always present, so a particle's energy is a function of its instantaneous gyrophase angle. It has proven very useful to perform the integrations of (16) and (17) with respect to the plasma frames K_1 or K_2 while the particle is in the upstream or downstream regions, respectively. For example, when the fields are static and uniform, the electric field vanishes in frame K_i ($i = 1$ or 2), and one can write down exact solutions of (16) and (17) that are relativistically correct. More importantly, when magnetic fluctuations are present, it is often a good approximation to neglect the associated electric field fluctuations when one performs calculations in the plasma frame, so scattering off the magnetic fluctuations remains magnetostatic, and kinetic energy is conserved in frame K_i. Also, if one chooses to introduce scattering using a less rigorous but faster algorithm, such as defining a scattering probability and using a Monte-Carlo scheme, the plasma frame is generally the proper frame in which to do so.

Finally, we note that integration of (16) and (17) can also be performed in the HT frame K' as long as the transformation speed into K' is subluminal, and, more significantly, as long as magnetic fluctuations that produce changes in θ_i (to which the V_i in Equation (5) can be very sensitive, particularly at quasi-perpendicular shocks) are totally absent. Thus, frame K' is of no use for performing integrations in the most physically interesting situations where the r.m.s. amplitude of magnetic fluctuations, ΔB, is comparable to the background field, i.e., $\Delta B/B_0 \sim 1$.

3.2. FRAME TRANSFORMATIONS AND THE CROSSING TIME ALGORITHM

Numerical integration of Equations (16) and (17) for static and uniform fields at a fast-mode planar shock were performed in frame K' by Hudson (1965). However, the comparison of spacecraft observations with orbit integration studies is only meaningful in the spacecraft frame, which, for typical flow speeds ($\sim$ few hundred km s^{-1}) and particle energies ($\gtrsim 10$ keV protons), is well-approximated by frames K, K_1, or K_2. As a result, Chen (1975) undertook an exhaustive investigation of how distributions of charged particles are modified by a single encounter with quasi-perpendicular shocks as observed in shock frame K. For the constant and uniform field given by (2) and (3), one can solve (16) and (17) analytically for the exact particle orbits on either side of the shock. One then proceeds in one of two ways. First, starting with the initial conditions, one steps the orbit equations for $\mathbf{x}(t)$ and $\mathbf{p}(t)$ in time using the constant fields appropriate to that particular side of the shock, and proceeds until a shock crossing is detected, i.e., the particle's x-coordinate changes sign. Then, one backs up a time step, reduces the size of the time step, and repeats the procedure until the shock crossing time is determined to some specified accuracy. Using the particle's position and momentum at the shock crossing as new initial conditions, one substitutes the fields appropiate to the new side of the shock into the orbit equations, and proceeds, essentially solving for the particle's interaction with the shock as a series of initial value problems. A second, much faster algorithm to calculate the particle's behavior at the shock was introduced by Chen (1975), and involves solving the transcendental equation $x(t) = 0$ for the crossing times. This was done for particle phase space coordinates $[\mathbf{x}(t), \mathbf{p}(t)]$ in shock frame K, and was limited to nonrelativistic particle energies ($E \ll m_0c^2$). In the following discussion, we outline how the crossing time algorithm can be implemented, but generalize Chen's technique to include relativistic particle energies by working in the plasma frames K_i and transforming to frame K at the end.

First, it is necessary to establish the transformation equations among the frames K_1, K_2, and K. We suppose that at injection ($t = 0$), the origins of the coordinate systems K_1, K_2, and K coincide (Figure 1(a)). We allow particle motion to be relativistic, but restrict the relative velocities among the reference frames to be nonrelativistic, i.e., we neglect terms of order $(U_i/c)^2$. If a particle's phase space coordinates relative to plasma frame K_i are $[\mathbf{x}_i(t), \mathbf{p}_i(t)]$, its coordinates $[\mathbf{x}(t), \mathbf{p}(t)]$ relative to shock frame K are

$$\mathbf{x}(t) = S_i\mathbf{x}_i(t) + \mathbf{U}_i t\,, \tag{18a}$$

$$\mathbf{p}(t) = S_i\mathbf{p}_i(t) + \gamma_i m_0 U_i, \tag{18b}$$

where $\gamma_i = [1 + (p_i/m_0c)^2]^{1/2}$, $p_i = |\mathbf{p}_i|$, and S_i is the rotation matrix

$$S_i = \begin{pmatrix} \sin\theta_i & 0 & \cos\theta_i \\ 0 & 1 & 0 \\ -\cos\theta_i & 0 & \sin\theta_i \end{pmatrix}. \tag{19}$$

The inverse transformation from K to K_i is

$$\mathbf{x}_i(t) = S_i^T \mathbf{x}(t) - \mathbf{W}_i t, \tag{20a}$$

$$\mathbf{p}_i(t) = S_i^T \mathbf{p}(t) - \gamma m_0 \mathbf{W}_i, \tag{20b}$$

where S_i^T is the transpose of S_i, $\gamma = [1 + (p/m_0 c)^2]^{1/2}$, $p = |\mathbf{p}|$, and $\mathbf{W}_i$ is the constant vector

$$\mathbf{W}_i = \begin{pmatrix} U_i \sin(\theta_i - \delta_i) \\ 0 \\ U_i \cos(\theta_i - \delta_i) \end{pmatrix}. \tag{21}$$

When working in the plasma frames, energy is conserved when either $\mathbf{B}_i = \mathbf{B}_{0i}$ or scattering off of magnetic fluctuations is elastic; therefore, energy changes resulting from shock interactions are formally introduced when on performs Lorentz transformations from one plasma frame to the other at shock crossings. Given coordinates $[\mathbf{x}_1(t), \mathbf{p}_1(t)]$ in K_1, those $[\mathbf{x}_2(t), \mathbf{p}_2(t)]$ relative to K_2 are given by

$$\mathbf{x}_2(t) = R\mathbf{x}_1(t) + \mathbf{A}_1 t, \tag{22a}$$

$$\mathbf{p}_2(t) = R\mathbf{p}_1(t) + \gamma_1 m_0 \mathbf{A}_1, \tag{22b}$$

where R is the rotation matrix

$$R = \begin{pmatrix} \cos \Delta & 0 & \sin \Delta \\ 0 & 1 & 0 \\ -\sin \Delta & 0 & \cos \Delta \end{pmatrix}, \tag{23}$$

$\Delta = \theta_2 - \theta_1$, and $\mathbf{A}_1$ is the constant vector

$$\mathbf{A}_1 = \begin{pmatrix} U_1 \sin(\theta_2 - \delta_1) - U_2 \sin(\theta_2 - \delta_2) \\ 0 \\ U_1 \cos(\theta_2 - \delta_1) - U_2 \cos(\theta_2 - \delta_2) \end{pmatrix}. \tag{24}$$

The inverse transformation from K_2 to K_1 is

$$\mathbf{x}_1(t) = R^T \mathbf{x}_2(t) - \mathbf{A}_2 t, \tag{25a}$$

$$\mathbf{p}_1(t) = R^T \mathbf{p}_2(t) - \gamma_2 m_0 \mathbf{A}_2, \tag{25b}$$

where R^{T} is the transpose of R, and $\mathbf{A}_2 = R^T \mathbf{A}_1$.

Now, returning to the case of constant and uniform fields, we have $\mathbf{B}_i = \mathbf{B}_{0i}$, so the solutions of (16) and (17) in frame K_i are trivial:

$$x_i(t) = x_{i0} + r_{i\perp} [\sin(\Omega_i t + \phi_{i0}) - \sin \phi_{i0}], \tag{26a}$$

$$y_i(t) = y_{i0} - r_{i\perp}[\cos(\Omega_i t + \phi_{i0}) - \cos\phi_{i0}]\,, \tag{26b}$$

$$z_i(t) = z_{i0} + v_{i\parallel} t\,, \tag{26c}$$

$$p_{ix}(t) = p_{i\perp}\cos(\Omega_i t + \phi_{i0})\,, \tag{26d}$$

$$p_{iy}(t) = p_{i\perp}\sin(\Omega_i t + \phi_{i0})\,, \tag{26e}$$

$$p_{iz}(t) = p_{i\parallel}\,, \tag{26f}$$

where $\mathbf{x}_i(0) = [x_{i0}, y_{i0}, z_{i0}]$, $p_{i\perp} = (p_{ix}^2 + p_{iy}^2)^{1/2} = p_i \sin\alpha_i$, $p_{i\parallel} = p_i\cos\alpha_i$, $p_i = p_{i0}$, $r_{i\perp} = v_{i\perp}/\Omega_i$, $v_{i\perp} = p_{i\perp}/\gamma_i m_0$, and $\Omega_i = qB_{0i}/\gamma_i m_0 c$. The angle $\alpha_i = \alpha_{i0}$ is the (constant) pitch angle, and ϕ_{i0} is the initial gyrophase angle. (The 'initial' time $t = 0$ can be either the injection time or the time of the particle's most recent shock crossing.) Using the orbit Equations (26) in Equation (18a) gives the particle's x-coordinate in shock frame K in terms of its phase space coordinates in plasma frame K_i at time t:

$$x(t) = x_i(t)\sin\theta_i + z_i(t)\cos\theta_i + U_i t\cos\delta_i\,, \tag{27a}$$

$$= a_i + b_i\sin(\Omega_i t + \phi_{i0}) + c_i t\,, \tag{27b}$$

where the constants in (27b) are

$$a_i = x_{i0}\sin\theta_i + z_{i0}\cos\theta_i - r_{i\perp}\sin\theta_i\sin\phi_{i0}\,, \tag{28a}$$

$$b_i = r_{i\perp}\sin\theta_i\,, \tag{28b}$$

$$c_i = v_{i\parallel}\cos\theta_i + U_i\cos\delta_i\,. \tag{28c}$$

For a specific set of constants (28) in frame K_i, the time of the next shock crossing in the smallest, positive, nonzero root of the transcendental equation

$$x(t) = a_i + b_i\sin(\Omega_i t + \phi_{i0}) + c_i t = 0\,. \tag{29}$$

Clearly, any root of (29) must lie within the interval bounded by $t_- = (b_i - a_i)/c_i$ and $t_+ = -(b_i + a_i)/c_i$. If both t_- and t_+ are negative, no positive root of (29) exists, i.e., no future shock crossing is possible for this set of coefficients (28). If either t_- or t_+ is negative and the other positive, confine attention to zero and the positive of the two. If an interval for a positive root of (29) exists, define t_0 and $t_f > t_0$ as its endpoints, such that $[t_0, t_f]$ is the interval. The roots of (29) can be obtained using the half-interval method, which must be applied to an interval within which the function has only one root. Since $x(t)$ is oscillatory and may possess multiple roots in $[t_0, t_f]$, section $[t_0, t_f]$ into subintervals such that the endpoints of each subinterval are at the extrema of $x(t)$. The extrema of $x(t)$ are found from the roots of its derivative, which, upon defining $\psi = \Omega_i t + \phi_{i0}$, implies that the zeros of $\mathrm{d}x(\psi)/\mathrm{d}\psi$ are all the $\psi_j, j = 1, 2, 3, \ldots$, such that $\cos\psi_j = -c_i/b_i\Omega_i$. Then, if t_j are the times associated with the subinterval boundaries, apply the half-interval calculation to the first subinterval $[t_k, t_{k+1}]$, $k = 0, 1, 2, \ldots$, that satisfies the condition $x(t_k)x(t_{k+1}) < 0$ and determine the crossing time. Substitute the crossing time into Equations (22) or (25) to obtain a new set of initial conditions in the new plasma frame, re-evaluate the coefficients in (28), and repeat the entire process to solve for a new root of $x(t) = 0$ in (29). Continue until no more roots of $x(t) = 0$ are found, in which case the particle's encounter with the shock is over. If desired, transform to the shock frame using Equations (18). This algorithm can be easily adapted to include scattering between shock crossings using Monte-Carlo techniques.

3.3. NUMERICAL RESULTS FOR SCATTER-FREE SHOCK DRIFT ACCELERATION

The process whereby an energetic charged particle is accelerated at a collisionless shock when the electric and magnetic fields remain uniform and static on both sides of the shock during the particle's interaction with the shock is known as the scatter-free shock drift acceleration (SDA) process. We shall often refer to SDA as simply the drift process, whether or not motion is scatter-free away from the shock. As we will discuss in Section 4, the drift process remains clearly evident in the presence of magnetic fluctuations, although the characteristics of the accelerated particle distributions are significantly different from those in the scatter-free limit. Also, with the exception of a few comments at the close of this section, we shall confine our attention for the remainder of this review to acceleration at fast-mode shocks.

Figures 2 and 3 show examples of exact particle orbits in frame K under scatter-free conditions upstream and downstream of the shock. In Figure 2, $\theta_1 = 80°$ (i.e., the shock obliquity is in the quasi-perpendicular regime, $45° \lesssim \theta_1 \leq 90°$), $\delta_1 = 0°$, $\beta = 1$, and

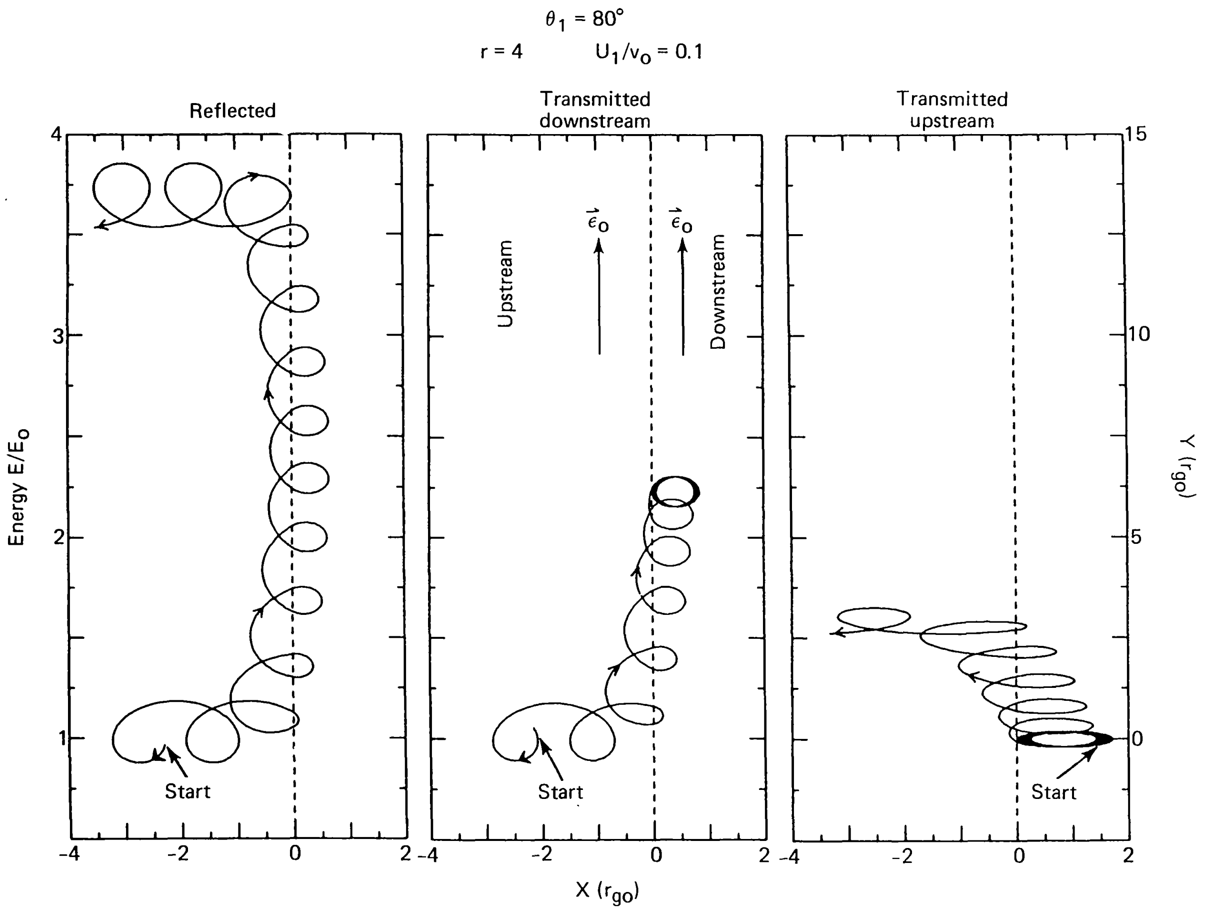

Fig. 2. Sample particle trajectories in shock frame K at quasi-perpendicular shock with $\theta_1 = 80°$.

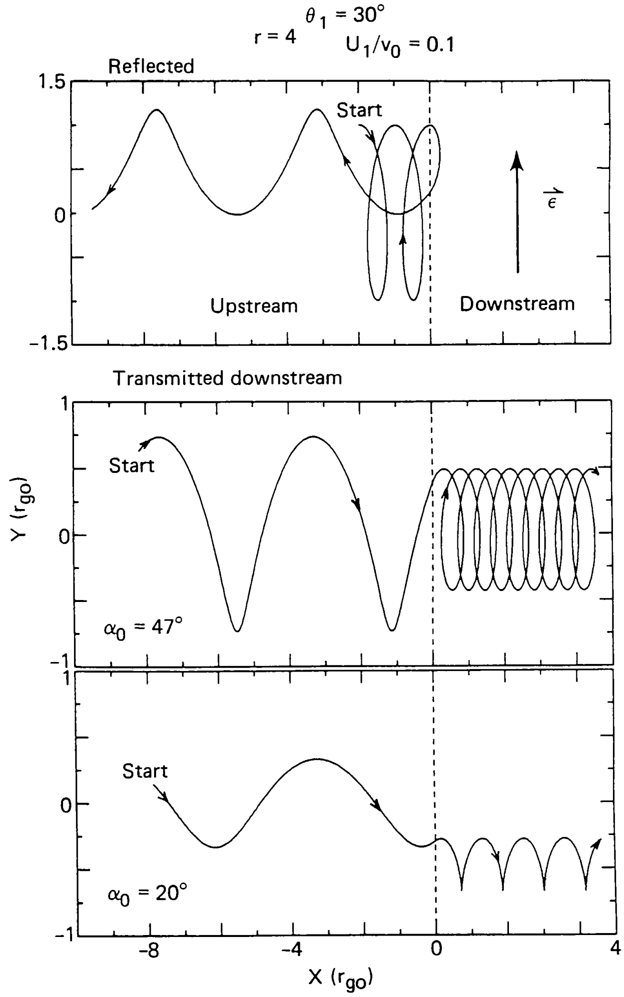

Fig. 3. Sample particle trajectories in shock frame K at quasi-parallel shock with $\theta_1 = 30°$.

$M_{A1} = 10$, which from the magnetic RH-conditions, yields strength $r \cong 4$ (i.e., a strong shock). At injection, the particle's initial speed was $v_0 = 10\,U_1$. Plotted in Figure 2 are both the particle's energy E (divided by its initial energy E_0) and its y-coordinate versus its x-coordinate, with the stationary shock indicated by the dashed vertical line at $x = 0$, and the electric field $\varepsilon_0 = \hat{y}\varepsilon_0$. Distances are in units of the particle's (nonrelativistic) gyroradius $r_{g0} = v_0/\Omega_{01}$, $\Omega_{01} = qB_{01}/m_0c$. The three particles had different pitch and gyrophase angles at injection. Particles injected upstream of the shock are either reflected or transmitted downstream after a single encounter with the shock, while those injected downstream are transmitted upstream (for a fast-mode shock, $B_2 > B_1$, so there are no reflected downstream particles).

Basically, as observed from frame K, an energetic particle is drift accelerated during a single shock encounter as its guiding center 'drifts' along the $\mathbf{U} \times \mathbf{B}_0$ electric field. This drift is actually composed of several discrete deflections of the particle's guiding center that occur each time the particle crosses the shock and experiences the abrupt change in both the strength and direction of the magnetic field. A single encounter, therefore, consists of many individual penetrations or crossings of the particle's orbit through the shock surface. The total energy gain, $\Delta E = q\varepsilon_0 \Delta y$, depends upon the total drift distance

Δy, which for an oblique shock is a complicated function of the particle's initial velocity, and, in the presence of field fluctuations, any wave-particle interactions that occur within a gyroradius of the shock. As the representative orbits in Figure 2 show, the drift process at a quasi-perpendicular shock can produce energy gains for all three cases, and, as is true on average, reflected particles gain more energy than those transmitted downstream, with in turn gain more energy than those transmitted upstream.

The situation is different at a quasi-parallel ($0° \leq \theta_1 \lesssim 45°$) shock. Figure 3 shows typical examples of reflected and transmitted downstream particles for a single encounter at a $\theta_1 = 30°$ shock. Shown is y versus x to emphasize the small energy changes involved. The top panel shows a small net deflection of the gyrocenter $\Delta y_g > 0$. The lower panels show two particles, both of which are transmitted after only one shock crossing, with one (initial pitch angle $\alpha_0 = 47°$) undergoing a slight acceleration ($\Delta y_g > 0$) and the other ($\alpha_0 = 20°$) undergoing a marked deceleration ($\Delta y_g < 0$).

Figures 2 and 3 show that a typical drift encounter at a quasi-perpendicular shock is markedly different from that at a quasi-parallel shock. At a quasi-perpendicular shock, drift encounters generally involve many shock crossings, with large net energy and pitch angle changes evolving relatively slowly from crossing to crossing. At a quasi-parallel shock, drift encounters involve only a few shock crossings that resemble large-angle scatterings rather than gradual processes that resemble drifts, and can result in small energy losses as well as small energy gains. The term 'drift' is obviously inappropriate in this case.

The process leading to reflection at oblique fast-mode shocks is easily understood with the aid of Figure 4, which shows the $(x - z)$-plane containing the upstream and downstream field lines and their extensions across the shock (dashed lines) (adapted from Armstrong *et al.*, 1977). For the sake of illustration, we neglect the particle's spatial evolution from one crossing to another, and refer the entrance and exit velocities to the same spatial location at the shock. Suppose that upon crossing the shock from upstream to downstream, $\mathbf{v}$ is the $(x - z)$-plane projection of the particle velocity, and $\mathbf{v}_{2_\parallel}$ and $\mathbf{v}_{1_\parallel}$ are the projections of $\mathbf{v}$ onto $\mathbf{B}_{02}$ and the downstream extension of $\mathbf{B}_{01}$, respectively. Likewise, upon its subsequent crossing upon returning upstream, $\mathbf{v}^*$ is the $(x - z)$-plane projection of the particle's velocity, and $\mathbf{v}^*_{1_\parallel}$ the projection of $\mathbf{v}^*$ along $\mathbf{B}_{01}$. One can view this process from either the shock frame K, in which case, $|\mathbf{v}|$ and $|\mathbf{v}^*|$ will generally differ because of field line convection (or, equivalently, because of ε_0), or if $V_1/c < 1$, from the HT frame K', in which case $|\mathbf{v}'| = |\mathbf{v}'^*|$, where $\mathbf{v}'_{1_\parallel} = \mathbf{v}_{1_\parallel} + \mathbf{V}_1$, etc. In either case, note that $|\mathbf{v}_{2_\parallel}| < |\mathbf{v}_{1_\parallel}|$, and further that $|\mathbf{v}^*_{1_\parallel}| < |\mathbf{v}_{1_\parallel}|$. Thus, there is a net increase in the component of velocity anti-parallel to $\mathbf{B}_{01}$, i.e., headed away from the shock upstream. Iteration of this process over several shock crossings leads ultimately to reflection or transmission through the shock. As viewed from frame K', it is primarily the particle's pitch angle α'_0 at injection that determines whether reflection or transmission occurs.

Figure 5 is a summary of how the degree of energization after a single shock encounter depends upon incident pitch angle α_0 and gyrophase angle ϕ_0 in shock frame K (from Armstrong *et al.*, 1977), as adapted from Chen, 1975. These results were obtained using

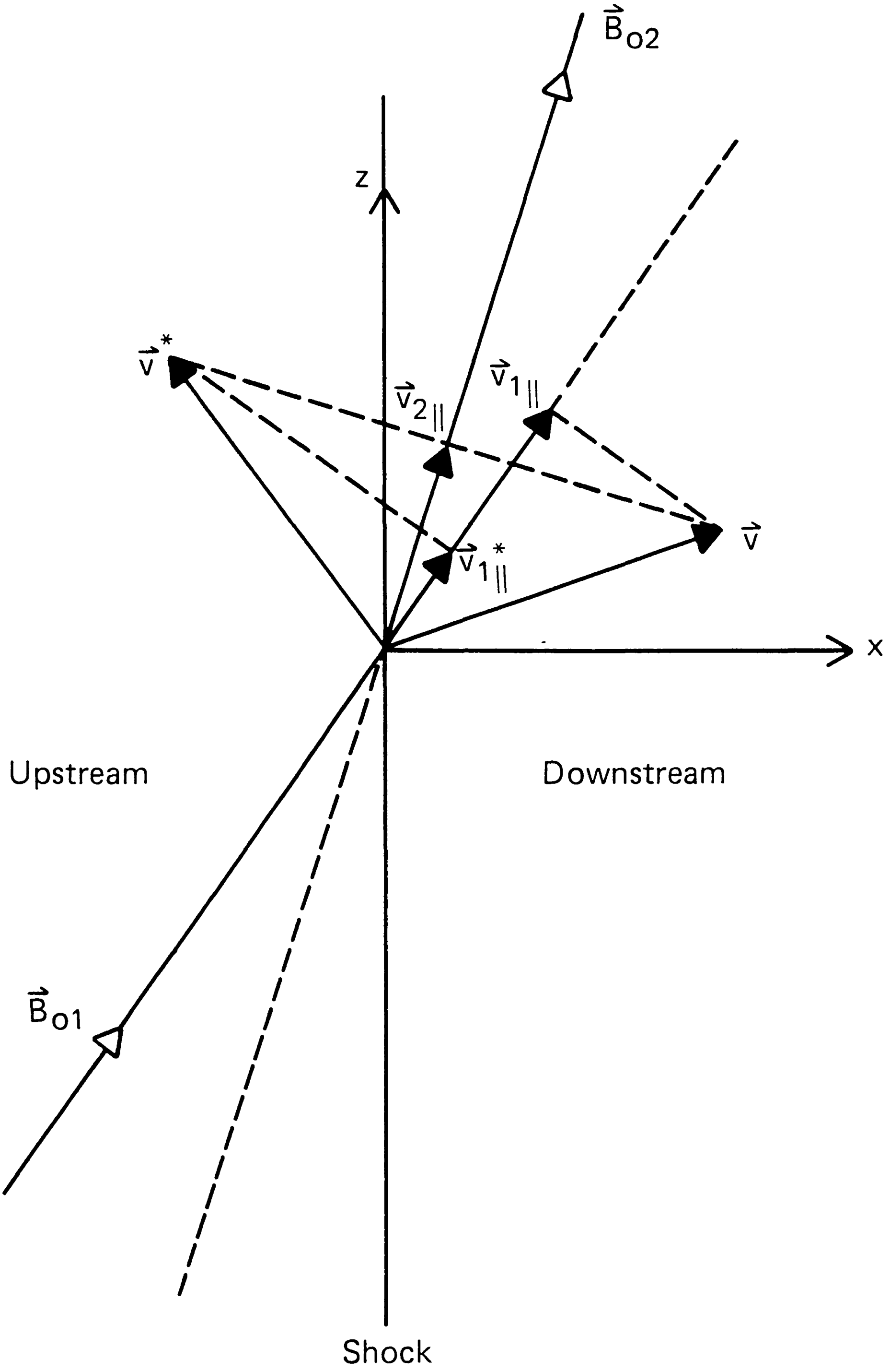

Fig. 4. Schematic illustration of reflection process at an oblique shock discontinuity (adapted from Armstrong *et al.*, 1977).

the crossing time algorithm on 1972 particles injected in an isotropic distribution immediately upstream of a quasi-perpendicular shock with $\theta_{Bn} = \theta_1 = 84.3°$ and $B_2/B_1 = 2$. At injection, $v_0/U_1 = 10$ ($= v_i/v_s$). Zero-degree pitch angle is away from the shock upstream, towards the shock downstream. Plotted numbers represent reflected particles, such that 0 denotes the ratio of final to initial energies E/E_0 in the interval (0, 1), 1 denotes E/E_0 in (1, 2), etc., and plotted letters represent transmitted particles,

1988SSRv...48..195D

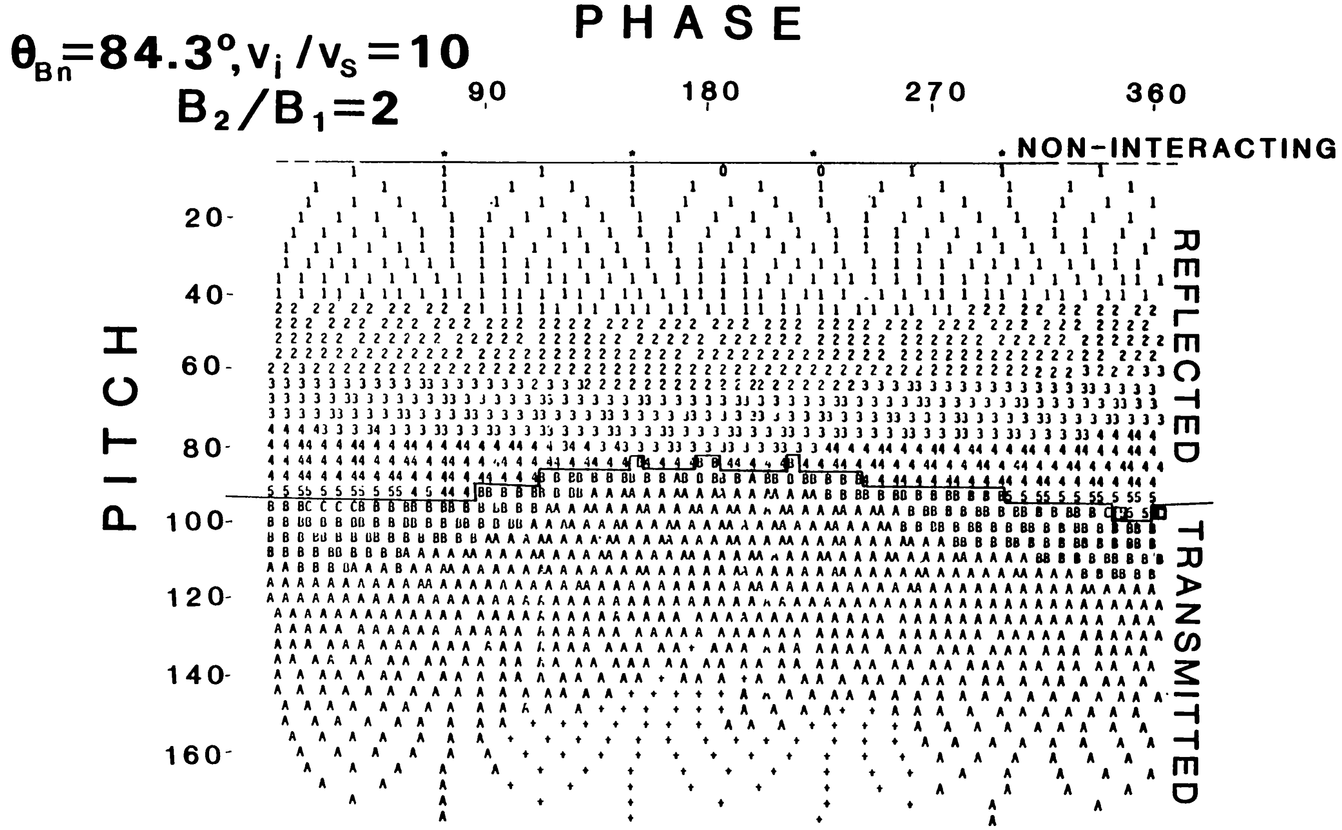

Fig. 5. Map of energy gain for 1972 particles after single encounter with $\theta_1 = 84.3°$ shock. At injection particles were distributed isotropically with initial pitch and phase angles shown. Numbers denote reflected particles, letters transmitted particles. See text for details (adapted from Armstrong *et al.*, 1977).

such that + stands E/E_0 in (0, 1), A denotes E/E_0 in (1, 2), etc. The most energetic particles lie near the boundary that separates reflected from transmitted particles, which in this case occurs at $\alpha_0 = 90° \pm 6°$. The most energetic particles crossed the shock 50 times. A particle's fate is most sensitive to its initial pitch angle, and less so to its initial gyrophase, although other orbit integration studies show that the gyrophase dependence does increase somewhat at the mid-range obliquities $\theta_1 \sim 30° - 60°$.

3.4. COMPARISON OF ORBIT INTEGRATIONS WITH ADIABATIC TEST PARTICLE THEORY

The degree of order apparent in plots such as Figure 5 suggest an underlying simplicity, and one expects the under a certain set of conditions, the numerical results should be organized by some analytical, albeit approximate, expressions. This is indeed the case for scatter-free particle encounters with an infinitesimally thin, planar, oblique shock under uniform and static conditions. The theory is based entirely upon the assumption that a particle's magnetic moment as measured in either plasma frame K_i or the HT frame K' is the same before and after (but not necessarily during) a shock encounter. If in addition, $V_i/c < 1$, one can transform from K_i or K to K' where a particle's energy is also conserved during a shock encounter.

The possibility that a charged particle's magnetic moment is an approximate invariant of a shock interaction and that this idea can be used to calculate the characteristics of superthermal as well as high-energy particles at oblique shocks has been exploited by a number of authors (e.g., Parker, 1958; Shabanskii, 1962; Schatzman, 1963; Hudson, 1965; Sonnerup, 1969; Alekseyev and Kropotkin, 1970; Sarris and Van Allen, 1974; Vasilýev *et al.*, 978; Terasawa, 1979; Pesses, 1979; Decker, 1983; Webb *et al.*, 1983; Schwartz *et al.*, 1983; Wu, 1984; Pesses and Decker, 1986; Vandas, 1987). We shall restrict our attention here to particles with sufficiently high energy so that we can approximate the shock by a discontinuity, neglecting the magnetic field overshoot and cross-shock potential associated with the shock transition (e.g., Leroy *et al.*, 1982). Then, in the HT frame K', a particle's magnetic moment $M' = p'^2 \sin^2 \alpha'/2m_0 B$ as well as its kinetic energy is assumed to remain unchanged before and after a shock encounter. Analytically, one expects M' invariance to be a good approximation at a nearly perpendicular shock when $\Delta_{1,2} \ll 1$ and $\Delta_{1,2} \cot \alpha'_{1,2} \ll 1$, where $\Delta_{1,2} = \pi/2 - \theta_{1,2}$ (Alekseyev and Kropotkin, 1970; Toptyghin, 1980). Numerical studies have confirmed this (Hudson, 1965; Terasawa, 1979), and have also shown that, on average, the approximate invariance of M' holds over a wider range of θ_1 than expected theoretically (Terasawa, 1979). This 'adiabatic approximation' enables one to model shock encounters in K' and derive transmission coefficients and expressions for energy and pitch angle changes in the shock frame K (Webb *et al.*, 1983) or the plasma frames K_i (Vasilýev *et al.*, 1978; Pesses, 1979; Pesses *et al.*, 1982; Toptyghin, 1980; Decker, 1983; Ostrowski, 1988) by transforming into and out of K' using the velocities described in Section 2.1.

To derive the 'adiabatic test particle' expressions for energy and pitch angle changes resulting from a single shock encounter, we shall work between the plasma frames K_i and the HT frame K'. We assume that transformations between K_i and K' remain nonrelativistic, i.e., $(V_i/c)^2 \ll 1$, but allow for relativistic particle energies. Now, a particle with speed v_i in K_i has speed $v'_i = (1 + \beta_i R_i \mu_i)^{-1}(1 + 2\varepsilon_i \mu_i + \varepsilon_i^2)^{1/2}$ in K', where $\beta_i = v_i/c$, $R_i = V_i/c$, $\mu_i = \cos \alpha_i$, and

$$\varepsilon_i = V_i/v_i = (U_i/v_i) \sec \theta_i \cos \delta_i \,. \tag{30}$$

The corresponding pitch cosine in K' is $\mu'_i = (\mu_i + \varepsilon_i)(1 + 2\varepsilon_i \mu_i + \varepsilon_i^2)^{-1/2}$. Solving this for μ_i in terms of ε_i and μ'_i, and setting $\mu'_i = \mu'_c = \cos \alpha'_c = (1 - b^{-1})^{1/2}$, where α'_c is the loss cone angle in K' for $b = B_2/B_1$, yields ($i = 1$)

$$\mu_\pm = \varepsilon_1 b^{-1} \pm [(1 - b^{-1})(1 - b^{-1}\varepsilon_1^2)]^{1/2} , \tag{31}$$

where for $\varepsilon_1 < 1$, we take the upper sign, while for $\varepsilon_1 \geq 1$, we must allow for both signs. Note that for $\varepsilon_1 \ll 1$, $\mu_+ \lesssim (1 - b^{-1})^{1/2} = \mu'_c$, so the difference between frames K_1 and K' diminishes at high energies. Given a particle's initial kinetic energy E_i and pitch cosine μ_i in plasma frame K_i, we transform into K$'$, determine whether the particle is reflected ($0 < \mu'_1 \leq \mu'_c$), transmitted downstream ($\mu'_c < \mu'_1 \leq 1$), transmitted upstream ($-1 \leq \mu'_2 < 0$), or noninteracting ($-1 \leq \mu'_1 \leq 0$, $0 \leq \mu'_2 \leq 1$), conserve the particle's energy and pitch angle accordingly, and transform back to the appropriate plasma frame. We find for reflected (R) particles,

$$E_1^R = E_1[1 + 2\gamma_1(\gamma_1 - 1)^{-1}\beta_1^2 \varepsilon_1(\varepsilon_1 + \mu_1)] , \tag{32}$$

$$\mu_1^R = \frac{-(2\varepsilon_1 + \mu_1)}{[1 + 4\varepsilon_1(\varepsilon_1 + \mu_1)]^{1/2}} \tag{33}$$

which are valid for

$$-\varepsilon_1 < \mu_1 \leq \mu_+ \quad (\varepsilon_1 < 1)\,, \tag{34a}$$

$$\mu_- < \mu_1 \leq \mu_+ \quad (1 \leq \varepsilon_1 < b^{1/2})\,, \tag{34b}$$

where $\gamma_1 = (1 - \beta_1^2)^{-1/2}$.

For transmitted downstream (D) particles,

$$\begin{aligned} E_2^D = E_1(1 + \gamma_1(\gamma_1 - 1)^{-1}\beta_1 R_1\{\tfrac{1}{2}(1 + f^2)\varepsilon_1 + \mu_1 - \\ -f[(\varepsilon_1 + \mu_1)^2 - (b - 1)(1 - \mu_1^2)]^{1/2}\})\,, \end{aligned} \tag{35}$$

$$\mu_2^D = \frac{[(\varepsilon_1 + \mu_1)^2 - (b - 1)(1 - \mu_1^2)]^{1/2} - f\varepsilon_1}{\{([(\varepsilon_1 + \mu_1)^2 - (b - 1)(1 - \mu_1^2)]^{1/2} - f\varepsilon_1)^2 + b(1 - \mu_1^2)\}^{1/2}} \tag{36}$$

which are valid for

$$\mu_+ < \mu_1 \leq 1 \qquad (\varepsilon_1 < 1)\,, \tag{37a}$$

$$-1 \leq \mu_1 \leq \mu_- \ \text{ and } \ \mu_+ < \mu_1 \leq 1 \qquad (1 \leq \varepsilon_1 < b^{1/2})\,, \tag{37b}$$

$$-1 \leq \mu_1 \leq 1 \qquad (\varepsilon_1 \geq b^{1/2})\,, \tag{37c}$$

where $f = V_2/V_1 = (B_2/B_1)(U_{2x}/U_{1x}) = b/r$ $(0 \leq f \leq 1)$.

For transmitted upstream (U) particles,

$$\begin{aligned} E_1^U = E_2(1 + \gamma_2(\gamma_2 - 1)^{-1}\beta_2 R_2\{\tfrac{1}{2}(1 + f^{-2})\varepsilon_2 - \mu_2 - \\ -f^{-1}[(\varepsilon_2 + \mu_2)^2 + (1 - b^{-1})(1 - \mu_2^2)]^{1/2}\})\,, \end{aligned} \tag{38}$$

$$\mu_1^U = \frac{-[(\varepsilon_2 + \mu_2)^2 + (1 - b^{-1})(1 - \mu_2^2)]^{1/2} + f^{-1}\varepsilon_2}{\{([(\varepsilon_2 + \mu_2)^2 + (1 - b^{-1})(1 - \mu_2^2)]^{1/2} + f^{-1}\varepsilon_2)^2 + b^{-1}(1 - \mu_2^2)\}^{1/2}} \tag{39}$$

which are valid for

$$-1 \leq \mu_2 < -\varepsilon_2 \quad (\varepsilon_2 < 1)\,, \tag{40}$$

where $\gamma_2 = (1 - \beta_2^2)^{-1/2}$.

Noninteracting upstream particles lie within $-1 \leq \mu_1 \leq -\varepsilon_1$ $(\varepsilon_1 < 1)$, and those downstream lie within $-\varepsilon_2 \leq \mu_2 \leq 1$.

Equations (32)–(40) contain several interesting predictions. First, as expected, E_1^R and E_2^D attain their maximum values for a given ε_1 when μ_1 and μ_2 on the right-hand side of Equations (32) and (35) are equal to μ_+, the loss cone angle in K_1 that separates reflected from transmitted downstream particles. Energy E_1^U is a maximum when $\mu_2 = -\varepsilon_2$ on the right-hand side of Equation (38). Both E_1^R and E_2^D attain their maximum values for any ε_1 when $\varepsilon_{1_m} = b^{1/2} = (B_2/B_1)^{1/2}$ (Vasilÿev *et al.*, 1978), so that $\mu_1 = \mu_\pm = -b^{-1/2}$ by (31) (there are no reflected particles for $\varepsilon_1 > b^{1/2}$). In this case we must use the nonrelativistic limit ($E_1 \ll m_0c^2$) of (32) and (35), since we have assumed $(V_1/c)^2 \ll 1$, and $\varepsilon_{1m} = V_1/v_{1m} = b^{1/2}$ implies $(v_{1m}/c)^2 \ll 1$ for $1 \leq b \leq 4$. Then, $\Delta E^R_m/E_1 = (E^R_{1m} - E_1)/E_1 = 4(b-1)$, and $\Delta E^D_m/E_1 = 2(b-1)$. Thus, the maximum fractional energy gain of reflected particles is twice that of transmitted downstream particles, and can be no more than a factor of 12 for a strong, nearly perpendicular shock with $b = r = 4$. Also, note that in the nonrelativistic limit, $\Delta E^R_1/E_1 = 4\varepsilon_1(\varepsilon_1 + \mu_1)$, while in the ultra-relativistic limit ($E_1 \gg m_0c^2$), $\Delta E^R_1/E_1 = 2\varepsilon_1(\varepsilon_1 + \mu_1)$. Finally, we note that for $v_1^2 \ll V_1^2 \ll c^2$, expansion of the radicals is (35) and (36) for $\varepsilon_1^2 \gg 1$ yields the simple relations $\Delta E^D_2/E_1 = (b-1)(1-\mu_1^2)$ and $\mu^D_2 = \mu_1/[\mu_1^2 + b(1-\mu_1^2)]^{1/2}$, which are just the energy change and pitch cosine of a particle transmitted through a perpendicular shock. Thus, to sufficiently low-energy particles such that $\varepsilon_1^2 \gg 1$, an oblique shock appears perpendicular.

Predictions of Equations (32)–(40) can be easily compared to results from orbit integrations. Such comparisons have been made for energies and pitch angles measured in the plasma frames (Terasawa, 1979; Pesses, 1979; Decker, 1983). However, as Webb *et al.* (1983) have pointed out, this approach always yields energy gains, whereas if one works in a single reference frame, i.e., the shock frame K, a small subset of initially

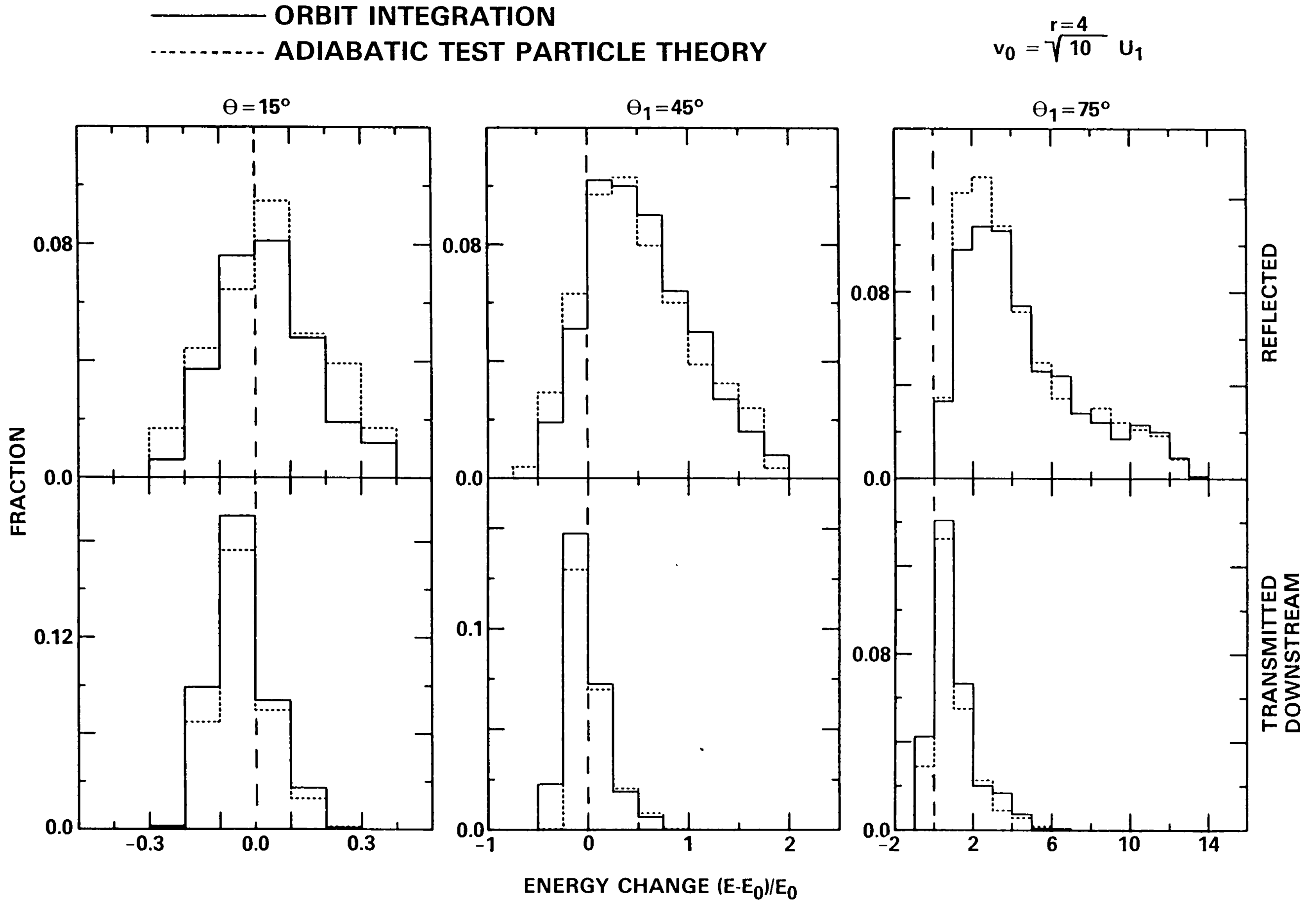

Fig. 6. Histograms of energy change for reflected (*upper*) and transmitted (*lower*) particles for three shock angles. Solid curves are from numerical solution of Equations (26). Dashed curves are from theoretical expressions (32)–(40). Energies given in shock frame.

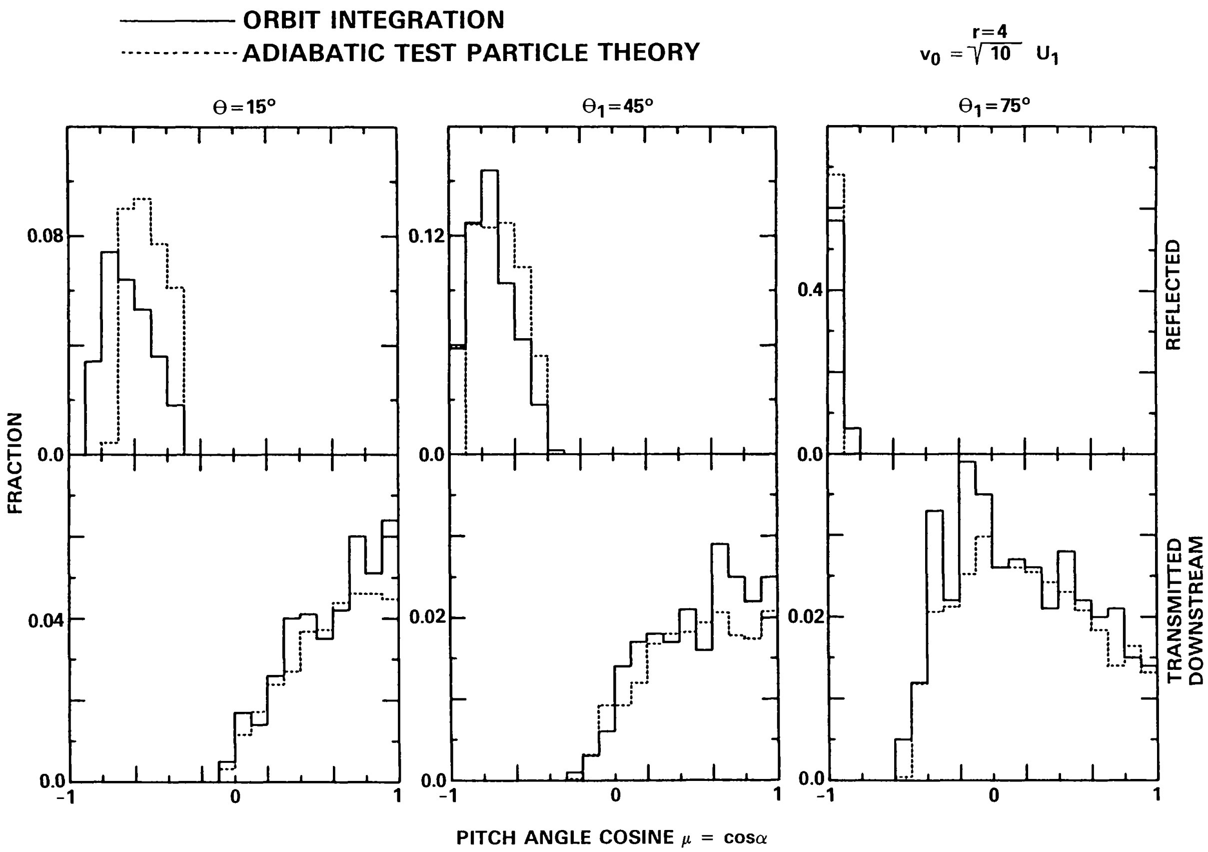

Fig. 7. Histograms of post-encounter pitch angle cosines for particles in Figure 6. Convention is that $\mu < 0$ is away from shock upstream, toward shock downstream.

field-aligned particles are predicted to undergo deceleration. One can either work out relations similar to (32)–(40) in frame K, as Webb *et al.* (1983) did, or transform the plasma frame relations (32)–(40) to the shock frame. This latter approach was used to construct Figures 6 and 7, which show energy and final pitch cosine histograms in frame K after a single encounter for 5000 protons injected upstream of shocks with $\theta_1 = 15°$, $45°$, and $75°$, $\delta_1 = 0°$, and $r = 4$. At injection, particles were isotropically distributed in plasma frame K_1 with initial speed $v_0 = \sqrt{10}\, U_1$. Solid lines denote distributions of reflected (top) and transmitted downstream (bottom) particles as determined using the crossing time algorithm on Equations (26), with both pre- and post-interaction variables expressed in frame K. Dashed curves denote results obtained using the adiabatic test particle equations. To construct these histograms, we used (32)–(40) to calculate energy and pitch cosine changes, introduced random gyrophase angles, transformed these expressions to shock frame K, and binned the results, assuming isotropic injection at speed v_0 in the upstream plasma frame K_1.

Figures 6 and 7 show that under scatter-free conditions, the adiabatic test particle theory adequately reproduces the exact orbit integration results, even in the quasi-parallel regime. Energy gains in Figure 6 increase as θ_1 increases, becoming quite large at $\theta_1 = 75°$. Note, however, that for $\theta_1 = 15°$ and $45°$, the majority of particles transmitted downstream were decelerated, i.e., $(E - E_0)/E_0 < 0$. Figure 7 shows that particles reflected after a single drift encounter form anti-shockward, field-aligned anisotropies that can become very large in the quasi-perpendicular regime (upstream, $\mu \leqslant 0$ is away from the shock, $\mu > 0$ is toward the shock; downstream it is *vice-versa*). Downstream, the peak in the distribution shifts from away from the shock along $\mathbf{B}_{02}$ to perpendicular to $\mathbf{B}_{02}$ as θ_1 increases. Note also that the fraction of transmitted particles headed shockward along $\mathbf{B}_{02}$ also increases with θ_1; however, these particles have parallel velocities $v_{\parallel} < U_2 \tan \theta_2$ and, therefore, cannot catch up with the receding shock. These are the particles that in frame K' are incident upon the shock with pitch angles near the loss cone angle α_c', and end up downstream with pitch angles near 90°; the shockward component of parallel velocity results from transforming back to K from K'.

Figure 8 shows the average energy gains and the fraction of reflected and transmitted

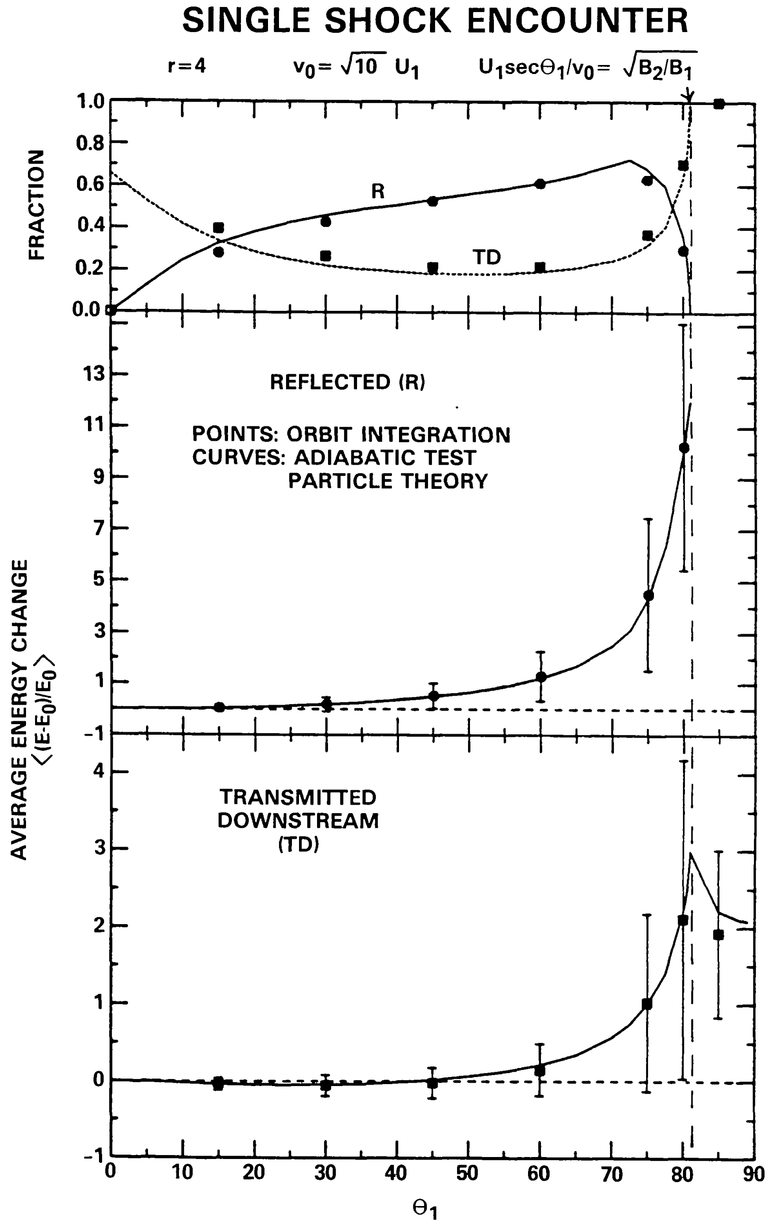

Fig. 8. Average fractional energy change (*lower two panels*) and interaction probability (*top panel*) after single encounter as a function of θ_1. Points are from numerical integrations, curves are from theoretical expressions (32)–(40).

particles as a function of θ_1. The vertical error bars on the orbit integration points are two standard deviations long, and indicate the width of the energy distributions (e.g., Figure 6). Again, simulation and theory agree very well. The value of θ_1 where reflection is expected to cease is given from theory by $\varepsilon_1 = (B_2/B_1)^{1/2}$ and is indicated at the top. Note the small average energy loss for transmitted particles when $0 \leq \theta_1 \lesssim 40°$. This is qualitatively consistent with the picture that, under the adiabatic approximation, the scatter-free drift process is equivalent to the combined action of effective gradient and curvature drifts at the shock discontinuity (Webb *et al.*, 1983) even though, as discussed with regard to Figure 3, the term 'drift' is a poor description of particle interactions with quasi-parallel shocks. Then, one expects drifts to produce a net deceleration when $0 \leq \theta_1 \leq \cot^{-1}(r^{1/2})$ $(0 \leq \theta_1 \leq 27°$ for $r = 4)$, which is the range of obliquities where the effective curvature drift (which drives ions anti-parallel to $\boldsymbol{\varepsilon}_0$) exceeds the gradient drift (which drives ions parallel to $\boldsymbol{\varepsilon}_0$). Note, however, that on average, only transmitted particles experience a net deceleration; reflected particles always show a net acceleration.

Returning to Figure 5, we note that for the parameters used, $\varepsilon_1 = U_1 \sec\theta_1/v_1 = 1.0$ (because $v_1 \gg U_1$, we need not differentiate between frames K_1 and K).By Equation (31), we find $\mu_+ = 0$, consistent with the boundary between reflected and transmitted particles at $\alpha = 90°$. For $\mu_1 = \mu_+ = 0$ and $\varepsilon_1 = 1$ in (32) and (35) $(E_1 \ll m_0c^2)$, $E_1^R/E_1 = 5$ and $E_2^D/E_1 = 3$. These are also consistent with Figure (5), although there are a few particles with energies higher than predicted based upon magnetic moment conservation.

Orbit integrations have shown that the difference between a particle's magnetic moment before and after a single, scatter-free shock encounter is small. However, as demonstrated by Pesses (1981), this is not true *during* the encounter, when the magnetic moment between crossings can deviate significantly from its intial value. Pesses showed this for a perpendicular shock, but it is also true for oblique shocks in general. Whipple *et al.* (1986) derived a generalized invariant to describe the adiabatic motion of charged particles under conditions where large field gradients exist. As one example, they applied their technique to particle motion at a perpendicular shock discontinuity. They showed that, in contrast to the particle's magnetic moment, the generalized invariant is conserved during the shock encounter, and reduces to the magnetic moment before and after the encounter. This example from Whipple *et al.* (1986) is shown in Figure 9. The top panel shows the projection onto the $(x - y)$-plane of the particle's orbit in shock frame K. The bottom panel shows the evolution during the shock encounter of the particle's magnetic moment (μ) measured in the local plasma frame, and the generalized invariant $J(\kappa, P)$. The success of this analysis is obvious in the flatness of the generalized invariant curve.

3.5. PREDICTED FLUXES AT QUASI-PERPENDICULAR SHOCKS

During an interplanetary shock event, for example, shock-accelerated particles measured in a given energy channel and solid angle map to pre-accelerated particles with various energies and angular distributions. To cast expected features of single-encounter

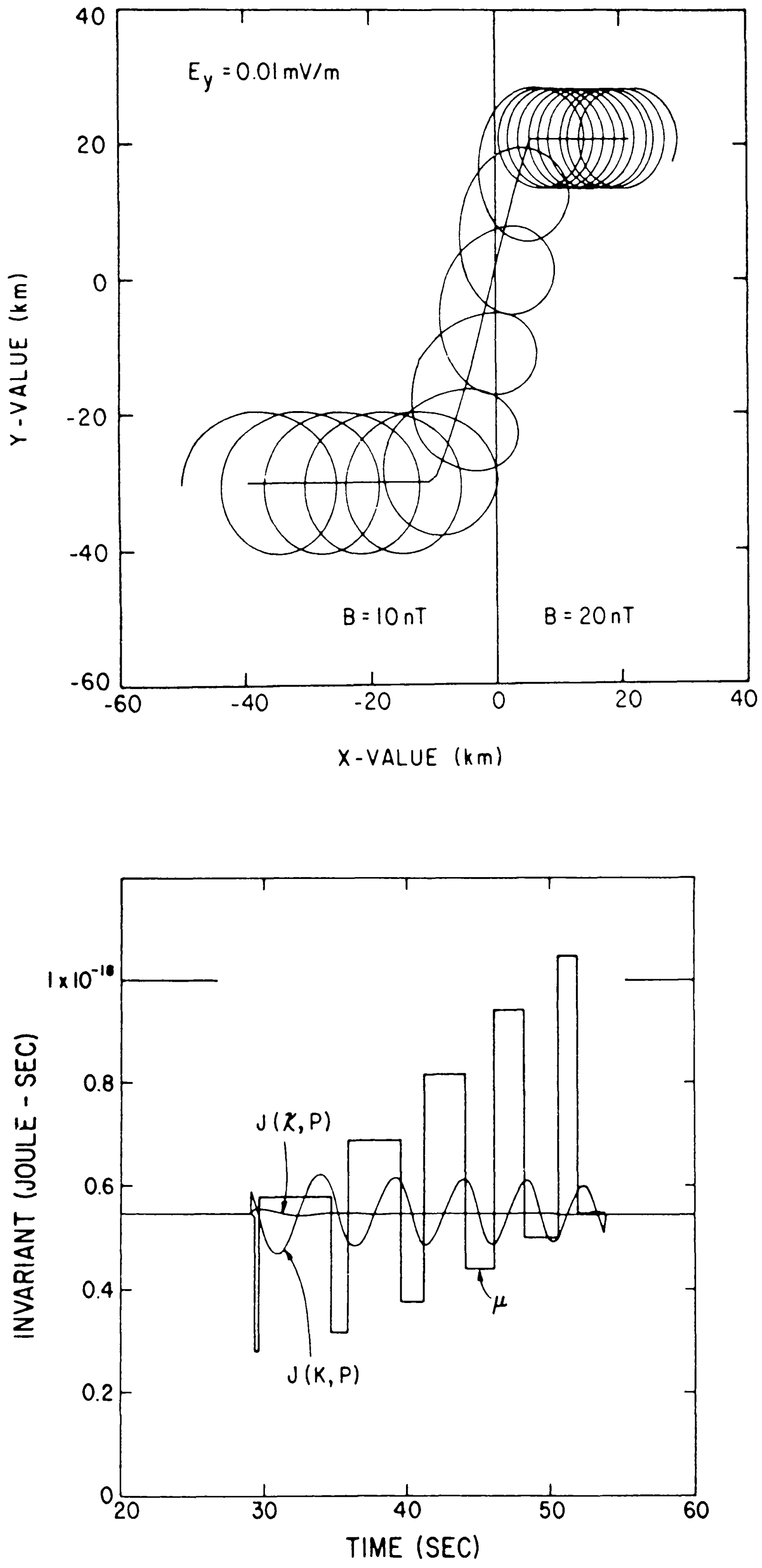

Fig. 9. *Top*: Projection onto $(x - y)$-plane of particle incident on perpendicular shock. *Bottom*: Evolution during orbit of particles magnetic moment (μ), measured in local plasma frame, and generalized invariant J (adapted from Whipple *et al.*, 1986).

drift acceleration in a form more easily comparable to observations, one can use time-reversed orbit integrations or derive the time-reversed versions of Equations (32)–(40), and then invoke Liouville's theorem to construct 'observed' particle distributions given a plausible form of the pre-acceleration distribution function (Decker, 1981, 1983; Kessel, 1986).

Figure 10 shows predicted, steady-state, omni-directional fluxes immediately upstream and downstream of a quasi-perpendicular shock ($B_2/B_1 = 3$) after a single drift encounter under scatter-free conditions. Adiabatic test particle equations were used in this case and the ambient or pre-acceleration flux was assumed isotropic with a power-law energy dependence, $j_{\text{ambient}} \sim E^{-\gamma}$, with $\gamma = 3$ (other distributions are examined in Decker, 1983). The abscissa is the final (f) or post-acceleration energy E_f (measured in the appropriate plasma frame) scaled in terms of the transformation energy E_1 from frame K_1 to frame K', i.e., $E_f/E_1 = \varepsilon_f^{-2}$, where $\varepsilon_f = U_1 \sec\theta_1/v_f$ and v_f = final particle speed. For $E_f = E_f^* \sim 2.5E_1$, the fluxes upstream (j_U) and downstream (j_D) are comparable, while for $E_f > E_f^*$, $j_U > j_D$. For $E_f < E_f^*$, j_U drops rapidly from a peak near E_f^* to the ambient flux for $E_f < E_1$, which expresses the simple kinematical constraint that particles are unable to escape upstream when $v_f < U_1 \sec\theta_1$. With decreasing energy below $E_f \sim E_1$, j_D approaches the limiting flux expected for an isotropic distribution incident on a perpendicular shock, i.e., the post-shock spectrum is the incident spectrum shifted to the right. The ratio of the accelerated flux to the ambient flux (i.e., the enhancement) at a given energy increases as B_2/B_1 and/or the slope γ of the ambient spectrum increase. On the basis of the simple example in Figure 10, one expects that when quasi-static conditions obtain near a laminar, quasi-perpendicular shock, peak flux enhancements should shift from upstream to downstream with decreasing particle energy. This is a well-known consequence of single-encounter drift acceleration that has been observed during shock-spike events at interplanetary shocks (e.g., Sarris *et al.*, 1976; Decker *et al.*, 1981; Balogh and Erdös, 1981; Armstrong *et al.*, 1985; Sarris and Krimigis, 1985).

3.6. PREDICTED PITCH ANGLE DISTRIBUTIONS AT QUASI-PERPENDICULAR SHOCKS

Figure 11 shows predicted flux enhancements in the plasma frame as a function of final pitch cosine $\mu_f = \cos\alpha_f$ for particles in the three energy ranges A, B, and C shown at the top of Figure 10. The smaller values $B_2/B_1 = 2$ and $\gamma = 2$ yield enhancements in Figure 11 that are smaller than those in Figure 10; however, the energy dependence of features in j_U and j_D in Figure 10 is unchanged. For the upstream region in Figure 11, $\mu > 0$ is away from the shock, $\mu < 0$ is toward the shock, and *vice-versa* downstream (this convention is opposite to that used in Figure 7). In range A, the downstream distribution peaks at $\mu_f \sim 0.5$, so these particles are headed back toward the shock along $\mathbf{B}_{02}$ with $\alpha_f \sim 60°$. In range B, the enhancement upstream peaks away from the shock nearly parallel to the field, while that downstream (as in A) peaks in the shockward pitch angle hemisphere. As energy increases from B to C, the enhancement upstream, although remaining large, becomes somewhat less field-aligned, while that downstream decreases and peaks more nearly perpendicular to $\mathbf{B}_{02}$.

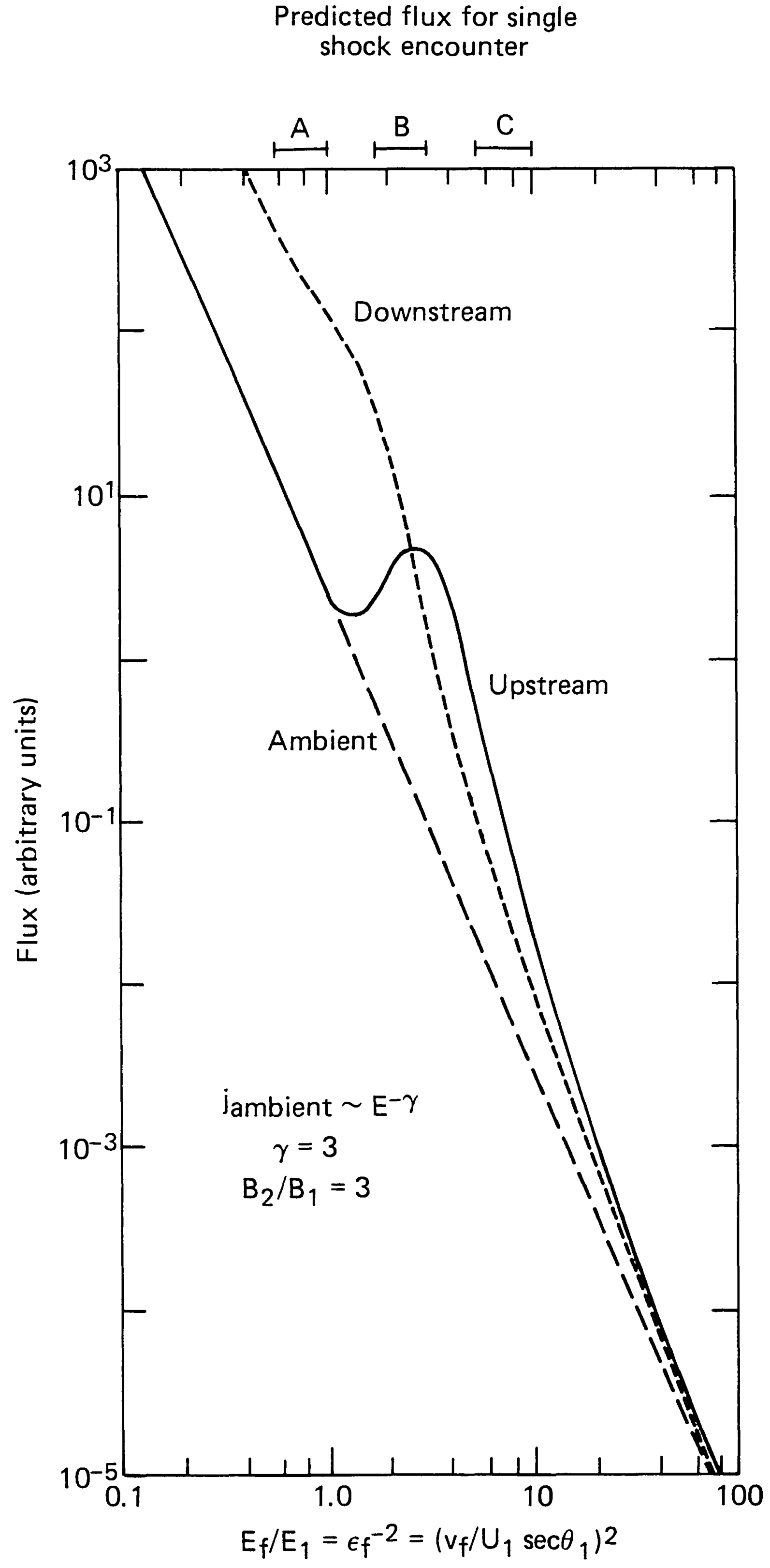

Fig. 10. Predicted steady-state energy spectra after single encounter with quasi-perpendicular shock. Energy E_f is in units of transformation energy E_1 into de Hoffmann-Teller frame (adapted from Decker, 1983).

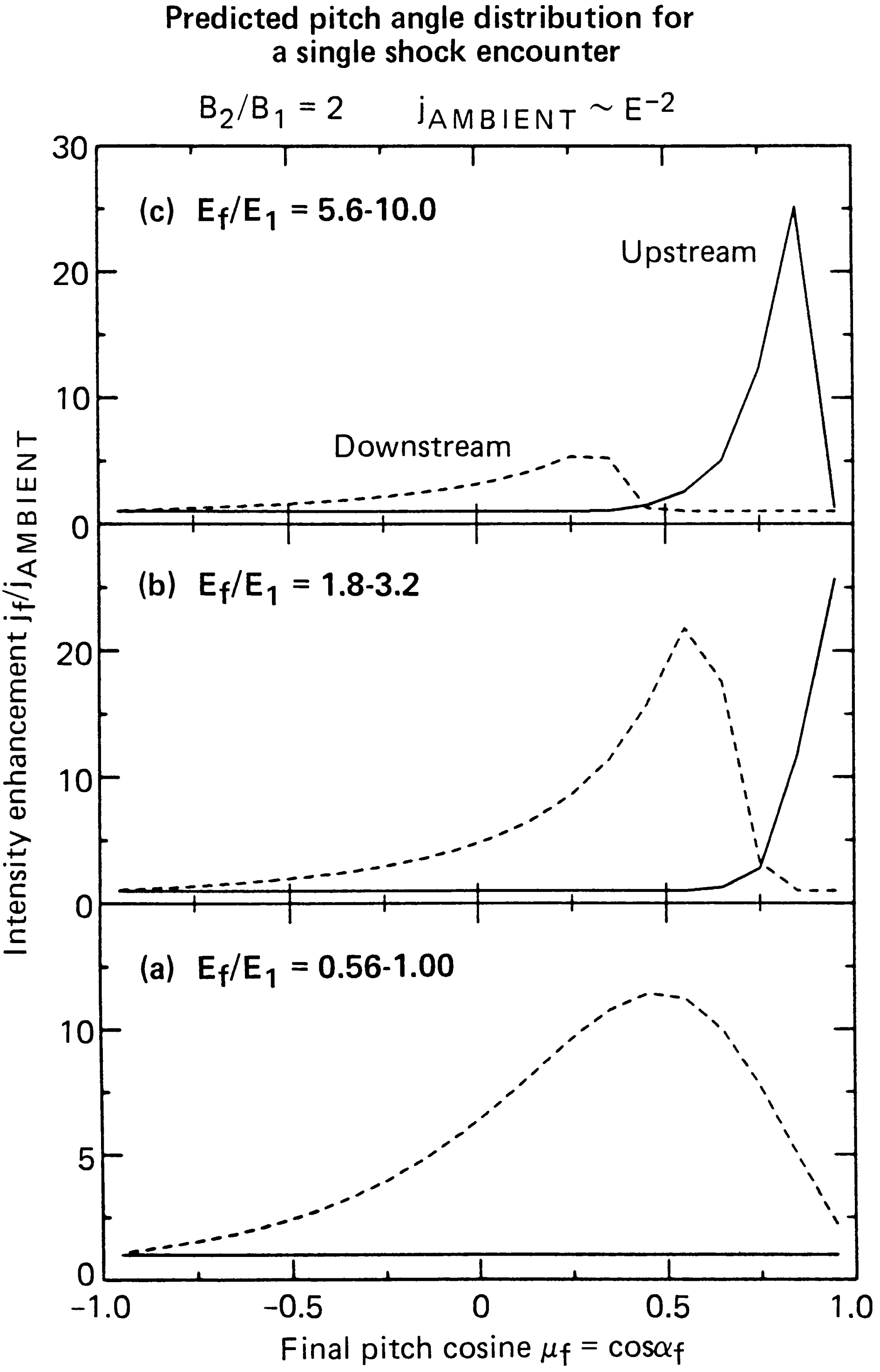

Fig. 11. Predicted pitch angle cosine distributions for three energy ranges at top of Figure 10. Field jump is B_2/B_1 and slope of ambient energy spectrum is $\gamma = 2$.

Angular distributions showing clear signatures of single-encounter drift acceleration have been observed at the Earth's bow shock (e.g., Anagnostopoulos and Sarris, 1983; Vandas *et al.*, 1986) and at many interplanetary shocks (Armstrong *et al.*, 1970, 1985; Singer and Montgomery, 1971; Potter, 1981; Pesses *et al.*, 1984; Sanderson *et al.*, 1985; Sanderson, 1984; Balogh and Erdös, 1985; Kessel, 1986). Figure 12 shows plasma-

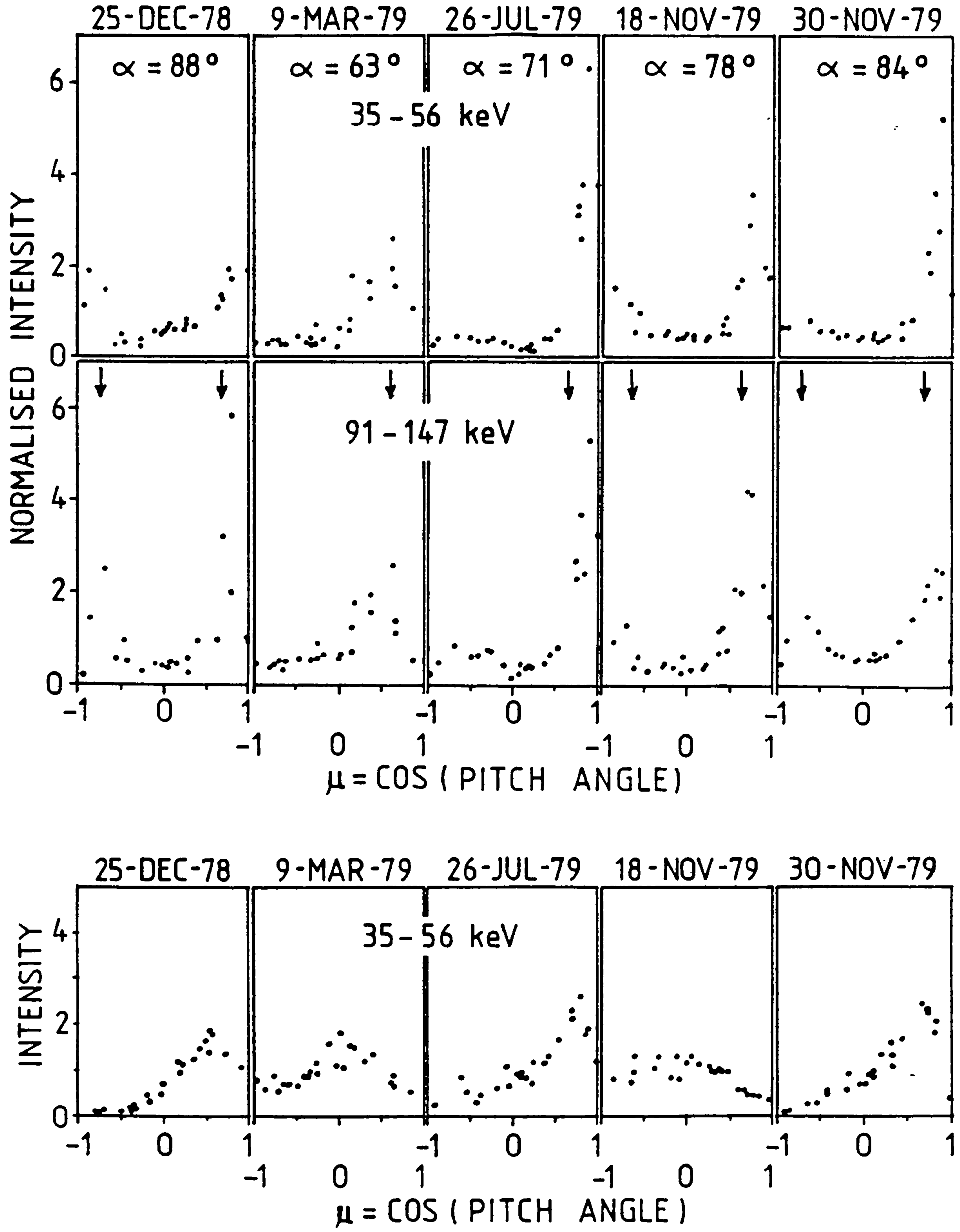

Fig. 12. Plasma-frame pitch angle cosine distributions of ions measured upstream (*top two rows*) and downstream (*bottom row*) of five quasi-perpendicular interplanetary shocks observed at ISEE-3. Here, $\theta_1 = \alpha$. Arrows in 91–147 keV channel denote position of peak intensity predicted by theory (adapted from Balogh and Erdös, 1985).

frame pitch angle cosine distributions of ions measured upstream (top two rows) and downstream (bottom row) of five quasi-perpendicular interplanetary shocks observed at ISEE-3. Event times and shock obliquity ($\theta_1 = \alpha$ in Figure 12) are as indicated. Arrows in the 91–147 keV channel denote peak intensity positions as expected from theory. Three events exhibit double peaks upstream, which the authors attribute to loop-like upstream field structures that intersect the shock at two points, thus producing oppositely-directed beams at the spacecraft (Balogh and Erdös, 1985). Three of the downstream distributions peak at pitch angles directed back towards the shock ($\mu > 0$), while the other two peak nearly perpendicular to the downstream field. In one event

(30 November, 1979), a shift in the peak of the downstream distribution from $\mu > 0$ toward $\mu = 0$ with increasing energy was clearly identifiable (not shown here). These observations are in excellent qualitative agreement with predicted features of drift acceleration in Figure 11.

The model predictions in Figures 10 and 11 were derived from steady-state acceleration at a planar shock with uniform fields upstream and downstream; consequently, shock-accelerated distributions would in principle fill the infinite half-spaces on either side of the shock. However, as implied by their name, shock spike events, which have provided the clearest observational evidence of single-encounter drift acceleration, are rather narrow ($\sim$ 1 hour or so at the spacecraft) and are confined very close to the shock. These shocks are generally nearly perpendicular, so interplanetary magnetic field (IMF) lines are nearly parallel to the shock surface, and the distance s between the spacecraft and the shock along a field line can be a sizeable fraction of an AU. For example, one hour prior to arrival of a shock with speed $V_s = 600 \text{ km s}^{-1}$, $s = V_s t \sec \theta_1 \sim 0.1$ AU for $\theta_1 = 82°$. It is clear that large-scale directional fluctuations in the IMF, finite shock curvature, and surface fluctuations on the shock itself (e.g., Grazis *et al.*, 1985) will limit or prevent shock connection when the spacecraft is not in the immediate vicinity of the shock, thereby limiting the width of shock spike enhancements. Pitch angle scattering off ambient magnetic fluctuations will also limit the spike width, although scattering must be weak enough to preserve large anisotropies such as those in Figure 12.

3.7. EFFECTS OF CHARGE TO MASS RATIO AND INJECTION CRITERIA

Under static and uniform conditions at a planar shock discontinuity, there is no natural scale time and scale length, so the dynamics is independent of a particle's charge to mass ratio. Thus, two particles with the same initial momentum end up with the same post-encounter momentum. For example, two different ion species with the same energy per nucleon and pitch angle have the same final energy per nucleon and pitch angle following a drift encounter. However, both the shock encounter time τ and drift distance d along the shock surface scale as q/m. If for a proton we denote these quantities by τ_p and d_p, then for ion species σ with the same initial momentum, $\tau_\sigma = (A/Z^*)\tau_p$ and $d_\sigma = (A/Z^*)d_p$, where A and Z^* are the ion's atomic mass number and charge state, respectively. For instance, compared to a proton with the same initial momentum, an alpha particle drifts twice as far and takes twice as long to do so. For electrons, $\tau_e = (m_e/m_p)\tau_p$ and $d_e = (m_e/m_p)d_p$. Therefore, q/m effects can become extremely important when the shock is curved or supports a spectrum of surface fluctuations, when a spectrum of field fluctuations is present and, of course, when the finite shock thickness is properly introduced into the problem. For example, in the presence of low-frequency MHD waves, the ion dynamics will be complex, while the electrons may undergo relatively undisturbed drift interactions.

For ions, there are two important considerations with regard to the problem of injection into the drift process. The first is the purely kinematical requirement that reflection of an incident particle is possible only if its initial velocity v_0 exceeds or is comparable to the velocity of the shock along the upstream field line, i.e., $v_0 \gtrsim U_1 \sec\theta_1 \cos\delta_1$, or $v_0/V_1 \gtrsim 1$. This criterion is important because reflected particles can undergo multiple shock encounters and attain high energies if there is a mechanism for sending them back to the shock. However, this criterion can also be quite severe at nearly-perpendicular shocks. The second consideration is the thin shock assumption, $r_g \gg L_s$, which, for fixed L_s, breaks down with decreasing particle energy and, for fixed r_g, breaks down as θ_1 decreases, since the thin, laminar transitions at quasi-perpendicular shocks give way to broad, turbulent transitions at quasi-parallel shocks. The effect of $r_g \sim L_s$ on ion acceleration at quasi-perpendicular shocks will be discussed in Section 5.

3.8. DRIFT ACCELERATION AT SLOW-MODE SHOCKS

There are no reported numerical studies of test particle interactions with slow-mode shocks. However, based upon our experience with fast-mode shocks, it is reasonable to expect that adiabatic test particle theory should provide a reasonable picture under static and uniform conditions. Equations similar to (32)–(40) describing scatter-free

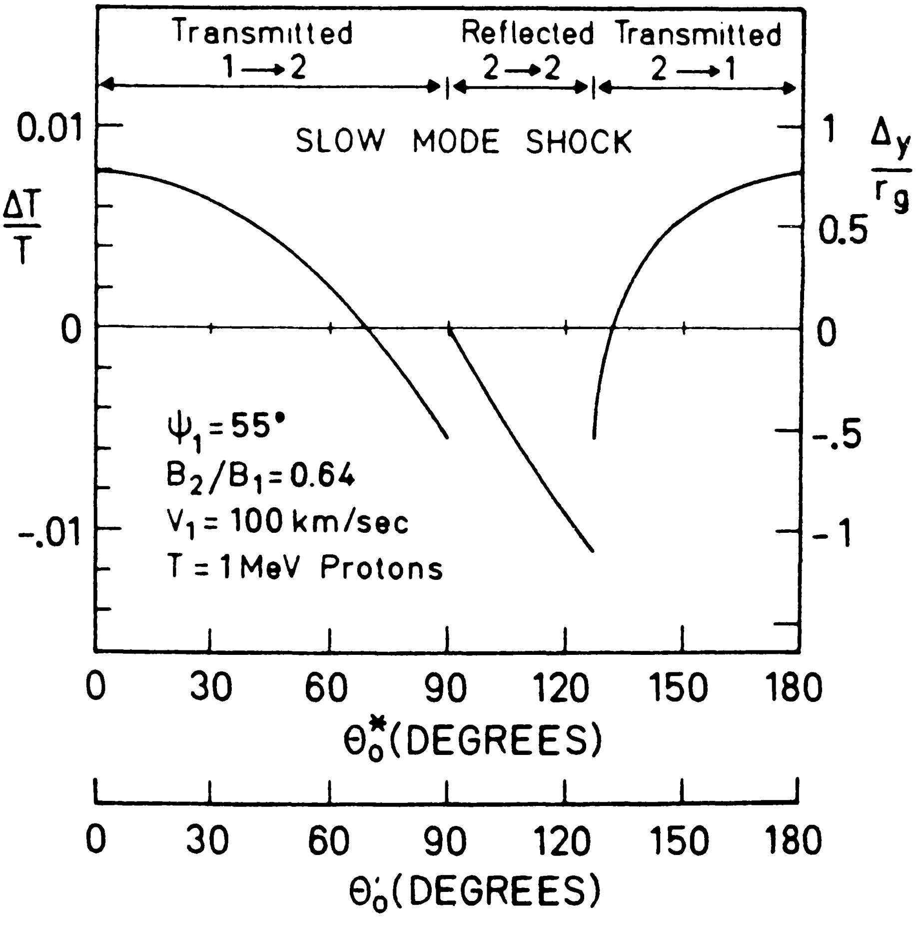

Fig. 13. Fractional energy change $\Delta T/T$ versus initial particle pitch angle θ_0^* in shock frame (or θ_0' in de Hoffmann-Teller frame). Here, $\psi_1 = \theta_1 = 55°$, $T = 1$ MeV, $V_1 = U_1 = 100$ km s^{-1}, and $B_2/B_1 = 0.64$. Particles incident from upstream are all transmitted downstream ($1 \to 2$); those incident from downstream are either reflected ($2 \to 2$) or transmitted upstream ($2 \to 1$) (from Webb *et al.*, 1983).

1988SSRv...48..195D

single-encounter interactions with slow-mode shocks have been given in the plasma frames by Pesses *et al.* (1982) and in the shock frame by Webb *et al.* (1983). Figure 13, from Webb *et al.* (1983), shows the fractional kinetic energy change $\Delta T/T$ versus the particle's initial pitch angle θ_0^* in the shock frame K or θ_0' in the HT frame K'. Here, $\theta_1(\psi_1) = 55°$, $T = 1$ MeV, $U_1(V_1) = 100\ \text{km s}^{-1}$ and $B_2/B_1 = 0.64$ (recall that across a slow-mode shock, the field is refracted away from the shock surface and is decreased in magnitude). Particles incident from upstream are all transmitted downstream ($1 \rightarrow 2$), while those incidents from downstream are either reflected ($2 \rightarrow 2$) or transmitted upstream ($2 \rightarrow 1$). In contract to the case of a fast-mode shock, the reflected and transmitted particles with $70° \lesssim \theta_0^* \lesssim 130°$ *lose* energy, while the transmitted particles with θ_0^* more closely field-aligned *gain* energy. Webb *et al.* (1983) attribute energy losses to predominance of the effective gradient drift, which drives particles anti-parallel to ε_0, and energy gains to predominance of the effective curvature drift, which drives particles parallel to ε_0. Follow-up studies of these predictions using orbit integrations would be of interest, particularly with ambient magnetic fluctuations introduced (see Section 4). Because slow-mode shocks are extremely rare in the interplanetary medium, observational verification of these results is as yet unavailable.

4. Test Particle Interactions with a Shock Discontinuity: Magnetic Fluctuations, Pitch Angle Scattering, and Multiple Shock Encounters

We showed in the previous section that particle motion through an infinitesimally thin planar shock for static and uniform conditions upstream and downstream can be calculated exactly using the fast crossing-time numerical algorithm, or can be approximated by the adiabatic test particle relations based upon magnetic moment conservation. In this section we describe a technique for introducing magnetic fluctuations into the problem, and discuss how these fluctuations modify single-encounter drift acceleration as compared with the scatter-free case. This comparison shows that stochastic processes produce interesting modifications to the drift acceleration process. However, focusing upon a single encounter is rather artificial, since the presence of magnetic fluctuations can generally return particles to the shock. Specifically, on a time-scale much larger than the duration of a typical drift encounter, magnetic fluctuations will produce spatial diffusion via pitch angle scattering, resulting in a few particles that can attain very high energies by experiencing multiple shock encounters. This is the process of multiple-encounter shock acceleration. With respect to the shock frame K, this process can be viewed as including both the drift and first-order Fermi acceleration processes. We shall describe specific applications of the multiple-encounter code, and discuss how recent numerical studies compare with predictions from diffusive shock acceleration theory.

4.1. GENERATION OF MAGNETIC FIELD FLUCTUATIONS

Here we describe a method that has been used to synthesize a field of random magnetic field fluctuations on one or both sides of the shock (e.g., Decker and Vlahos, 1986a).

We shall confine our attention to ion acceleration, and therefore are interested primarily in low-frequency, transverse magnetic fluctuations of the MHD variety. We shall consider two types of computer experiments that differ in how one relates the upstream and downstream random field components. In the first type of experiment (type I), the random field realizations are independently generated on each side of the shock. In the second type of experiment (type II), the random field downstream is generated by passing each vector of the upstream field through the R–H jump conditions. We describe each type in turn.

For the type I experiment, one introduces magnetic fluctuations into the model by adding to the constant field $\mathbf{B}_{0i}$ ($i = 1$ or 2) the random field $\mathbf{b}_i(z_i)$, i.e.,

$$\mathbf{B}_i(z_i) = \mathbf{B}_{0i} + \mathbf{b}_i(z_i) \tag{41}$$

is the total field, where $\mathbf{b}_i$ is formed by superposing a large number N of monochromatic, circularly polarized Alfvén waves with random phases and with wave vectors $\mathbf{k}$ aligned either parallel or anti-parallel to $\mathbf{B}_{0i}$. The random field $\mathbf{b}_i$ has zero mean, is transverse to $\mathbf{B}_{0i}(\mathbf{b}_i \cdot \mathbf{B}_{0i} = 0)$, and in frame K_i varies only with coordinate z_i along $\mathbf{B}_{0i}$ and is static (i.e., we neglect wave phase velocities so that pitch angle scattering is elastic in the plasma frames). Realizations of $\mathbf{b}_i$ are generated separately for the upstream and downstream regions, and the R–H jump conditions are satisfied on average, i.e., $\langle \mathbf{B}_i(z_i) \rangle = \mathbf{B}_{0i}$, since $\langle \mathbf{b}_i(z_i) \rangle = 0$ (angle brackets denote an ensemble average).

For the type II experiment, one treats the total field changes across the shock more carefully. One first generates a realization $\mathbf{b}_1(z_1)$ of the upstream random field, as described in the previous paragraph, and forms the total field $\mathbf{B}_1(z_1) = \mathbf{B}_{01} + \mathbf{b}_1(z_1)$. Then the total downstream field vector $\mathbf{B}_2(z_2) = \mathbf{B}_{02} + \mathbf{b}_2(z_2)$ is calculated by requiring that the R–H conditions be satisfied pointwise at the shock; thus, the downstream field is the shock-processed upstream field.

Spatial realizations of $\mathbf{b}(z) = \hat{x}b_x(z) + \hat{y}b_y(z)$ are generated in this slab model using the following algorithm (subscript i is temporarily dropped for convencience). Let $\{b(z)\}$ be a zero mean, homogeneous random process, such that $\{b(z)\}$ denotes the ensemble of real-valued functions $b(z)$ (here $b(z)$ can stand for $b_x(z)$ or $b_y(z)$) of the spatial variable z, $-\infty < z < \infty$. Let $b(z)$ be a particular sample record or realization of $\{b(z)\}$ that consists of N points evenly spaced a distance h_b apart on the finite interval $[0, L]$. Let $N = 2^p$ (p = integer ≥ 0), and define

$$b_n = b(z = z_n = nh_b), \quad 0 \leq n \leq N - 1, \tag{42}$$

as the value of $b(z)$ at each of the N discrete points. Then, the grid spacing is $h_b = L/(N - 1) = \tilde{L}/N$, where $\tilde{L} = L + h_b$. For convenience in applying periodic boundary conditions to the realization along z, we define the additional point $b_N = b_0$ in (42), so there are now $N + 1$ points on $[0, \tilde{L}]$. We relate h_b to the correlation length z_c of the random field by $h_b = z_c/2^q$ where q is a positive integer, $0 \leq q \leq p$. Given p, q, and z_c, the realization length $\tilde{L} = Nh_b = 2^{p-q}z_c$, so there are $2^{p-q} \geq 1$ correlation lengths per interval $\tilde{L}$, with 2^q grid points per z_c (roughly speaking, two values of $\mathbf{b}(z)$ separated by z_c will, on average, be completely different in magnitude or direction, or both).

The technique of synthesizing a realization of $b(z)$ is most easily understood by considering how one would obtain the finite Fourier transform of the N points of $b(z)$ on the interval $[0, L]$ (e.g., Owens, 1978; Brinca, 1984; Decker and Vlahos, 1986a). In this case,

$$a_m = \sum_{n=0}^{N-1} b_n e^{-ik_m z_n}, \quad m = 0, 1, 2, \ldots, N-1, \tag{43}$$

where

$$k_m = 2\pi m/(Nh_b) = 2\pi m/\tilde{L} \tag{44}$$

is the wavenumber corresponding to wavelength $\lambda_m = \tilde{L}/m$, and is associated with Fourier coefficient a_m. The inverse transform is

$$b_n = N^{-1} \sum_{m=0}^{N-1} a_m e^{ik_m z_n}, \quad n = 0, 1, 2, \ldots, N-1. \tag{45}$$

For real b_n, only half of the a_m are unique, with $a_{N-n} = a_m^*$, $m = 1, 2, 3, \ldots, N/2 - 1$, where the asterisk denotes complex conjugate, a_0 and $a_{N/2}$ are real, and $a_0 = 0$, so $b(z)$ has zero mean. The largest and smallest wavenumbers k_L and k_S, respectively, are then

$$k_L = k_{N/2} = \pi/h_b = \pi 2^q/z_c, \tag{46}$$

and

$$k_S = k_1 = 2\pi/\tilde{L} = 2^{-p+1} k_L, \tag{47}$$

so that $k_L/k_S = 2^{p-1}$.

An estimate of the one-sided (i.e., $0 \le k < \infty$) wavenumber power spectrum $P(k)$ at k_m is (Bendat and Piersol, 1971)

$$P_m = P(k_m) = (2h_b/N)\,|a_m|^2. \tag{48}$$

Note that, given P_m, only the modulus $|a_m|$ of each a_m is recoverable from Equation (48). Thus, the a_m are not uniquely defined for use in (45). As suggested by Owens (1978), one can generate the phase angles ϕ_m of the a_m randomly from a distribution uniform over the interval $0 \le \phi_m < 2\pi$, and use $|a_m| = (NP_m/2h_b)^{1/2} = N(P_m/2\tilde{L})^{1/2}$ to obtain

$$a_m = |a_m|\, e^{i\phi_m} = N(P_m/2\tilde{L})^{1/2} e^{i\phi_m}. \tag{49}$$

Upon taking the complex conjugate of (45) and (49) and requiring the b_n to be real, one obtains

$$b_n = \sum_{m=0}^{N-1} A_m e^{-ik_m z_n}, \tag{50}$$

where

$$A_m = (P_m/2\tilde{L})^{1/2} e^{i\phi_m}. \tag{51}$$

1988SSRv...48..195D

Equation (51) is in exactly the same form as (43), so fast Fourier transform (FFT) algorithms routinely used to Fourier analyze real input data b_n by generating the a_m via (43) can also be used to synthesize a particular realization of the b_n from the coefficients A_m in (51) once P_m and the random ϕ_m are given. The A_m also satisfy $A_{N-m} = \mathrm{A}_m^*$, $m = 1, 2, 3, \ldots, N/2 - 1$, where again we set $A_0 = 0$. Thus, each set of the random ϕ_m, $m = 1, 2, 3, \ldots, N/2 - 1$, generates one particular realization of $b(z)$ on $[0, L]$. As pointed out by Owens (1978), one can generate two field realizations with one use of the FFT on Equation (50). Then, by appropriate choice of the phase difference between the corresponding ϕ_m of each realization, one can simultaneously generate the x- and y-components of a random field **b** that is a superposition of Fourier components with particular polarizations, e.g., left- or right-hand circular polarization.

One can obtain the amplitudes of the Fourier coefficients in (51) by assuming a one-sided wavenumber power spectral density $P(k)$ of the general form

$$P_\beta(k) = \frac{A_\beta z_c (\Delta B)^2}{1 + (kz_c)^\beta}\,, \quad (k_S \leq k \leq k_L)\,, \tag{52}$$

where β is the spectral exponent,

$$(\Delta B)^2 = \langle b^2 \rangle \tag{53}$$

is the variance of the random field, and A_β is the normalization constant, such that

$$\int_{k_S}^{k_L} \mathrm{d}k P_\beta(k) = (\Delta B)^2\,. \tag{54}$$

For typical values of k_S and k_L we shall consider, only a small error is incurred if for $(\Delta B)^2$ given, one uses $A_\beta = (\beta/\pi)\sin(\pi/\beta)$, $1 < \beta < \infty$, and replaces the integration limits in (54) by 0 and ∞. (For power spectra with the normalization defined in (54), it is necessary to multiply by a factor of 2π before using in Equation (51).)

For a type I experiment, $\mathbf{b}_i \cdot \mathbf{B}_{0i} = 0$ on both sides of the shock. For a matched-field, type II experiment, $\mathbf{b}_1 \cdot \mathbf{B}_{01} = 0$, but generally, $\mathbf{b}_2 \cdot \mathbf{B}_{02} \neq 0$, i.e., there is a component of $\mathbf{b}_2$ parallel to as well as perpendicular to $\mathbf{B}_{02}$. For $\mathbf{b}_1(z_1) = \hat{x}_1 b_{1x}(z_1) + \hat{y}_1 b_{1y}(z_1)$ relative to the K_1 coordinate system, then

$$b_{2x} = \frac{r}{(\cos^2\theta_1 + r^2 \sin^2\theta_1)^{1/2}}\, b_{1x}\,, \tag{55a}$$

$$b_{2y} = r b_{1y}\,, \tag{55b}$$

$$b_{2z} = \frac{(1 - r^2)\cos\theta_1 \sin\theta_1}{(\cos^2\theta_1 + r^2 \sin^2\theta_1)^{1/2}}\, b_{1x}\,, \tag{55c}$$

where we have assumed $\xi \sim 1$ (i.e., $M_{\mathrm{A}1}^2 \gg 1$ in Equation (12)) and that r and θ_1 on the right-hand side of Equation (55) are the unperturbed values. By definition, $\langle b_{1x} \rangle = 0$, so, $\langle b_{2x}\rangle = \langle b_{2y}\rangle = \langle b_{2z}\rangle = 0$. The r.m.s. amplitudes $\Delta B_{2_{\|}} = (\langle b_{2z}^2\rangle)^{1/2}$ and $\Delta B_{2_{\perp}} = (\langle b_{2x}^2\rangle + \langle b_{2y}^2\rangle)^{1/2}$ are calculable for given shock parameters and $\Delta B_{1x} = (\langle b_{1x}^2\rangle)^{1/2}$ and $\Delta B_{1y} = (\langle b_{1y}^2\rangle)^{1/2}$. For a type II experiment, the N vectors of $\mathbf{B}_2(z_2)$ are generated by imposing the R–H conditions on each of the N vectors of $\mathbf{B}_1(z_1)$. In order to retain the computationally convenient condition of magnetostatic scattering in plasma frame K_2, one must also neglect any associated perturbations that would produce a deviation in the downstream flow from its unperturbed value $\mathbf{U}_2$. Within this approximation, one can show that, pointwise, the normal component of the total magnetic field is continuous across the shock, while the tangential electric field is continuous across the shock through first order in $M_{\mathrm{A}1}^{-1}$ (Decker, 1988).

More careful and detailed analyses of the transmission of Alfvén waves through oblique shocks have been performed, most notably by McKenzie and Westphal (1969) and Achterberg and Blandford (1986). In the latter paper, the authors considered the transmission of circularly polarized Alfvén waves through a strong ($M_{\mathrm{A}1}^2 \gg 1$) shock and calculated the subsequent damping of the resultant downstream wave modes in the high-beta downstream plasma. The work of Achterberg and Blandford (1986) was restricted to effects that were linear in full set of MHD variables. This level of sophistication is beyond the scope of present numerical studies of test particle acceleration at oblique shocks, which have been concerned only with changes in the magnetic field across the shock and have neglected any processes leading to damping of the downstream waves.

Figure 14 shows sample power spectra for $\beta = 1$ and $\frac{5}{3}$ (left) and a section of the resultant magnetic fluctuations (right) for $\beta = \frac{5}{3}$. A field of magnetic fluctuations composed of left-hand circularly polarized Alfvén waves upstream of the shock was generated using the following set of parameters: $\beta = \frac{5}{3}$ (solid) and 1 (dashed) (i.e., for $kz_c \gg 1$, $P_\beta(k) \sim k^{-5/3}$ and k^{-1}, respectively), $p = 12$, $q = 6$, $z_c = 10^5$ cm, $B_{01} = 50$ G, and $U_1 = 3.3 \times 10^8$ cm s^{-1} (the speed of a 57 keV proton). Then, the number of Fourier components $N = 4096$, the grid spacing $h_b = z_c/2^6 = 1.6 \times 10^3$ cm, the realization length $L = 2^6 z_c = 6.4 \times 10^6$ cm, $k_S = 9.8 \times 10^{-7}$ cm^{-1}, and $k_L = 2.0 \times 10^{-3}\, cm^{-1}$. These parameters for $\beta = \frac{5}{3}$ were used in a study by Decker and Vlahos (1985a, 1986a) to characterize ion acceleration at solar flare shocks. The nonrelativistic proton gyrofrequency $\Omega_1 = eB_{01}/m_{0p}c = 4.8 \times 10^5$ s^{-1}, and the lengths k_L^{-1}, z_c, and k_S^{-1} correspond to upstream gyroradii r_g of protons with kinetic energies ~ 30 keV, ~ 800 keV, and ~ 14 GeV, respectively. Thus, power for resonant pitch angle scattering ($k \sim r_g^{-1}$) was available over the range of proton energies from ~ 100 keV to ~ 1 GeV relevant to solar flare acceleration. The upstream variance $(\Delta B_1)^2$ was $0.2B_{01}^2$; thus, $(\Delta B_{1x})^2 = (\Delta B_{1y})^2 = 0.1B_{01}^2$. The bottom panel of Figure 14(b) shows $b_{1x}(z_1)/B_{01}$ versus z_1 (units of z_c) for a short segment of the realization. The upper panel of Figure 14(b) shows the difference $\theta_1(z_1) - \theta_{01}$ between the instantaneous value of θ_1 and the mean value θ_{01} calculated using $\mathbf{B}_{01}$. Although $\langle \theta_1(z_1)\rangle = \theta_{01}$ when averaged over the entire realization, fluctuations about θ_{01} of ~ 20° $\simeq \Delta B_{1x}/B_{01}$ or more are common. These fluctuations are significant to charged particles that respond to the local θ_1, not θ_{01}, at shock crossings.

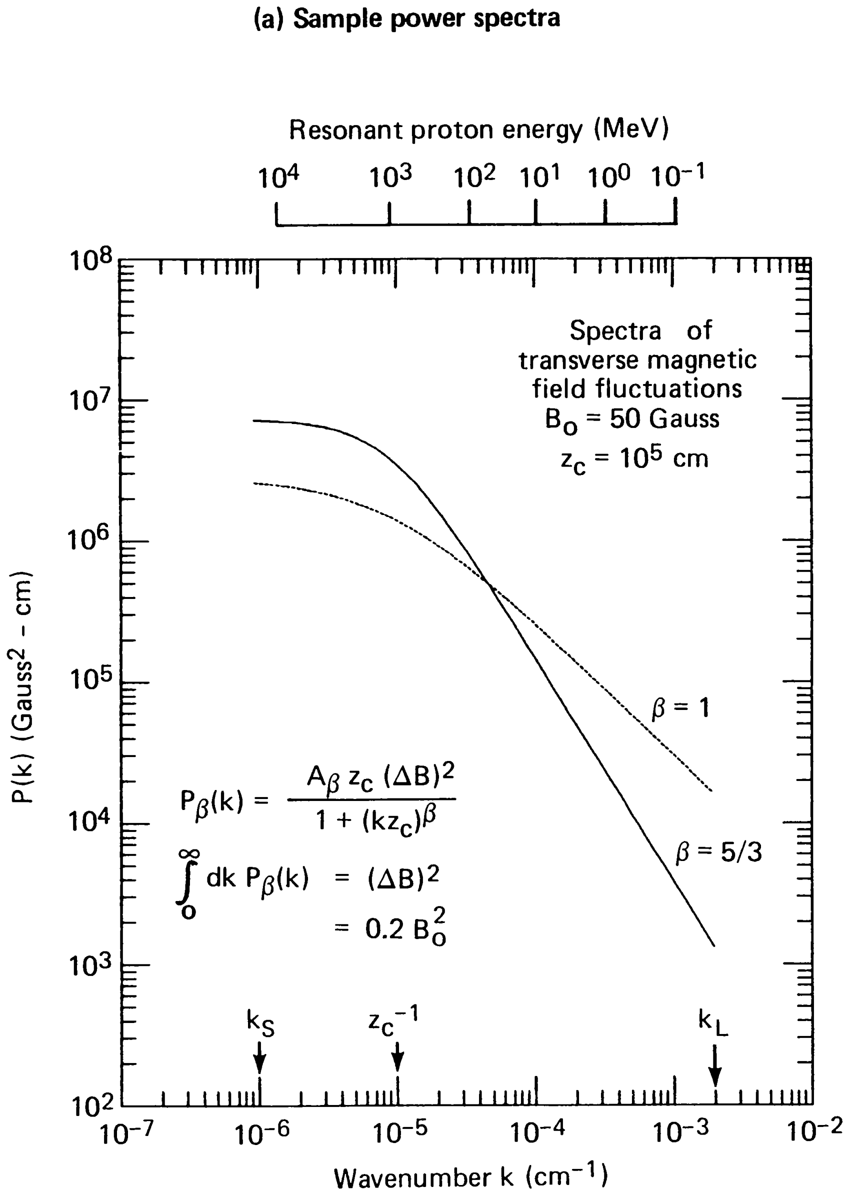

(a) Sample power spectra

Fig. 14. (a) Sample wavenumber power spectral densities for spectral slopes $\beta = 1$ and $\frac{5}{3}$. Top scale shows gyroradius r_g of proton for which $r_g = k^{-1}$. (b) *Lower panel*: Section of realization of random magnetic field component b_x versus distance z along ambient field $\mathbf{B}_0$ (z_c = correlation length of random field). *Top panel*: Difference between average upstream angle θ_0 and instantaneous angle $\theta(z)$.

For given field realizations $\mathbf{B}_1(z_1)$ and $\mathbf{B}_2(z_2)$, one proceeds by numerically integrating Equations (16) and (17) along exact $[\mathbf{x}_i, \mathbf{p}_i]$ phase space orbits in plasma frame K_i. Equation (27a) is continually monitored to determine shock crossings (i.e., x reverses sign), in which case one performs Lorentz transformations between plasma frames given in Equations (22)–(25). One assumes periodic boundary conditions on the realizations $\mathbf{B}_1(z_1)$ and $\mathbf{B}_2(z_2)$, i.e., that each is reproduced indefinitely upstream and downstream of the shock, respectively. For a given particle coordinate z_p, one uses linear interpolation between discrete field vectors on each side of z_p to calculate $\mathbf{B}_i(z_p)$. Each particle orbit is followed until a specified temporal or spatial boundary (e.g., loss boundary) is crossed, whereupon new field realizations are generated if desired, and the procedure

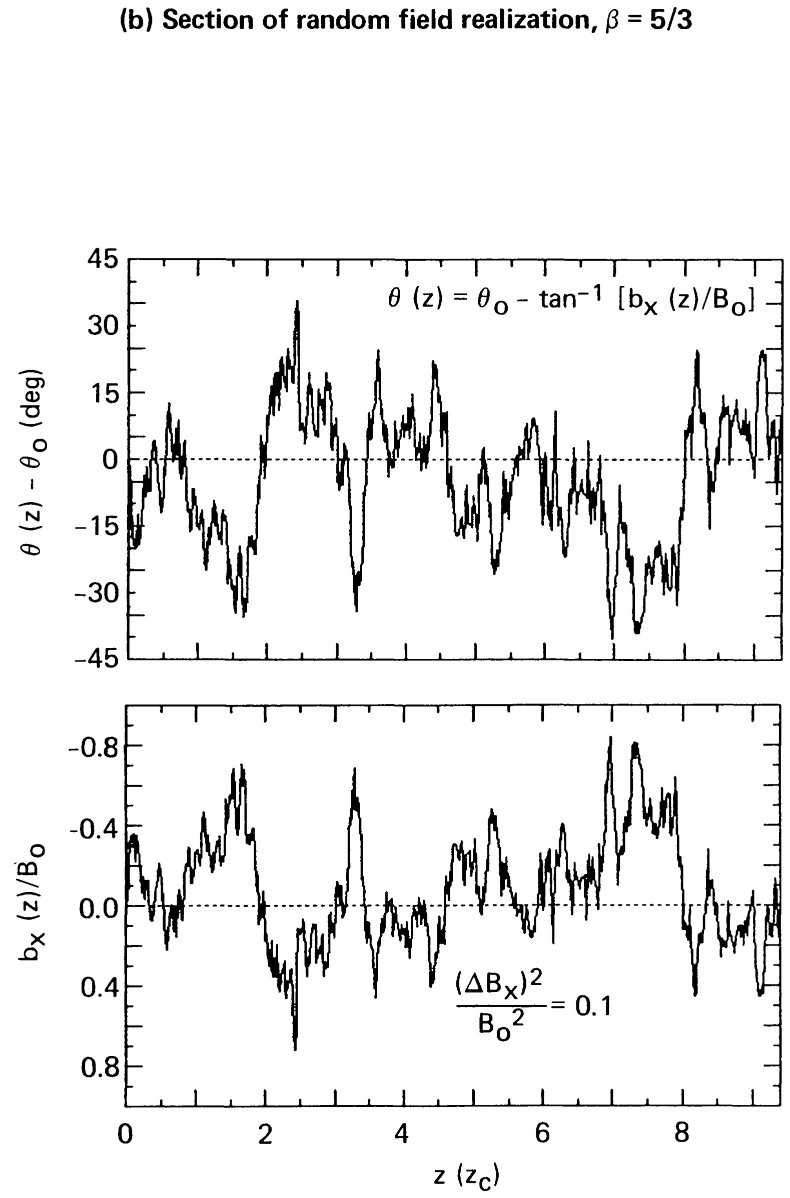
(b) Section of random field realization, $\beta = 5/3$

repeated for a new particle. Lorentz transformations are performed to obtain phase space coordinates $[\mathbf{x}, \mathbf{p}]$ in shock frame K given those $[\mathbf{x}_i, \mathbf{p}_i]$ in plasma frame K_i using Equations (18) and (19).

4.2. EFFECTS OF MAGNETIC FLUCTUATIONS ON DRIFT ACCELERATION AT A SINGLE SHOCK ENCOUNTER

Drift acceleration at a single shock encounter is modified relative to the scatter-free case when magnetic fluctuations are introduced. Figure 15 (Decker and Vlahos, 1985b) shows how a proton's drift encounter at a $\theta_1 = 80°$ shock is altered as the relative r.m.s. amplitude $\delta B/B_0$ ($= \Delta B/B_0$) of magnetic fluctuations upstream and downstream of the shock is increased. The power spectrum used was characteristic of that for transverse,

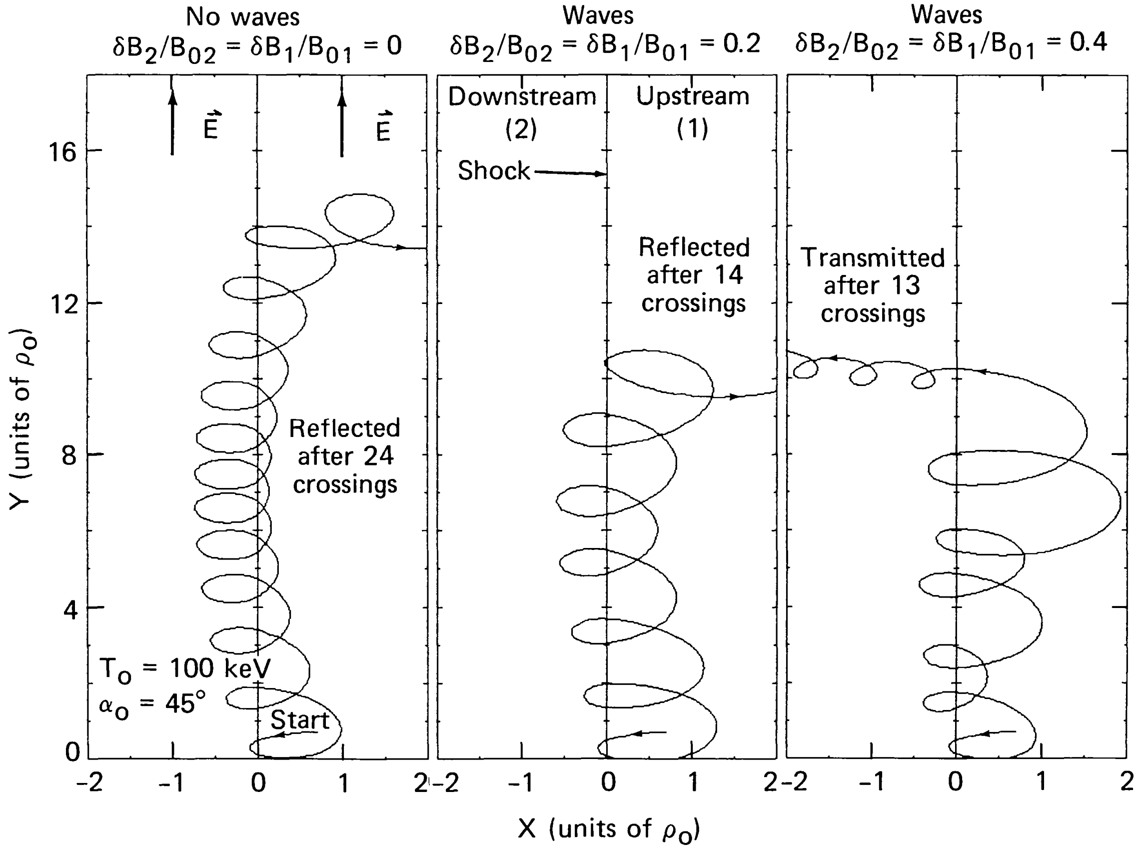

Fig. 15. Projection onto ($x - y$)-plane in shock frame of three proton orbits. Parameters $\delta B_1/B_{01}$ and $\delta B_2/B_{02}$ are relative r.m.s. amplitudes of magnetic fluctuations upstream and downstream, respectively (from Decker and Vlahos, 1985b).

ambient MHD waves in the interplanetary medium near 1 AU, with the upstream and downstream realizations generated independently (i.e., a type I experiment). (Typical orbits from type I and type II experiments are comparable.)

Figure 15 shows the projection onto the $x - y$ plane in shock frame K of protons starting at 100 keV with identical initial conditions in all three panels (here, upstream is $x > 0$, downstream is $x < 0$, ρ_0 = initial gyroradius, $\mathbf{E}$ = electric field). The scatter-free case on the left shows a nicely symmetric drift encounter, with the particle reflected after 24 shock crossings. In the middle panel, the particle is again reflected, but because of wave-induced perturbations during drift, the symmetry is destroyed, and the particle makes fewer crossings, gaining less energy. At the larger fluctuation amplitude on the right, the orbit is highly perturbed, leading to a particle that is ultimately transmitted downstream. The opposite situation can also occur, that is, a particle quickly transmitted or reflected after only a few crossings in the scatter-free limit can perform many more shock crossings and gain much more energy when wave amplitudes are increased.

Figures 16–18 show statistical results for several thousand protons injected isotropically with speed $v_0 = \sqrt{10}\, U_1$ (in frame K_1) upstream of the shock. The wave power spectrum used is the case $\beta = 1$ displayed in the left of Figure 14, and other input parameters are described in Section 4.1; however, we emphasize that the results are representative of the shock acceleration process in general. When magnetic fluctuations are present, a single encounter is defined to end when the particle does not recross the shock surface after three gyroperiods have elapsed.

Figure 16 shows energy versus acceleration time (in units of upstream proton gyroperiod $\tau_1 = 2\pi/\Omega_1$) in shock frame K for 10^4 protons injected at a shock with

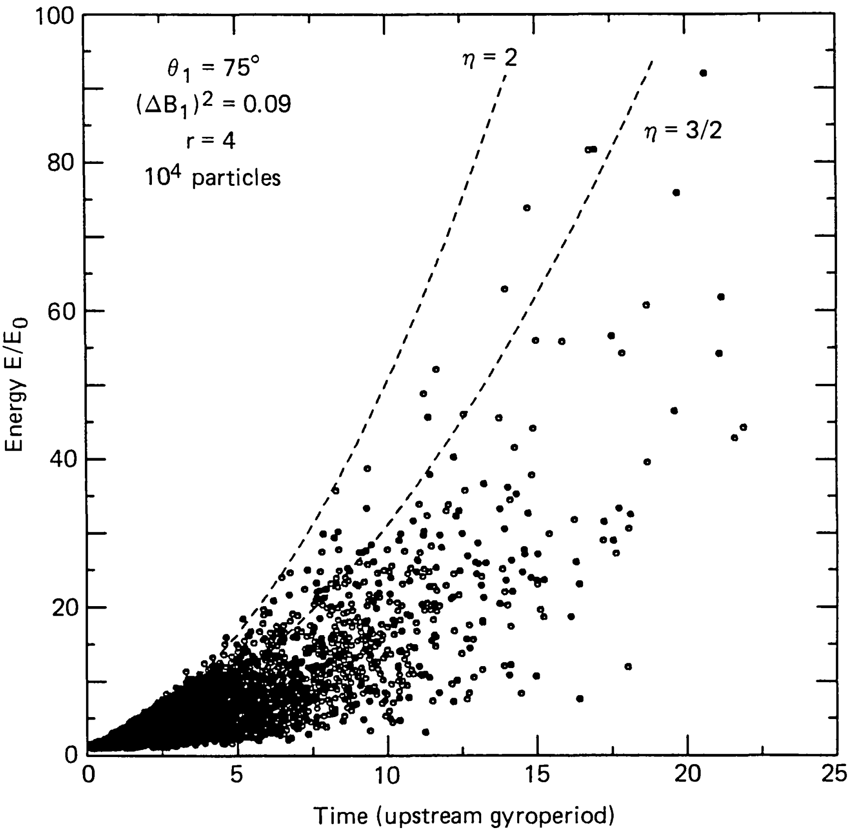

Fig. 16. Energy E/E_0 versus acceleration times for 10^4 protons after single encounter for case $\theta_1 = 75°$, $r = 4$, and $(\Delta B_1/B_{01})^2 = 0.09$. Dashed curves labeled $\eta = \frac{3}{2}$ and 2 correspond to a displacement along electric field ε_0 of $\frac{3}{2}$ and 2 gyroradii per gyroperiod.

$\theta_1 = 75°$, $\delta_1 = 0°$, $M_{A1} = 10$, $\beta_1 = 0.1$ (which yields $r = 3.83$) and $(\Delta B_1)^2/B_{01}^2 = 0.09$. This was a type II experiment using a spectrum of linearly polarized upstream waves with $\mathbf{b}_1(z_1) = \hat{x}_1 b_{1x}(z_1)$; therefore, by Equations (55), $(\Delta B_{2\perp})^2/B_{02}^2 = 0.007$ and $(\Delta B_{2\parallel})^2/B_{02}^2 = 0.006$, so $(\Delta B_2)^2/B_{02}^2 = 0.013$. Compared with the scatter-free case in Figure 6, the addition of magnetic fluctuations increases the peak energy gain from $E/E_0 = 13$ to ~ 90 and the maximum acceleration time from ~ 5 to $\sim 24\tau_1$. To estimate the time dependence of the largest energy gains in Figure 16, we use $\mathrm{d}E = e\boldsymbol{\varepsilon} \cdot \mathrm{d}\mathbf{x} \simeq e\varepsilon_0\, \mathrm{d}y$ (i.e., neglect fluctuations in $\boldsymbol{\varepsilon}$ about ε_0) and assume $\mathrm{d}y = \eta r_{1g}(\mathrm{d}t/\tau_1)$ (i.e., the particle's guiding center is displaced η upstream gyroradii along ε_0 per upstream gyroperiod). For simplicity, we have neglected multiplicative factors that arise from changes in the magnetic field across the shock (see also the derivation in Quenby, 1986). Then, $E/E_0 = [1 + \eta(U_1/v_0)(t/\tau_1)\sin\theta_1]^2 \sim t^2$ for $E \gg E_0$. Figure 16 shows that the largest energy gains lie generally between the two curves corresponding to the extreme case $\eta = 2$ (i.e., a displacement of one gyrodiameter per gyroperiod) and $\eta = \frac{3}{2}$.

Figure 17 contains histograms comparing energy gains (left) and final pitch cosines (right) of the particles in Figure 16 with the corresponding scatter-free results for the

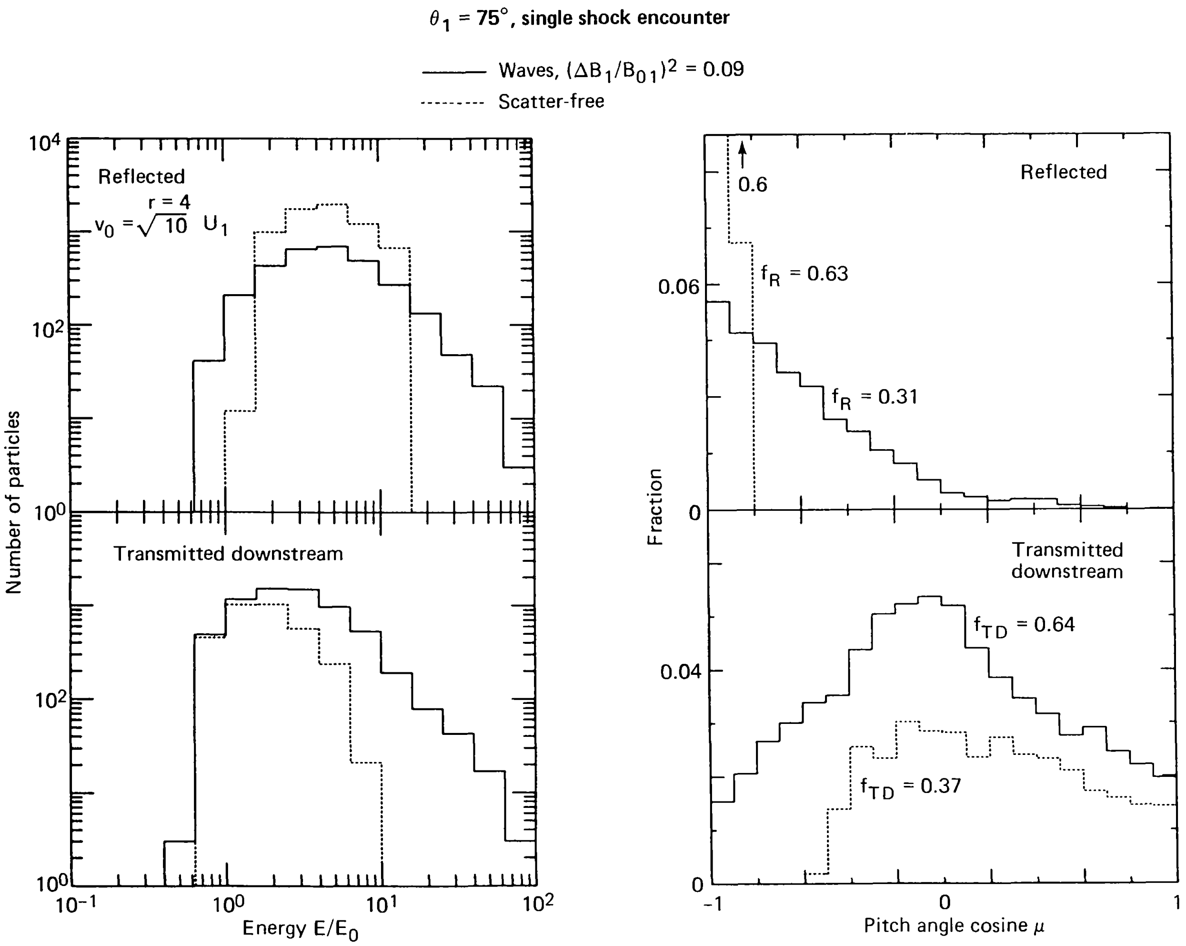

Fig. 17. Histograms comparing energy gains (*left*) and final pitch angle cosines (*right*) after single encounter with $\theta_1 = 75°$ shock. Solid histograms correspond to particles in Figure 16; dashed histograms correspond to scatter-free case in Figures 6 and 7.

$\theta_1 = 75°$ case in Figures 6 and 7, respectively. Note the logarithmic scales for the energy histograms. Energy gains in the scatter-free case cut-off rather abruptly with increasing energy, whereas those produced in the presence of magnetic fluctuations extend smoothly to energies ~ 10 times higher. When plotted as the number ΔN of protons in each energy bin divided by the associated bin width ΔE, the resulting energy spectrum $dN/dE \sim E^{-5/2}$ for $E/E_0 \gtrsim 8$ upstream and downstream. (From diffusive shock acceleration theory, one expects a power law with slope $(2r + 1)/2(r - 1) = 1.53$ for $r = 3.83$ (e.g., Bell, 1978b); however, this is based upon multiple shock encounters under quasi-isotropic conditions, clearly not the case in Figure 17). As shown on the right panel in Figure 17, magnetic fluctuations reduce anisotropies, particularly for the reflected population. Fluctuations also increase the fraction of particles transmitted

1988SSRv...48..195D

downstream, f_{TD}, from 0.37 to 0.64, but at the expense of reflected particles, the fraction of which decreases by a factor of 2 from $f_R = 0.63$ to 0.31.

In summary, as compared with a single encounter in the scatter-free limit, the inclusion of ambient magnetic fluctuations at *quasi-perpendicular* shocks (i) increases particle transmission from upstream to downstream, (ii) produces broader energy distributions for reflected and transmitted particles, with power-law tails extending to several times the maximum energy attained in the scatter-free case, and (iii) reduces anisotropies near the shock, particularly for reflected particles, but does not eliminate them. In addition, the approximate invariance of the magnetic moment for particle encounters with quasi-perpendicular shocks is completely violated in the presence of magnetic fluctuations (Decker and Vlahos, 1985b). All of the aforementioned effects become more pronounced as the amplitude of the random field increases (Decker *et al.*, 1984).

Schatzman (1963) obtained analytic expressions for energy gains at perpendicular shocks (at which all incident particles are ultimately transmitted) and considered the scattering of particles between shock crossings due to the 'clumpiness' of the magnetic field. He found that small-angle scattering in pitch and phase angle produced by such magnetic irregularities provided a statistical process that can produce power-law energy spectra even for a single encounter with a perpendicular shock. Chen (1975) used a computer model to study the effects of scattering between shock crossings for particle encounters with nearly perpendicular shocks. The numerical technique did not involve actual orbit integration in wave fields. Rather, Chen used the crossing-time algorithm and included scattering (elastic in shock frame K) in an *ad hoc* way by introducing random, small-angle changes in a particle's pitch and gyrophase angles between shock crossings. The increased particle transmission, formation of high-energy tails, and reduced pitch angle anisotropies evident in Chen's results are in qualitative agreement with the representative results of orbit integrations displayed in Figures 16 and 17.

Roughly speaking, a broadband spectrum of magnetic fluctuations such as in Figure 14 modifies drift encounters in two ways. First, components of the random field with wavelengths much larger than r_g produce variations in θ_1 about its average value, $\langle \theta_1 \rangle$, that persist over typical drift encounters. Consequently, each particle will 'see' a different θ_1 during a drift encounter. For transverse fluctuations superposed upon a mean field, $\theta_1 - \langle \theta_1 \rangle$ is approximated by a Gaussian distribution with r.m.s. deviation $\Delta B_1/B_{01}$ when $(\Delta B_1)^2/B_{01}^2$ is somewhat less than unity. Due to the nonlinear behavior of the upsteam HT frame speed, $V_1 = U_1 \sec\theta_1$, upon θ_1, the average value of V_1 exceeds $U_1 \sec \langle \theta_1 \rangle$, so, on average, the transmission probability of particles incident on a quasi-perpendicular shock from upstream is increased by fluctuations in θ_1. Second, components of the random field with wavelengths $\sim r_g$ perturb a particle's orbit during a drift encounter (e.g., Figure 15). As is characteristic of acceleration processes that contain a stochastic element, particles in the high energy tail in Figure 17 arise from relatively rare circumstances that provide more and more energy, but to fewer and fewer particles.

Figure 18 shows ensemble-averaged energy gains as a function of fluctuation amplitude $\Delta B_1/B_{01}$ for a *quasi-parallel* shock with $\theta_1 = 15°$ (the case $\Delta B_1/B_{01} = 0$ is in

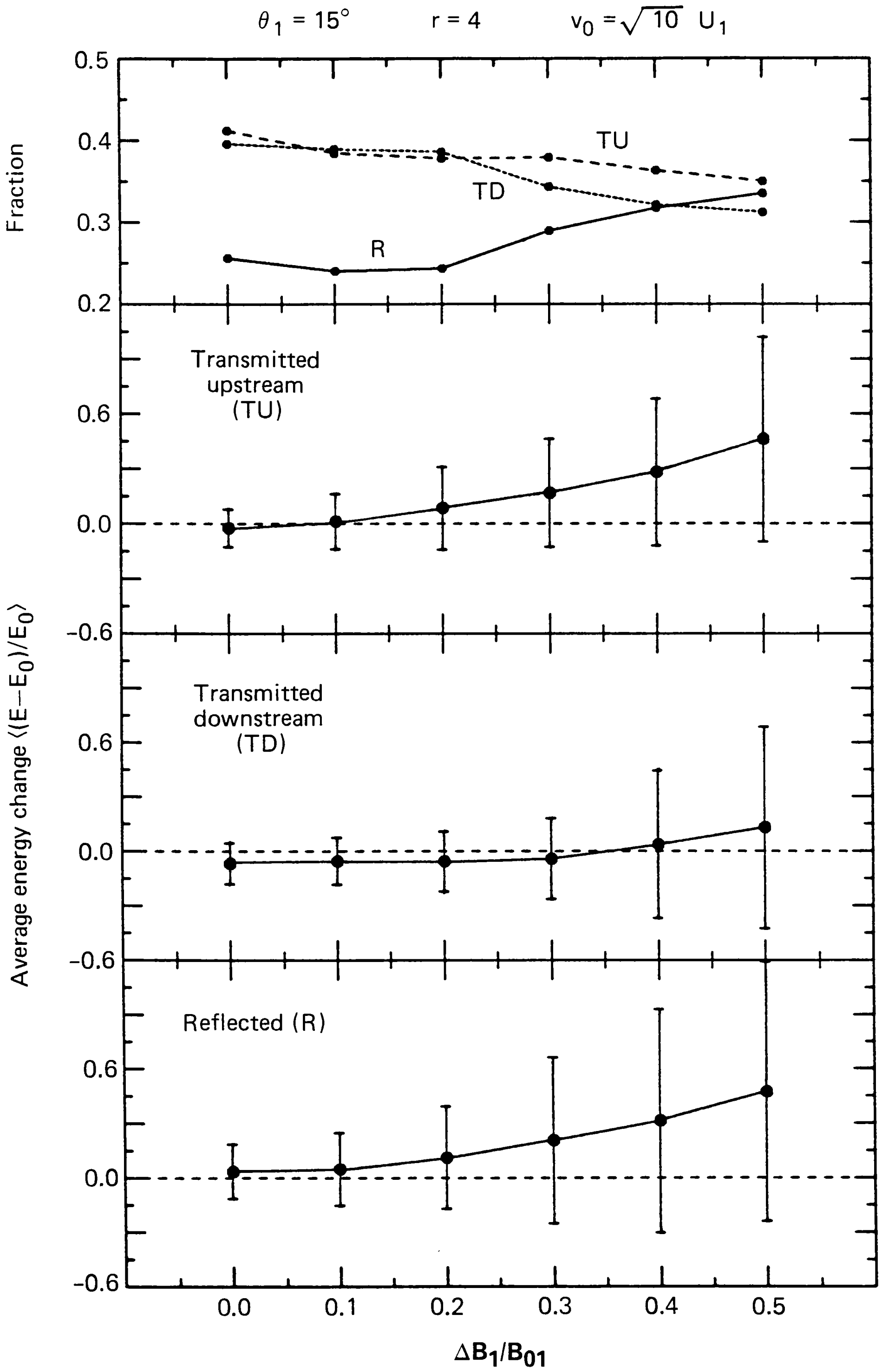

Fig. 18. Energy gains averaged separately over reflected, transmitted downstream, and transmitted upstream particles as a function of r.m.s. amplitude of upstream magnetic fluctuations for quasi-parallel shock $\theta_1 = 15°$. Top panel shows fraction of particles in each category.

Figure 6). On average, particles transmitted downstream (*TD*) continue to show a net deceleration until a relatively high amplitude ($\Delta B_1/B_{01} \gtrsim 0.4$) is reached. By contrast, the net energy gains of reflected (*R*) particles rise monotonically for $\Delta B_1/B_{01} > 0$. This is also true of the distribution transmitted upstream (*TU*) after release of an isotropic, monoenergetic distribution in plasma frame K_2. Also, in contrast to the situation at a quasi-perpendicular shock, the fraction of reflected particles actually increases while that of transmitted downstream particles decreases for $\Delta B_1/B_{01} \gtrsim 0.2$. A grand average formed over the R, TD, and TU distributions gives a net average energy gain that increases monotonically for $\Delta B_1/B_{01} > 0$.

4.3. MODELING OF MULTIPLE SHOCK ENCOUNTERS WITH SPECIFIC APPLICATIONS

If sufficient computer time is available, one can perform computer experiments in which test particles are scattered back to the shock many times, gaining more energy with each traversal of the shock. The two sample orbits in Figure 19 graphically illustrate the basically simple physics of the acceleration process. Shown is the particle's energy E/E_0 (E_0 = 100 keV) versus the x-component of its position in shock frame K (ρ_{01} = upstream gyroperiod = 915 cm in this case). The shock is denoted by the dashed vertical line, with upstream to the left, downstream to the right. The orbits in Figure 19 (adapted from Decker and Vlahos, 1986a) were generated in a type I experiment using the spectrum of magnetic fluctuations in Figure 14, with $\beta = \frac{5}{3}$, $(\Delta B_1)^2/B_{01}^2 = 0.2$ and

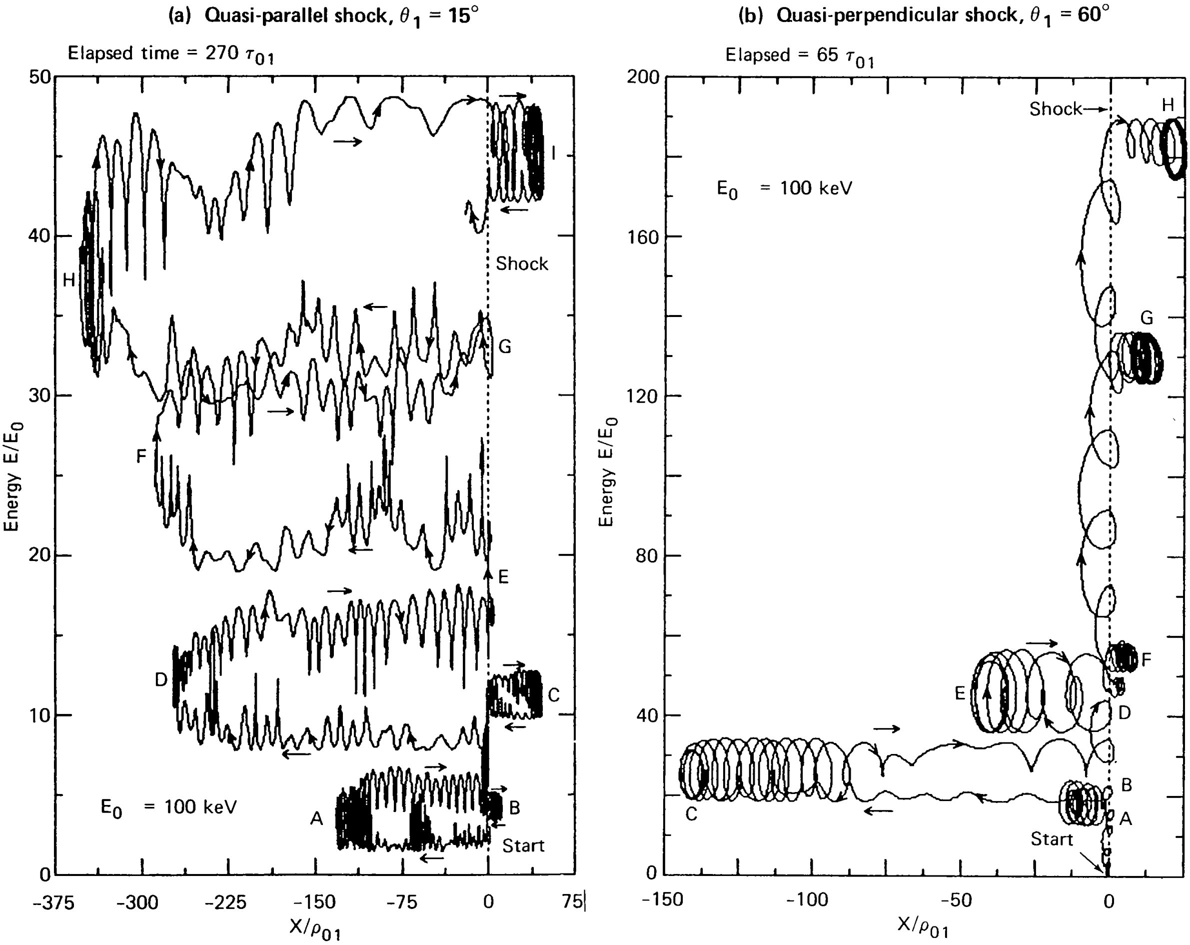

Fig. 19. (a) Sample particle orbit showing multiple shock encounters at a quasi-parallel (θ_1 = 15°) shock. Shown in the energy E/E_0 (E_0 = 100 keV) versus particle's x-coordinate in shock frame K (ρ_{01} = upstream gyroradius at injection). Elapsed time is 270 upstream gyroperiods, τ_{01}. (b) Sample particle orbit at a quasi-perpendicular (θ_1 = 60°) shock. Elapsed time is $65\tau_{01}$ (adapted from Decker and Vlahos, 1986a).

$(\Delta B_2)^2/B_{02}^2 = 0.4$. Other parameters used in this example to model in acceleration at solar flare shocks were given above in the description of Figures 16–18.

For the particle at the quasi-parallel shock in Figure 19(a), energy gains result primarily from the first-order Fermi process. There are four episodes where the particle heads upstream (left-pointing arrows), is eventually scattered in pitch angle until the x-component of it velocity reverses sign (i.e., points marked A, D, F, and H), and returns to the shock (right-pointing arrows). Energy gains result from these upstream excursions because the particle is scattered by magnetic fluctuations essentially frozen into the upstream plasma entering the shock (from the left) at speed U_1. Also clearly evident are three episodes of energy loss as the particle heads downstream and is scattered back towards the shock (i.e., points B, C, *and* I) by magnetic fluctuations moving away from the shock at speed U_2. Because $U_1 > U_2$, energy gained by scattering off approaching upstream fluctuations exceeds that lost by scattering-off receding downstream fluctuations. So, on average, there is a net energy gain over a cycle of motion from upstream to downstream and back again. This is the simple physical process of first-order Fermi acceleration at a shock (e.g., Bell, 1978a). Note, however, that because the shock is oblique, the abbreviated episodes of drift and rapid reflection (see also Figure 3) at the shock (i.e., points E and G) serve to reinject particles directly back upstream, thereby bypassing the downstream energy-loss portion of the cycle. The particle in Figure 19(a) gained a factor ~ 42 in energy after an elapsed time of 270 upstream gyroperiods (τ_{01}).

Figure 19(b) shows a sample orbit at a quasi-perpendicular shock. In this case, energy gains result primarily from the drift process when the particle is within a gyrodiameter of the shock. There are three major episodes of rapid drift acceleration (i.e., start to A, F to G, G to H) and two episodes of first-order Fermi acceleration (i.e., scattering marked by C and E). (The x-component of the particle's position is foreshortened in Figure 19(b) due to the field line obliquity.) This particle gained a factor of ~ 185 in energy after $65\tau_{01}$. As we shall discuss below, with all other parameters the same, acceleration rates increase with increasing θ_1, as suggested by the orbits in Figure 19.

When one examines orbits such as those in Figure 19, it is natural to make a distinction between energy gained during episodes of shock drift and that gained during first-order Fermi cycles. The distinction is physically relevant, especially if one is concerned with acceleration rates, anisotropies, drift displacements along the shock, etc. The distinction is also easier to make if the shock is either nearly parallel or nearly perpendicular. However, it is essential to remember that in the presence of magnetic fluctuations, the two processes are coupled, and simply represent two aspects of the general process of test particle acceleration at a turbulent oblique shock.

Figure 20 summarizes how energy gains are distributed as a function of acceleration time for ensembles of test particles Plotted is the kinetic energy E (in unit of $E_0 = 100$ keV on left axis, in MeV on right axis) versus acceleration time t_a/τ_{01} after a total elapsed time of $500\tau_{01}$ ($= 6.6$ ms for $B_{01} = 50$ G) for each of ~ 2100 protons injected at shocks with $\theta_1 = 0°, 30°, 60°$, and $75°$. Other parameters indicated at the top were the same for each run. The acceleration time is the time of the particle's last shock crossing. Points with $t_a/\tau_{01} < 500$ are particles that spent the time $500 - t_a/\tau_{01}$

propagating without net energy change in the regions upstream or downstream of the shock. Note that the shock compression ratio decreases from 3.85 to 2.75 as θ_1 increases from 0° to 75°.

Figure 20 shows that as θ_1 increases, the acceleration rate increases markedly, but the fraction of particles available for further acceleration decreases. For example, at $\theta_1 = 0°$, most particles are piled up near the cutoff time, and would have undergone further acceleration had the cutoff time been extended. At $\theta_1 = 75°$, there is a dropout of points at lower energies for $t_a/\tau_{01} \gtrsim 60$; thus, the spectrum from 100 keV to $\gtrsim 10$ MeV was essentially completed within a few milliseconds, with all but a few particles left downstream of the shock at the cutoff time. The spectra of the particles in Figure 20 are discussed in detail by Decker and Vlahos (1986a).

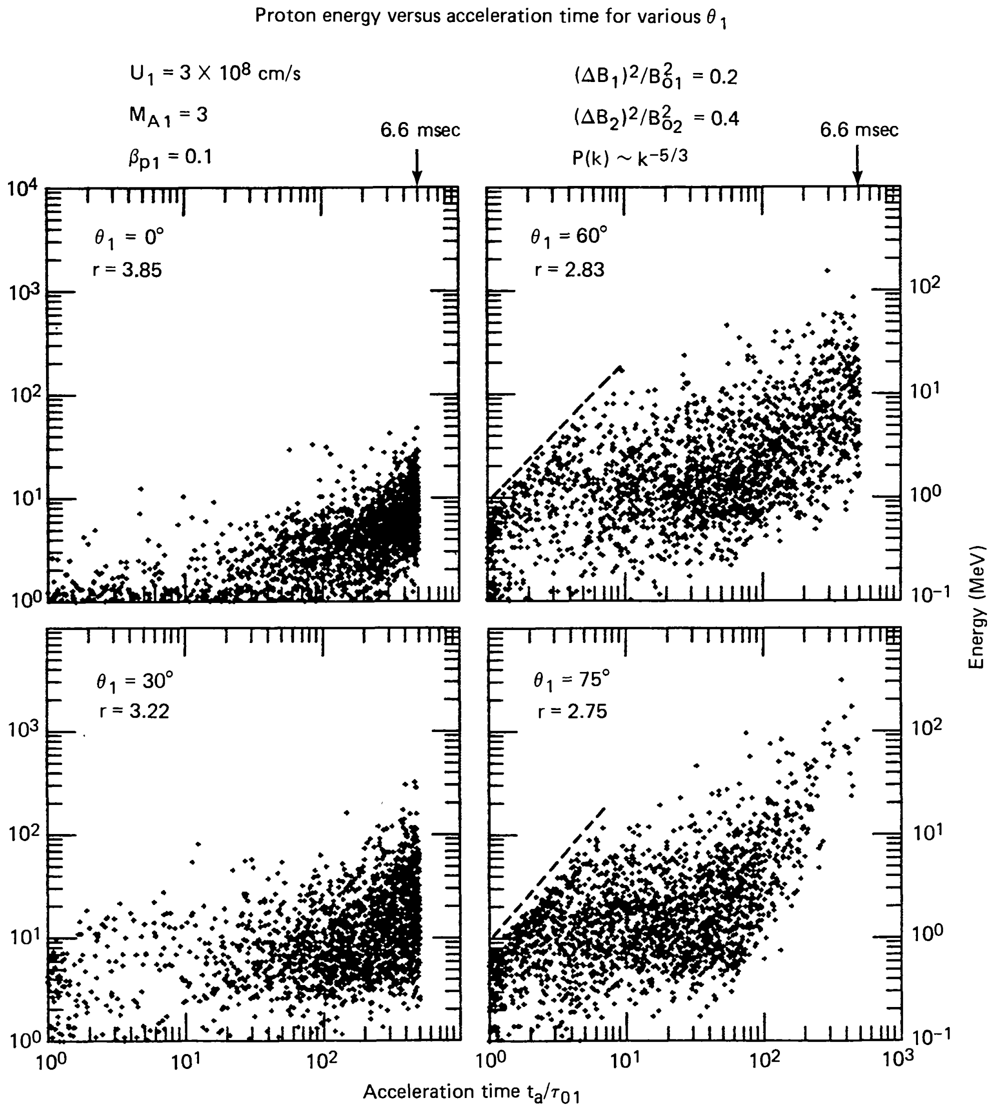

Fig. 20. Energy E/E_0 versus acceleration time t_a/τ_{01} for ~ 2100 protons injected as an isotropic distribution immediately upstream of four shocks with $\theta_1 = 0°, 30°, 60°$, and 75°. Each particle remained in the system for 500 gyroperiods. The acceleration time is the time of the particle's last shock crossing. Parameter r is the shock compression ratio (adapted from Decker and Vlahos, 1986a).

Another interesting feature of Figure 20 is the separate population of particles accelerated from 100 keV to ~10 MeV at the $\theta_1 = 60°$ and 75° shock within only 10 gyroperiods (indicated by the dashed diagonal lines). These are those particles that, through the interplay between scattering and drift, remained at the shock and underwent an intensive period of drift acceleration. We have seen these particles before. They are simply those whose features are displayed in Figures 16 and 17.

The particle distributions in Figure 20 evolved in an environment where fields of transverse magnetic fluctuations extended with unattenuated amplitude an infinite distance upstream and downstream of a flare-generated shock. It was also assumed that the amplitude of the fluctuations was independent of θ_1. Essentially, the assumption was that, once formed, a coronal shock propagates into a turbulent upstream medium that sustains a broadband spectrum of ambient MHD fluctuations of unspecified origin. The assumed sources of the downstream fluctuations included those upstream convected through and amplified by the shock, as well as turbulence excited by the flare release mechanism. However, it is well-known that other possible sources of upstream fluctuations include MHD waves driven by energetic ion beams streaming away from the shock following either reflection from the shock, or leakage from the hot downstream plasma, or both. For example, the excitation of upstream MHD waves from ion beams and the implications for additional ion acceleration have been discussed in relation to the Earth's bow shock (e.g., Gary *et al.*, 1981; Gary, 1985; Sentman *et al.*, 1981; Winske and Leroy, 1984; Bell, 1978a; Eichler, 1981; Lee, 1982; Ellison, 1981) and in relation to interplanetary traveling shocks (e.g., Tsurutani *et al.*, 1983; Kennel *et al.*, 1984; Sanderson *et al.*, 1985). Since such waves are ultimately convected back to and through the shock by the super-Alfvénic upstream flow, the wave amplitude will decrease with increasing distance upstream of the shock (e.g., Hoppe *et al.*, 1981; Tsurutani *et al.*, 1983), so particle scattering will be more efficient closer to the shock. In addition, observations of interplanetary shocks indicate that conditions vary with shock obliquity. In particular, the variance of the upstream shock-associated MHD wave spectrum decreases as θ_1 increases (Russell *et al.*, 1982; Russell and Hoppe, 1983).

In light of the comments in the previous paragraph, it is of interest to examine models that incorporate both a uniform background of ambient magnetic fluctuations and shock-associated upstream waves that are 'damped' in amplitude with increasing distance away from the shock. Figures 21 and 22 (from Decker and Vlahos, 1986b) show input wave power spectra and output particle energy spectra, respectively, from a model to simulate proton acceleration at traveling interplanetary shocks near 1 AU. Figure 21 shows representative upstream wave spectra ($B_0 = B_{01} = 5 \times 10^{-5}$ G), with wavenumber k in the solar wind frame (top and right axes) related to the Doppler-shifted frequency f in the spacecraft frame (bottom and left axes) by $k = 2\pi f / V_{\mathrm{SW}}$ for an assumed solar wind speed of $V_{\mathrm{SW}} = 4 \times 10^7$ cm s^{-1}. Spectrum A represents that of ambient, circularly polarized Alfvénic fluctuations in the interplanetary medium (Hedgecock, 1975; Matthaeus and Goldstein, 1982). The variance of spectrum A is $(\Delta B_{1A})^2 = 0.04 B_{01}^2$, the correlation length is $z_c^A = 2 \times 10^{11}$ cm = 0.013 AU, and $\beta_A = \frac{5}{3}$, so that $P_A(k) \sim k^{-5/3}$ for $k z_c^A \gg 1$.

1988SSRv...48..195D

Figure 21 also shows the spectrum of transverse, circularly polarized MHD waves used to model waves that have been observed in the vicinity of interplanetary shocks at which $\theta_1 \lesssim 65°$ to $75°$ (Tsurutani *et al.*, 1983). The observed power spectrum of such waves typically extends from $\sim 10^{-2}$ to ~ 1 Hz (frequency in the spacecraft frame), decreasing with increasing frequency beyond $\sim 5 \times 10^{-2}$ Hz, with the variance decreasing with distance upstream of the shock. Spectrum *B* represents the shock-associated wave spectrum at the shock ($x = 0$). The correlation length is $z_c^B = 1.3 \times 10^8$ cm (gyroradius of a 2 keV proton), the variance is $(\Delta B_{1B})^2 = 0.25 B_{01}^2$, and $\beta_B = 2$, so that $P_B(k) \sim k^{-2}$ for $k z_c^B \gg 1$. The attenuation of the upstream waves was modeled by damping the magnetic field realization derived from spectrum *B* with the function $\Gamma_1(x) = (1 + |x|/x_1^*)^{-1}$, where $x_1^* = D_1 \cos\theta_1$, and D_1 is the distance from the shock along $\mathbf{B}_{01}$. For example, the variance of spectrum *C* at $|x| = x_1^*$ is $(\Delta B_{1B})^2/4$. This

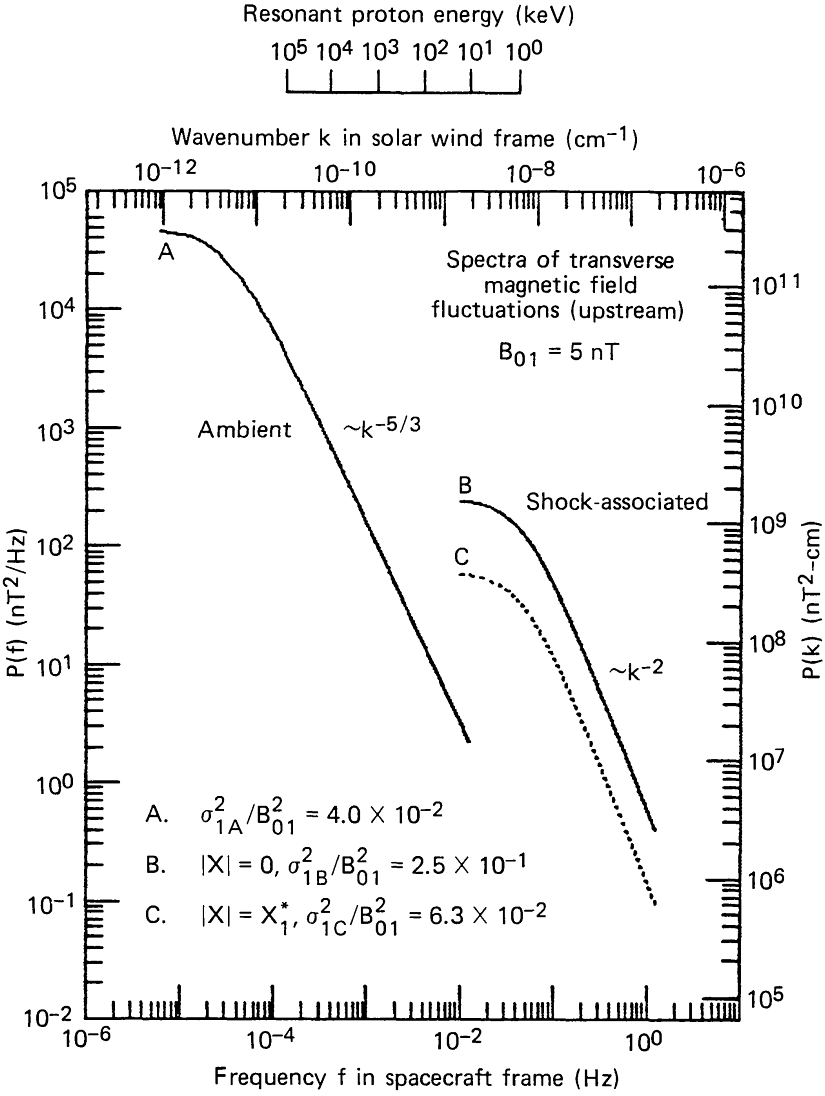

Fig. 21. Power spectra of transverse magnetic fluctuations used to model proton acceleration through multiple shock encounters at an interplanetary shock. Spectrum *A* represents ambient Alfvén waves. Spectra *B* and *C* represent shock-associated transverse MHD waves at the shock, and at one damping length upstream of shock, respectively (from Decker and Vlahos, 1986b).

particular form of Γ_1 provides a good representation of the variance of upstream waves during the 5 April, 1975 event ($\theta_1 = 44°$, shock speed $V_S \simeq 800\ \mathrm{km\ s^{-1}}$) for at least one hour prior to the shock passage (Sanderson *et al.*, 1985) if $D_1 = 1.3 \times 10^{-2}$ AU. However, other functional forms of Γ_1 are easily incorporated into the model. For the runs in Figure 22, $D_1 = 10^{-2}$ AU. Downstream values used were $(\Delta B_{2A})^2 = 0.04 B_{02}^2$ for the ambient spectrum, and $(\Delta B_{2B})^2 = 0.36 B_{02}^2$ and $D_2 = 1$ AU for the shock-associated spectrum (this was a type I experiment).

Figure 22 shows the resultant energy spectra for protons injected at the shock for the two cases $\theta_1 = 0°$ and $60°$ (with all other parameters held fixed) and left in the systems for 300 gyroperiods (~1 hour in the 5γ magnetic field). Other parameters used were $U_1 = 4 \times 10^7\ \mathrm{cm\ s^{-1}}$, $M_{A1} = 8$, $\beta_{p1} = 1$, and $\delta_1 = 0$. The energy spectra extend from 10 keV to ~100 keV for $\theta_1 = 0°$, and from 10 keV to ~1 MeV for $\theta_1 = 60°$. For $\theta_1 = 60°$, the downstream spectrum can be fit with two power laws, with spectral exponents $\gamma = 1.7$ from 10 keV to ~80 keV and $\gamma = 2.6$ from ~80 keV to 800 keV.

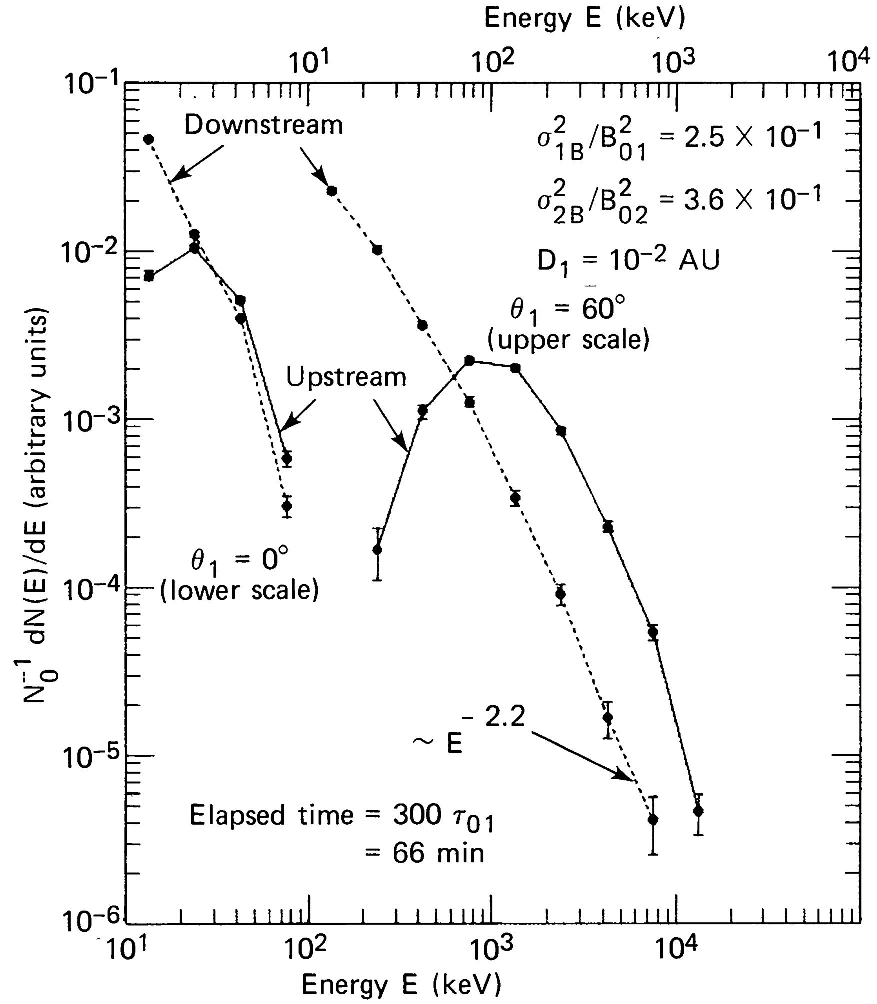

Fig. 22. Energy spectra for $\theta_1 = 0°$ (*lower scale*) and $\theta_1 = 60°$ (*upper scale*) shocks that result after 300 upstream gyroperiods. Power spectra of magnetic fluctuations are shown in Figure 21. Power law fits to downstream spectrum for $\theta_1 = 60°$ yield spectral exponents $\gamma = 1.7$ (10 keV to ~80 keV), $\gamma = 2.6$ (~80 keV to 800 keV), and $\gamma = 2.2$ (10 keV to 800 keV) (from Decker and Vlahos, 1986b).

A fit from 10 keV to 800 keV yields $\gamma = 2.2$. As discussed by Decker and Vlahos (1986b), the model-produced downstream spectra correspond reasonably well with observed values reported by van Nes *et al.* (1984), particularly at higher energies. Results were also presented for cases where the variance and upstream scale length of the shock-associated waves at the 60° shock were reduced relative to the values used at the 0° shock. The downstream spectrum in Figure 22 was not significantly changed when $(\Delta B_{1B})^2$ and $(\Delta B_{2B})^2$ were reduced by factors of 2 and 8, and D_1 was reduced by a factor of 5.

4.4. Drift distances and associated energy gains

As pointed out earlier, the modeling of multiple shock encounters via test particle orbits in synthesized magnetic fluctuations includes acceleration by both the drift and first-order Fermi processes. Although these two processes are intimately coupled through the intermediary of the magnetic fluctuations, it is of interest to calculate the relative contribution of each process to the total energy gain. Aside from its obvious relevance to quantifying the θ_1-dependence of drift exhibited by orbits such as those in Figure 19, this exercise is also relevant to the more practical question of how far particles are displaced along the shock surface by crossfield drifts. Specifically, because each drift encounter displaces a particle's guiding center transverse to the background magnetic field (i.e., in the y-direction in Figure 1(a)), the total displacement accumulated after many drift encounters can drift particles off a shock of finite transverse extent. This will limit the total energy gain and produce an upper cutoff in the energy spectrum (Jokipii, 1982).

Consider a type II experiment (i.e., fields matched across the shock) with the random magnetic field confined to the $x - z$-plane (i.e., $\mathbf{b}_i = \hat{x}_i b_{ix}$ in frame K_i), so that in shock frame K, the total electric field $\boldsymbol{\varepsilon}(\mathbf{x}, t) = \boldsymbol{\varepsilon}_0 + \delta\boldsymbol{\varepsilon}(\mathbf{x}, t)$ is along the y-axis, where $\delta\boldsymbol{\varepsilon}$ is the random component. Using the shock and field parameters from the solar flare acceleration model described in Section 4.1 with the $\beta = \frac{5}{3}$ spectrum in Figure 14, we injected several thousand protons with $E_0 = 1$ MeV, and allowed each particle to remain in the system for from $1000\tau_1$ to $3000\tau_1$ depending upon θ_1 (recall that acceleration rates increase with θ_1), so that at least a few particles reached energy $E/E_0 \sim 10^3$. Parameters θ_1, M_{A1}, and $(\Delta B_1)^2/B_{01}^2$ were varied rom run to run. For each particle, we expressed the total energy gain as the sum of two contributions,

$$\Delta E(\text{total}) = \Delta E(\text{drift}) + \Delta E(\text{Fermi}) \tag{56}$$

and assumed

$$\Delta E(\text{drift}) = e\varepsilon_0 \Delta y = (eU_1 B_{01} \sin\theta_1 / c)\Delta y\,, \tag{57}$$

where we have included the particle's drift distance Δy along the *unperturbed* electric field ε_0 only. For a given computer run, we calculated the ratio $\Delta E(\text{drift})/\Delta E(\text{total})$ for each particle (since both Δy and $\Delta E(\text{total})$ were known) that satisfied $\Delta E(\text{total})/E_0 > 10$, to ensure that particles underwent several encounters.

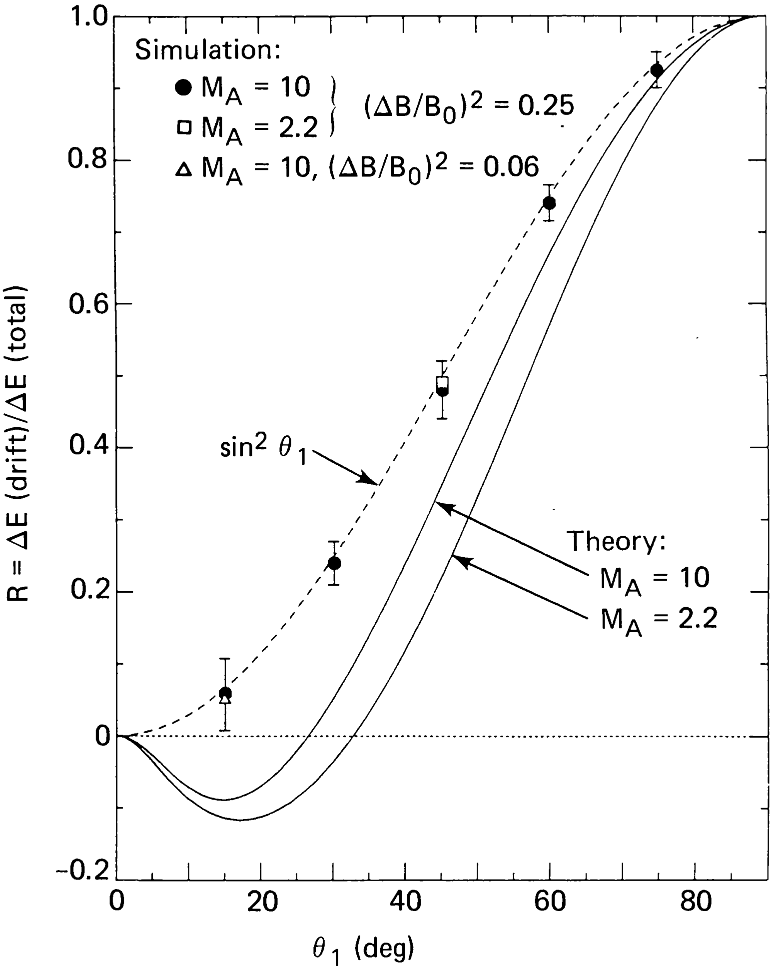

Fig. 23. Plot of R, the ratio ΔE(drift)/ΔE(total) averaged over all particles in given run, versus θ_1 for seven computer runs (points). Solid curves show theoretical predictions for two Mach numbers (from Decker, 1988).

We found that for a given run, i.e., fixed θ_1, the distribution of points in a plot of ΔE(total) versus ΔE(drift)/ΔE(total) exhibited a well-defined average value of ΔE(drift)/ΔE(total) (Decker, 1988). Figure 23 shows the quantity R, the ratio ΔE(drift)/ΔE(total) averaged over the entire distribution of particles from a given run, versus θ_1 for seven computer runs (points). The solid curves follow from Jokipii (1982) who showed that the steady state momentum distribution downstream of a planar shock is of the form

$$f(p, y) \sim p^{-s}\delta[y - y_0 - \eta(E - E_0)] \tag{58}$$

for a source continuously injected at $x = 0$, $y = y_0$, with energy E_0, where $s = 3r/(r - 1)$ is the spectral slope and $\eta = \mathrm{d}y/\mathrm{d}E$ can be written in the form (e.g., Jokipii, 1982; Forman and Webb, 1985)

$$\begin{aligned}\eta &= (e\varepsilon_0)^{-1}\,\frac{(\xi r - 1)\,(r\sin^2\theta_1)\,[(\xi r + 1)\sin^2\theta_1 - 1]}{(r - 1)\,[\cos^2\theta_1 + (\xi r)^2\sin^2\theta_1]}\\ &= (e\varepsilon_0)^{-1}F(r, \theta_1)\,,\end{aligned} \tag{59}$$

where ξ is defined in (12). The δ-function in Equation (58) associates a given energy gain with a unique drift distance Δy. Since $\Delta E(\text{total}) = E - E_0$ and $\Delta y = y - y_0$, it follows that the theoretical value of R is $F(r, \theta_1)$, which is plotted in Figure 23 for $M_{A1} = 2.2$ and 10.

Figure 23 shows that R: (i) remains positive down to $\theta_1 = 15°$ (the smallest angle used in the modeling); (ii) is independent of shock strength r for $2 \leq r \leq 4$ (at $\theta_1 = 45°$, $r = 2$ for $M_{A1} = 2.2$, $r = 4$ for $M_{A1} = 10$); (iii) is insensitive to $(\Delta B_1/B_{01})^2$ for $0.06 \leq (\Delta B_1/B_{01})^2 \leq 0.25$; and (iv) is well-ordered by the single parameter relation $R = \sin^2 \theta_1$. Points (i), (ii), and (iv) do not agree with theoretical predictions based upon solutions to the cosmic-ray transport equation. In particular, there is no evidence that, on average, $\Delta y \sim \Delta E(\text{drift}) < 0$ in the quasi-parallel regime $0 \leq \theta_1 \leq \cot^{-1}(r^{1/2})$.

There are two related reasons for the discrepancy between theory and modeling in Figure 23. First, since drift acceleration is associated with large anisotropies, particularly upstream of the shock, it is not clear that the simultaneous conditions of weak scattering and quasi-isotropy required in the theory actually obtain near the shock. Second, in contrast to existing theory, magnetic fluctuations and their effects upon particle dynamics during drifts are carefully handled in the computer modeling.

It is interesting that drift-associated deceleration implied by the theoretical curves in Figure 23 is consistent with the modeling only at very low levels of magnetic fluctuations (Figures 6 and 8), where anisotropies will be largest (Figure 7). However, as the level of magnetic fluctuations increases, average energy gains increase (left panel of Figure 17, and Figure 18) and anisotropies decrease (right panel of Figure 17). But then drift acceleration deviates from the simple gradient plus curvature drift picture that is evidently valid in the scatter-free limit.

4.5. COMPARISONS BETWEEN COMPUTER MODELING AND DIFFUSIVE SHOCK ACCELERATION THEORY

When performing numerical modeling experiments it is important to make periodic comparisons with the relevant theoretical predictions. This serves at least two purposes. First, agreement between the modeling and theory within the appropriate range of parameters lends confidence to one's model and numerical algorithms. Second, one can look for new phenomena in a systematic manner by performing numerical experiments using parameter values outside the range where the theory is expected to be valid. Modeling efforts involving exact orbit integrations at shocks embedded in synthesized fields of magnetic fluctuations are relatively new, so as yet, systematic parametric studies are unavailable. However, some attempts have been made to compare gross features of the modeling results with theory. We discuss one such attempt below.

The computer-generated energy distributions in Figures 20 and 22 exhibit high-energy limits due to the imposition of an upper cutoff on the acceleration time. Using relations developed in diffusive shock acceleration theory, one can estimate the maximum energy that a distribution of injected test particles is likely to reach after a finite acceleration time at an oblique shock, and compare this estimate with the modeling results. The conditions under which the formalism of diffusive shock acceleration theory is applicable have been enumerated by Axford (1987).

Let Δp and Δt denote, respectively, the mean momentum change and mean time taken per diffusive cycle (where one cycle involves diffusion from upstream to downstream and back again). When, among other conditions, the particle distribution remains quasi-isotropic, one can then show that $\Delta p = (4p/3)(U_1 - U_2)/v$ and $\Delta t = (4/v)(\kappa_1/U_1 + \kappa_2/U_2)$ (e.g., Legage and Cesarsky, 1983; Drury, 1983), so that

$$\frac{\Delta p}{\Delta t} = \frac{U_1 - U_2}{3(\kappa_1/U_1 + \kappa_2/U_2)}\, p\,. \tag{60}$$

Here κ_1 and κ_2 are the elements of the spatial diffusion tensor along the shock normal (i.e., the xx-components) in the upstream and downstream media, respectively. They can be expressed as

$$\kappa(p) = \kappa_{\parallel}(p)\cos^2\theta + \kappa_{\perp}(\mathrm{p})\sin^2\theta\,, \tag{61}$$

where $\kappa_{\parallel}$ and $\kappa_{\perp}$ are the diffusion coefficients parallel and perpendicular to $\mathbf{B}_0$, respectively, and are generally functions of momentum p.

For simplicity, we shall assume here that $(\kappa_{\perp}/\kappa_{\parallel})\tan^2\theta \ll 1$, so that

$$\kappa \simeq \kappa_{\parallel}\cos^2\theta\,. \tag{62}$$

Since we generally expect that $\kappa_{\perp}/\kappa_{\parallel} \ll 1$, Equation (62) essentially restricts us to shocks that are not too near perpendicularity. Indeed, in the regime of nearly perpendicular or perpendicular obliquities, one must retain the second term in (61) to maintain particle diffusion in the x-direction via cross-field scattering. Jokipii (1987, 1988) has examined this regime from the standpoint of diffusive shock acceleration theory, and has emphasized the dramatic increase in acceleration rate as θ_1 approaches 90°. This important prediction should be tested in the future by computer modeling.

To be consistent with the type I numerical experiment described at the outset of this section, we consider the case of particle motion in magnetic fluctuations composed of a spectrum of circularly polarized Alfvén waves with wave vectors aligned with equal probability either parallel or antiparallel to $\mathbf{B}_0$. The appropriate pitch angle diffusion coefficient for an axisymmetric wave distribution as obtained from the quasi-linear theory of pitch angle scattering (e.g., Jokipii, 1971; Lee and Lerche, 1974; Wentzel, 1974) is given by

$$D_{\mu\mu} = \frac{1}{2}\,\frac{\langle(\Delta\mu)^2\rangle}{\Delta t} = \frac{\pi}{4}\,(1 - \mu^2)\Omega_0\,\frac{kP(k)}{B_0^2}\,, \tag{63}$$

where μ is the pitch cosine, $\Omega_0 = qB_0/mc$, and (63) is to be evaluated at wavenumber $k = \Omega_0(v\,|\,\mu\,|)^{-1}$, corresponding to the condition for resonant pitch angle scattering. More sophisticated versions of (63) that account for convection speeds of the waves in the shock frame, correct for the well-known resonance gap at $\mu = 0$, include nonlinear effects and magnetic helicity, etc., are available; however, in keeping with the spirit of our calculation, (63) is adequate. The spatial diffusion coefficient along $\mathbf{B}_0$ is (Earl, 1974)

$$\kappa_{\|} = \frac{v^2}{4} \int_0^1 \mathrm{d}\mu (1 - \mu^2)^2 D_{\mu\mu}^{-1} . \tag{64}$$

At nonrelativistic particle energies of interest here, power for resonant pitch angle scattering lies at wavenumbers for which $kz_c \gg 1$, in which case we can approximate the power spectral density in (52) by

$$P_\beta(k) = A_\beta z_c (\Delta B)^2 (kz_c)^{-\beta} , \tag{65}$$

where

$$A_\beta = \begin{cases} (\beta/\pi) \sin(\pi/\beta) , & 1 < \beta < \infty , \\ 1/\ln[(1 + k_L z_c)/(1 + k_S z_c)] , & \beta = 1 . \end{cases} \tag{66}$$

(Note the comment following Equation (54).) Equations (63)–(65) yield

$$\kappa_{\|} = \tfrac{1}{3} v r_g Q_\beta^{-1} , \tag{67}$$

where

$$Q_\beta = \frac{\pi}{6} A_\beta (2 - \beta)(4 - \beta)(r_g/z_c)^{\beta - 1} (\Delta B/B_0)^2 = r_g/\lambda_{\|} , \tag{68}$$

where $\lambda_{\|}$ is the parallel mean-free path. Then, inserting κ_1 and κ_2 from (62) and (67) into (60), and letting $\Delta p/Dt \to \mathrm{d}p/\mathrm{d}t$, we solve for energy $E_m(t)\,(\ll m_0 c^2)$ at time t starting from initial energy E_0. The result is

$$E_m(t)/E_0 = (1 + \nu t)^{2/(3 - \beta)} , \tag{69}$$

where

$$\begin{aligned} \nu = \frac{\pi^2}{3} & A_\beta (2 - \beta)(3 - \beta)(4 - \beta)(1 - r^{-1}) \times \\ & \times \{1 + (r/a)[\cos^2\theta_1 + (\xi r)^2 \sin^2\theta_1]^{(\beta - 4)/2}\}^{-1} \times \\ & \times (U_1/\Omega_{01} z_c)^{\beta - 1} (U_1/v_0)^{3 - \beta} (\Delta B_1/B_{01})^2 \sec^2\theta_1 \, \tau_{01}^{-1} , \end{aligned} \tag{70}$$

where $a = (\Delta B_2/B_{02})^2/(\Delta B_1/B_{01})^2$. For $\nu t \gg 1$,

$$E_m/E_0 \sim (\Delta B_1/B_{01})^{4/(3 - \beta)} (\sec\theta_1)^{4/(3 - \beta)} t^{2/(3 - \beta)} .$$

It is expected theoretically that after an elapsed time t, the differential in energy number density from E_0 to $\sim E_m$ will be the steady-state form (e.g., Bell, 1978b)

$$\frac{\mathrm{d}n(E)}{\mathrm{d}E} \sim (E + m_0 c^2) [E(E + 2m_0 c^2)]^{-\Gamma} \xrightarrow[E \ll m_0 c^2]{} E^{-\Gamma} , \tag{71}$$

where

$$\Gamma = \frac{2r+1}{2(r-1)}\,, \tag{72}$$

while for $E > E_m$, $\mathrm{d}n/\mathrm{d}E$ will decrease exponentially with energy.

Figure 24 compares the model produced spectra with theoretical predictions for a parallel shock, $\theta_1 = 0°$ (left panel), with $\beta = 1$, and for a quasi-perpendicular shock, $\theta_1 = 60°$ (right panel), with $\beta = 1$ and $\frac{5}{3}$ (Decker, 1987). Plotted is $N_0^{-1}\,\mathrm{d}N(E)/\mathrm{d}E$ (N_0 = total number of particles) versus E/E_0 for protons with $E_0 = 100$ keV. These spectra were generated for each computer run by binning roughly 2500 protons, each of which was left downstream of the shock after undergoing acceleration for a period $500\tau_{01}$. The wave power spectral densities are shown in Figure 14, and other parameters used are shown at the top of Figure 24 and given in the description of Figures 16–18. Also, $(\Delta B_2/B_{02})^2 = 0.4$, i.e., $a = 2$ in Equation (70).

The dashed diagonal lines in Figure 24 are fits to the seven lowest energy points for $\theta_1 = 0°$, and to all points for $\theta_1 = 60°$, $\beta = 1$. The slope of the fit line, Γ_{fit}, should be

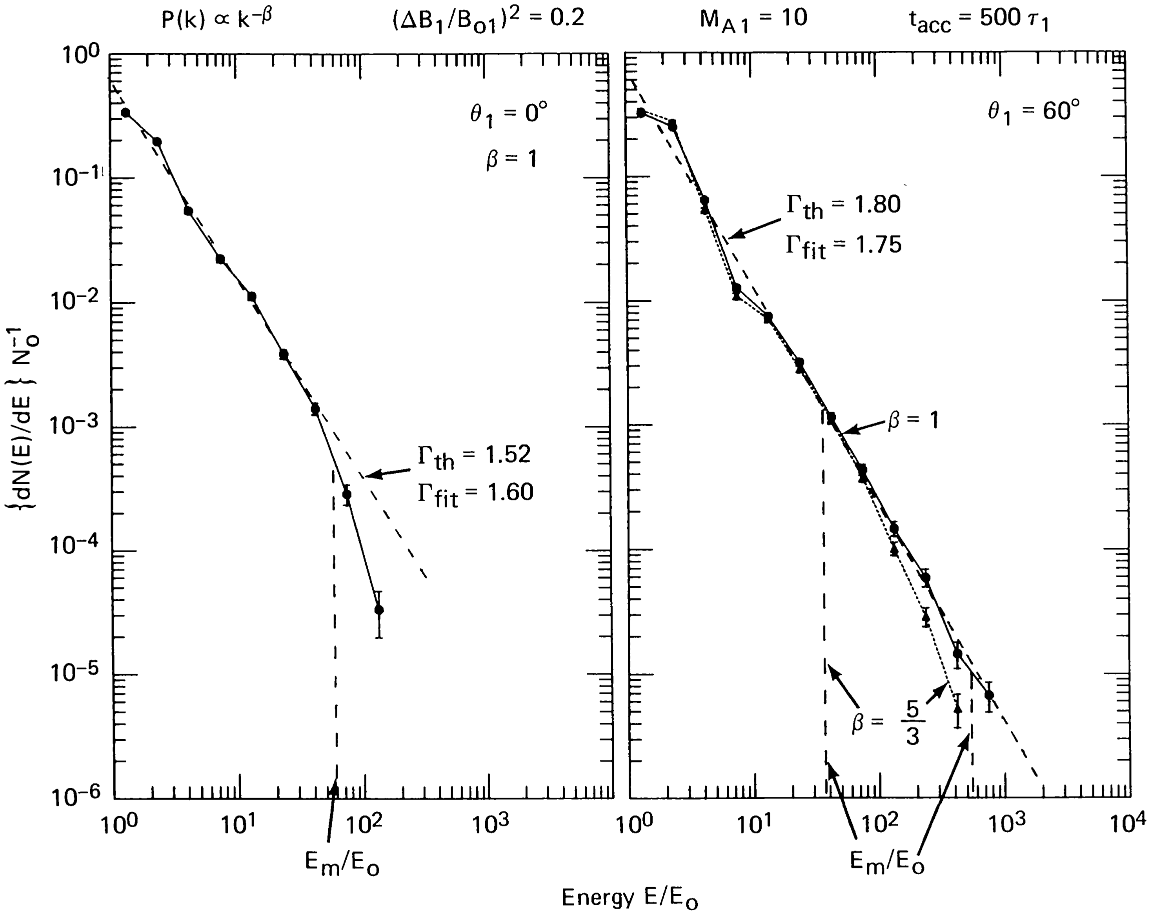

Fig. 24. Energy spectra of downstream protons after acceleration time of 500 gyroperiods. Modeled cases are: $\theta_1 = 0°$, $\beta = 1$ (*left panel*); $\theta_1 = 60°$, $\beta = 1$ and $\frac{5}{3}$ (*right panel*). Spectral slopes from fits to points, Γ_{fit}, and from theory, Γ_{th}, are shown. Dashed vertical lines denote energy E_m/E_0 above which spectrum decreases exponentially (see Equation (69)) (from Decker, 1987).

compared with the theoretical slope, Γ_{th}, given by (72), where $r = 3.89$ for $\theta_1 = 0°$ and $r = 2.85$ for $\theta_1 = 60°$. The spectral slopes Γ_{fit} and Γ_{th} for these examples agree to within 5%. This is consistent with the theoretical expectation that the slope of the steady-state portion of the energy spectra should depend only upon r, not θ_1 (Bell, 1978a). That is, the steady-state spectrum is a power law in energy with a spectral index that is evidently independent of how the relative contributions from the drift and first-order Fermi processes depend upon θ_1 (cf. Figure 23).

The dashed vertical lines in Figure 24 show E_m/E_0 evaluated using (69) and (70). For $\theta_1 = 0°$, the modeled and predicted E_m/E_0 show good agreement. For $\theta_1 = 60°$ and $\beta = \frac{5}{3}$, the predicted break point of $E_m/E_0 \sim 40$ is rather low compared with that of ~ 100–200 for the modeled spectrum. That is, the theory underestimates the acceleration rate in this case. For $\theta_1 = 60°$, $\beta = 1$, poor statistics beyond $E/E_0 \sim 10^3$ makes it difficult to compare with the predicted E_m/E_0, although the continuation of the power law to the last significant modeled point again suggests that theory underestimates the acceleration rate. The reason for this is apparently due to the relatively low injection energy of 100 keV, in which case $U_1 \sec\theta_1/v_0 = 1.5$, and the early stages of acceleration proceed faster than theory can reliably predict (note the structure in the $\theta_1 = 60°$ spectra from E_0 to $\sim 10E_0$). It is found that at higher injection energies for which $(U_1 \sec\theta_1/v_0)^2 < 1$ and the theory is expected to be valid, the modeled and predicted E_m/E_0 for $\theta_1 = 60°$ are in better agreement.

Although encouraging, the comparison between theory and modeling in Figure 24 is incomplete and rather crude. More detailed and definitive tests are possible. For example, the spectra from the modeling represent a spatial integration over the entire downstream half-space at a particular time. By performing appropriate integrations on theoretical expressions for the spatial, temporal, and energy dependence of the particle distribution function, one could compare the modeled and theoretical spectra directly, both upstream and downstream of the shock.

It is also necessary to cover a large range of θ_1 with the modeling. Figure 24 shows that, with all other parameters fixed, the acceleration rate increases with increasing θ_1. However, $\theta_1 = 60°$ is a modest value, with the peak energy reached only ~ 10 that for $\theta_1 = 0°$. As noted earlier, Jokipii (1987) has predicted that the acceleration rate can rise sharply as θ_1 approaches 90°, where the peak energy reached after a given time can be several orders of magnitude higher than at a parallel shock. This prediction, which has important consequences for shock acceleration in many astrophysical settings, has not been tested with computer models.

5. Selected Results from Plasma Simulations

Thus far in this review we have concerned ourselves with test particle acceleration under conditions where the shock was treated as a planar discontinuity and the fields upstream and downstream were either static and uniform, or else possessed an additional fluctuating component constructed from a spectrum of plane waves. The first case led to scatter-free drift acceleration at a single shock encounter (Section 3). The second case led to multiple shock encounters and acceleration through the drift and first-order Fermi processes (Section 4). These cases are the main topics of this review. However, we do not wish to imply that we have covered all the important physical processes. For example, the assumption that $r_g \gg L_s$ eliminated effects associated with the shock structure, such as how ions extracted from the thermal pool are accelerated to superthermal, and perhaps higher, energies in the shock transition. Such effects must be investigated using numerical simulations that incorporate the self-consistent coupling between the plasma particles and the electromagnetic fields.

We do not intend to review numerical simulations pertaining to oblique shock structure and associated particle phenomena. This would be beyond the scope of this review and outside the author's area of expertise. Excellent reviews can be found in the proceedings of various conferences, such as those from the Napa Chapman Conference on Collisionless Shocks in the Heliosphere (*Geophysical Monographs* 34 and 35, 1985), the Second International School for Space Simulations (*Space Sci. Rev.* **42**, 1985), and the International Conference on Collisionless Shocks held in Balatonfüred, Hungary, in the summer of 1987. For our purposes we have simply selected a few examples that illustrate the capability of the simulations and the potential importance of processes that we have overlooked in the present review.

5.1. SHOCK DRIFT ACCELERATION AT LOW ENERGIES

It is of considerable interest, particularly with regard to ion injection processes at oblique shocks, to examine drift acceleration at shocks of finite thickness, i.e., when $r_g \lesssim L_s$. Simulations of supercritical perpendicular and quasi-perpendicular shocks have indicated shock transitions (i.e., magnetic field foot plus ramp plus overshoot) with scales of a few ion inertial lengths, c/ω_{pi} (e.g., Leroy *et al.*, 1982; Leroy and Winske, 1983). This is consistent with observations of relatively high Alfvén Mach number, quasi-perpendicular shocks near 1 AU, such as the Earth's bow-shock (e.g., Russell and Greenstadt, 1979) and some interplanetary shocks (e.g., Dryer *et al.*, 1975). For such cases, Decker and Vlahos (1985b) have argued that the assumption $r_g \gg L_s$ is likely to break down for proton energy $\lesssim 10$ keV.

Figure 25 is from an investigation by Burgess (1987b) in which mildly energetic (1–10 keV) protons were released upstream of quasi-perpendicular shocks. The shocks were generated using a 1-D hybrid simulation code (e.g., Leroy *et al.*, 1982; Winske, 1985), which treats ions as particles and electrons as a massless fluid. This code creates shocks with realistic internal electromagnetic structure that is variable in space and time. The solid histograms in Figure 25 were obtained by injecting an isotropic, monoenergetic population of 2000, 2 keV protons upstream of a shock with $\theta_1 = 70°$, $M_{A1} = 6.5$, and $\beta_{p1} = 1.0$. These protons were treated as test particles in the dynamic shock fields. For this case, $v_0 = 2.4 U_1$ and the total elapsed time was $60 \Omega_1^{-1}$. A comparison of the distributions in Figure 25 with those in Figures 6 and 7 shows that the characteristic signatures of drift acceleration are clearly evident after particle interactions with realistic shock models for injection energies that, in solar wind terms, are normally termed 'superthermal'.

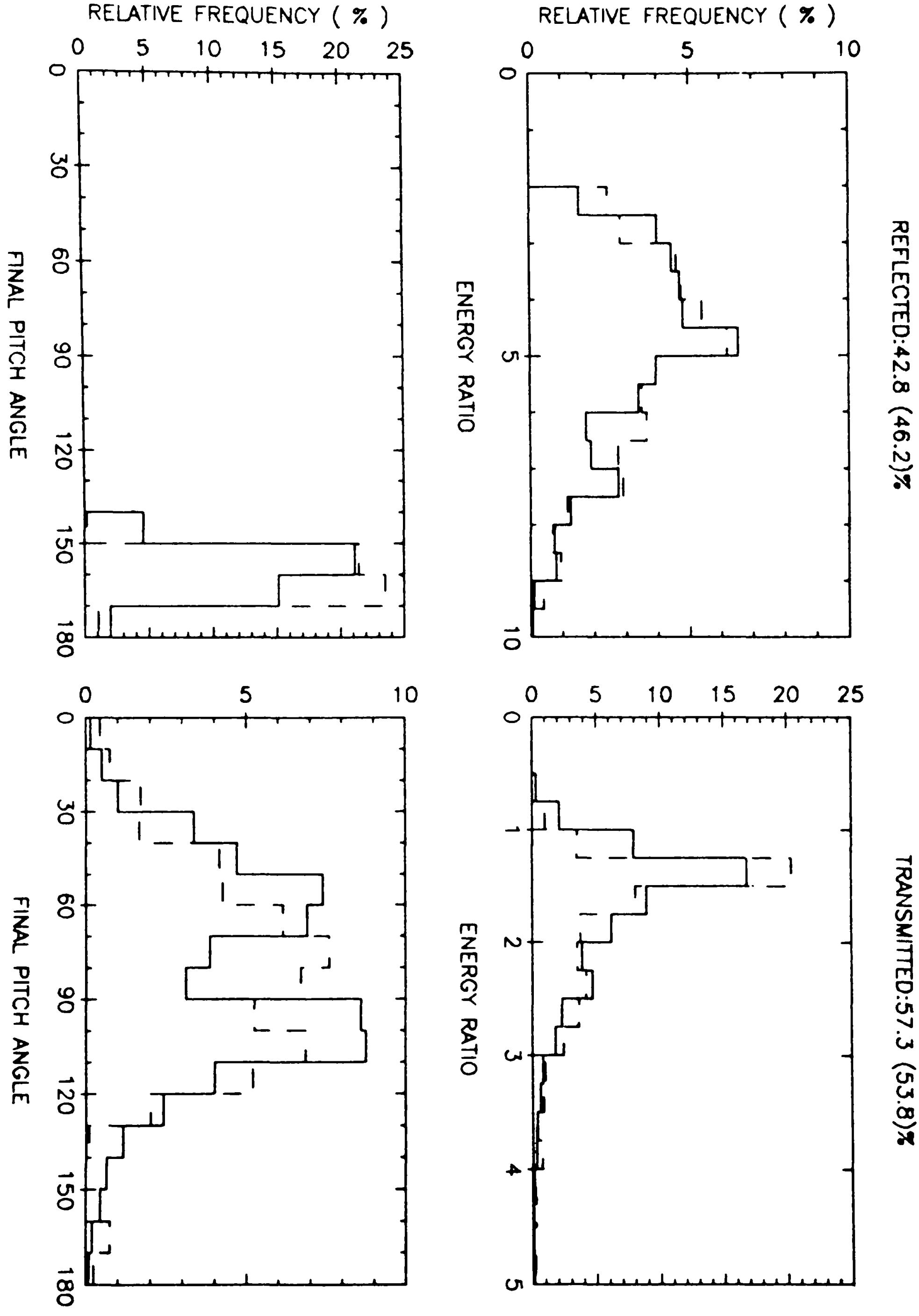

Fig. 25. Energy and pitch angle histograms in study of drift acceleration at low energies. Case shown is for $\theta_1 = 70°$, $M_{A1} = 6.5$, and initial proton speed $v_0 = 2.4U_1$ (energy of 2 keV). Solid histograms result after $60\Omega_p^{-1}$ using 1-D hybrid simulation code (Ω_p = proton gyrofrequency). Dashed histograms are from model where uniform and static upstream and downstream fields were connected by smooth shock transition of width $L_s^* \sim r_{g0}/5$ (from Burgess, 1987b).

Based upon his findings, as well as results from previous studies by Leroy and Winske (1983) and Burgess (1987a), Burgess (1987b) proposed the following scenario for the θ_1-dependence of injection in the quasi-perpendicular regime. For $\theta_1 \sim 30°$ to $60°$, depending upon M_{A1}, drift acceleration can operate directly on the *thermal* population, producing upstream field-aligned beams of reflected protons of 1–20 keV. For $\theta_1 \gtrsim 60°$, there is a minimum injection energy in the mildly energetic (superthermal) range above which drift acceleration and reflection can occur. This minimum energy increases as θ_1 increases towards 90°. Consequently, at naturally occurring shocks where θ_1 will fluctuate over a range of values (see, e.g., Figure 14(b) and Greenstadt and Mellott, 1985), the drift process will not only accelerate incident energetic ions, but will also accelerate ions in the thermal core and reflect them upstream where they are available for further acceleration.

Although realistic, hybrid code calculations are expensive and limited to relatively short run times and spatial dimensions. The dashed histograms in Figure 25 were obtained using a simple model in which uniform and static upstream and downstream fields were connected by a smooth transition of width L_s^*. In this case, $r_{g0} \sim 5L_s^*$. On a statistical basis, the smooth shock model does an adequate job of reproducing the hybrid code distributions. This suggests a simple way to introduce the effects of finite shock thickness to deal with the problem of low injection energies in orbit-integration modeling of acceleration at oblique shocks.

5.2. $\mathbf{V}_p \times \mathbf{B}$ ACCELERATION

The importance of the internal electromagnetic structure of nearly perpendicular fast-mode shocks with regard to ion acceleration is underscored by a series of recent papers emphasizing the '$\mathbf{V}_p \times \mathbf{B}$' acceleration process (e.g., Ohsawa, 1986a, b; Ohsawa, 1987; Ohsawa and Sakai, 1987; Sakai and Ohsawa, 1987, and references therein). Here, $\mathbf{V}_p$ denotes the wave or disturbance phase velocity. For a shock, $\mathbf{V}_p$ is just the shock velocity relative to the upstream plasma.

The key ingredient in $\mathbf{V}_p \times \mathbf{B}$ acceleration is the cross-shock, charge-separation electric field E_x oriented parallel to the shock normal. The basic physical argument is as follows (e.g., Sakai and Ohsawa, 1987). From nonlinear wave theory based upon the two-fluid cold plasma equations, it is found that a large potential jump $e\phi \sim 2m_i v_{\mathrm{A}}^2(M_{\mathrm{A}} - 1)$ develops across a laminar shock (m_i = ion mass, v_{A} = Alfvén speed, $M_{\mathrm{A}} = V_p/v_{\mathrm{A}}$ = Alfvén Mach number). For $\theta_c \lesssim \theta_1 \leq 90°$, this potential jump occurs over the shock ramp of width $\Delta \sim (c/\omega_{pe})/[2(M_{\mathrm{A}} - 1)^{1/2}]$, where c/ω_{pe} is the electron inertial length, ω_{pe} is the electron plasma frequency, and the critical angle $\theta_c = \tan^{-1}[(m_i/m_e)^{1/2} - (m_e/m_i)^{1/2}] \simeq 88.7°$ for a proton plasma. Thus, the cross-shock electric field is given by $eE_x \sim e\phi/\Delta \sim m_i v_{\mathrm{A}}^2 (c/\omega_{pe})^{-1} (M_{\mathrm{A}} - 1)^{3/2}$.

Now, some fraction of the incident thermal ions become trapped in the shock transition layer, and are pushed along with the shock by the electric field E_x. However, due to the Lorentz force associated with $\mathbf{B}$ (lying in the $x - z$-plane), the increase in an ion's velocity component v_x is continuously converted to component v_y; thus, such resonant ions can maintain $v_x \sim V_p$ and interact with E_x for a time much longer than a gyroperiod. Trapping ceases when ions are accelerated to the $\mathbf{E} \times \mathbf{B}$ drift speed $v_m \sim cE_x/B$. Therefore, ions are accelerated in a direction perpendicular to $\mathbf{B}$ and parallel to the shock surface up to a maximum speed

$$v_m \sim v_{\mathrm{A}}(m_i/m_e)^{1/2} (M_{\mathrm{A}} - 1)^{3/2} \qquad (73)$$

by a resonant wave-particle interaction within the shock layer. One can also estimate the associated trapping time by (Sakai and Ohsawa, 1987)

$$t_a \sim \Omega_i^{-1}(m_i/m_e)^{1/2}(M_A - 1)^{3/2}/M_A \tag{74}$$

and the distance traversed in the y-direction along the shock front by

$$L_f \sim \tfrac{1}{2}(c/\omega_{pi})(m_i/m_e)(M_A - 1)^3/M_A\,, \tag{75}$$

where c/ω_{pi} is the ion inertial length, and ω_{pi} is the ion plasma frequency. Thus, trapped thermal ions can be resonantly accelerated to a relatively high energy is a short time and small displacement along the shock surface.

As θ_1 decreases from θ_c, Δ increases from $O(c/\omega_{pe})$ to $O(c/\omega_{pi})$. The potential jump ϕ is only weakly dependent upon θ_1. Consequently, the cross-shock electric field and, therefore, v_m are $\sim (m_e/m_i)^{1/2}$ time smaller for $0 \leq \theta_1 < \theta_c$ than for $\theta_c \lesssim \theta_1 \leq 90°$. Thus, $v_m \sim v_A(M_A - 1)^{3/2}$ for $\tan\theta_1 = O(1)$. The strong acceleration to speeds in (73) occurs only when the shock is perpendicular or very nearly so. Inclusion of finite plasma beta effects (i.e., nonzero ion and electron temperatures) can decrease θ_c by a degree or so, thereby broadening the strong acceleration regime of θ_1, and increase the acceleration in this regime (Ohsawa, 1986b).

The predictions for $\mathbf{V}_p \times \mathbf{B}$ acceleration outlined above have been confirmed by $2\frac{1}{2}$-D, fully relativistic, fully electromagnetic particle simulations that retain full ion and electron dynamics (Ohsawa, 1986a). Figure 26 shows ion phase space plots of p_x/m_i (left) and p_y/m_i (right) versus x at time $\omega_{pe}t = 800$ in one such simulation to study $\mathbf{V}_p \times \mathbf{B}$ acceleration of protons at nearly perpendicular shocks in the lower solar corona (Ohsawa and Sakai, 1987). All lengths, times,and velocities are in units of the grid

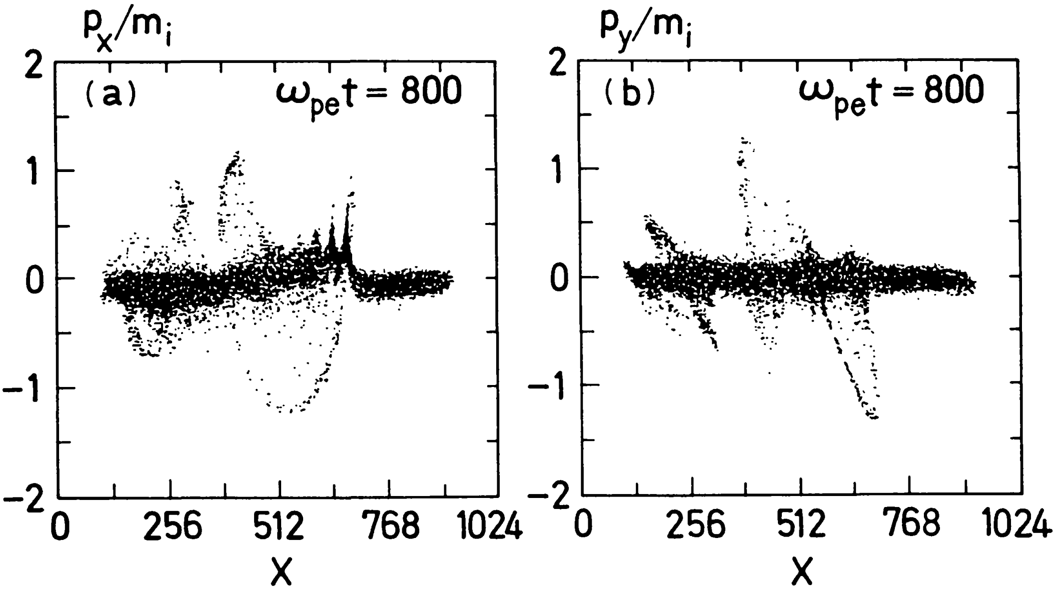

Fig. 26. Sample of ion phase space from $2\frac{1}{2}$-D numerical simulation incorporating full election and ion dynamics. Shown are ion phase space plots of momentum components p_x/m_i and p_y/m_i versus x at time $\omega_{pe}t = 800$, where x is in units of the grid spacing and ω_{pe} = ion inertial length. Plots illustrate $\mathbf{V}_p \times \mathbf{B}$ acceleration at the nearly-perpendicular shock ($\theta_1 = 88.7°$) at $x \simeq 680$ (from Ohsawa and Sakai, 1987).

spacing Δ_g, the inverse electron plasma frequency ω_{pe}^{-1}, and $\omega_{pe}\Delta_g$, respectively. For this run, $M_A = 1.57$, $\theta_1 = \theta_c \simeq 88.7°$ ($\beta_p = 0.07$), $v_A = 0.4$, $c/\omega_{pe} = 4$ (i.e., $c = 4$), and $m_i/m_e = 100$. It was determined from the simulation that $\Delta \simeq 30 \simeq 7.5c/\omega_{pe}$, $\phi \simeq 20 \simeq 80T_i$ (T_i = initial ion temperature), so $E_x \simeq 0.7$. The plot of $p_x/m_i \simeq v_x$ shows some ions that are trapped by the large potential at the shock front at $x = 680$ and pushed along at speed $v_x \sim V_p$, $V_p = M_A v_A \simeq 0.6$. The plot of $p_y/m_i \simeq v_y$ shows that these trapped ions are $\mathbf{V}_p \times \mathbf{B}$ accelerated along the shock front in the y-direction to speed $v_y \simeq 1.4$. From the simulation, $v_m \sim cE_x/B \sim 0.7$, while from the estimate in (73), $v_m \sim 1.7$. After acceleration to $\sim v_m$, the ions become detrapped and are deposited downstream.

Ohsawa (1987) has proposed $\mathbf{V}_p \times \mathbf{B}$ acceleration to explain the intense particle acceleration detected by the LECP instrument on Voyager 2 (1.9 AU) in coincidence with the passage of a quasi-perpendicular interplanetary shock on 6 January, 1978. This shock-spike event was associated with the highest ion and electron energies yet observed at a single shock. Ion intensity increases were detected from $\sim$ 17 keV to at least 22 MeV for protons, to at least 88 MeV for α-particles, to $\sim$ 220 MeV for oxygen, and to more than 112 MeV for iron. Using the observed shock parameters ($M_A = 3.4$, $V_p = 200$ km s^{-1}, $\theta_1 = 87.5°$, $B = 5 \times 10^{-5}$ G), and the finite beta expressions for v_m, Ohsawa (1987) estimated $v_m \sim$ 1 MeV for protons, which is at least an order of magnitude smaller than the observed value. The authors argued how neglected effects could increase the estimate of v_m, but no quantitative calculations were presented. They also note that since $v_m \sim cE_x/B$ is independent of ion mass, the kinetic energy of accelerated ions should be proportional to mass, which is consistent with the highest energy α-particle energy ($\sim$ 88 MeV) being four times that of the highest proton energy ($\sim$ 22 MeV).

An alternate interpretation of the 6 January, 1978 event in terms of drift acceleration was proposed by Sarris and Krimigis (1985) and Decker (1987). Acceleration from thermal energies is not necessary, since the enhanced background of solar particles from a previous solar flare provided an ample source of energetic particles available for drift acceleration. The species dependence of peak energy gains noted above is also consistent with the drift process (e.g., Section 3.7), as is the energy-dependence of features in the energy spectra upstream and downstream of the shock (Decker, 1987).

Clearly, detailed quantitative comparisons between the spacecraft data and predictions from both the drift acceleration modeling and the $\mathbf{V}_p \times \mathbf{B}$ acceleration simulations need to be performed if any headway is to be made. Specifically, what are the predicted energy and angular distributions of the accelerated ions and how do these distributions evolve from upstream to downstream through the shock? (Unfortunately, angular information is unavailable for the event reported by Sarris and Krimigis (1985). However, such information is available for other events where $\theta_1 \lesssim 90°$, e.g., the 25 December, 1978 event with $\theta_1 = 88°$ in Figure 12.) Since both the drift and $\mathbf{V}_p \times \mathbf{B}$ acceleration processes are probably operative at naturally occurring shocks, it may be difficult to clearly discern features of either process separately, particularly in observations made downstream of the shock.

5.3. Colliding quasi-perpendicular shocks

The third example in our small sample of numerical simulations involves the interaction of two collisionless shocks. Cargill and Goodrich (1987) employed a 1-D hybrid simulation code to investigate effects produced when two fast-mode, quasi-perpendicular shocks collide head-on. One of their goals was to study the differences when the shocks were both either subcritical or supercritical. Basically, MHD theory predicts the existence of a critical fast magnetoacoustic Mach number, M_F^*, above which anomalous resistivity alone is insufficient to provide the dissipation necessary for a shock to satisfy the RH conservation equations.

The set of upstream parameters associated with M_F^* correspond to the downstream condition $U_{2x} = v_{2S}$, where U_{2x} is the normal component of downstream flow and v_{2S} is the downstream sound speed. For typical solar wind parameters, $M_F^* \sim 1$–2 (Edmiston and Kennel, 1984). Shocks at which $M_F = U_1/c_{1F}$ (c_{1F} is defined in Equation (15)) satisfies $M_F < M_F^*$ are called subcritical, while those with $M_F \geq M_F^*$ are called supercritical. Ion kinetic effects in the form of ions specularly reflected from the shock produce an effective viscosity that is evidently sufficient to provide the additional dissipation to fulfill the RH conditions, at least for supercritical quasi-perpendicular shocks. That is, for $45° \lesssim \theta_1 \leq 90°$, the guiding centers of reflected ions are directed downstream, so most of these ions must return to the shock and penetrate downstream, thereby contributing to downstream thermalization. However, for $0° \leq \theta_1 \lesssim 45°$, the guiding centers of reflected ions are directed upstream, so most of these ions freely escape upstream, and so do not contribute to thermalization at quasi-parallel shocks.

Here we shall concentrate on the aspect of ion acceleration at supercritical shocks discussed by Cargill and Goodrich (1987). Figure 27 shows ion energy spectra at five times during a run ($t = 0, 3.68, 6.84, 8.64$, and $10.44\Omega_i^{-1}$ for (a)–(e)) where two identical shocks for which $\theta_1 = 45°$, $\beta_i = \beta_e = 1$, and $M_{A1} = 8$ propagate along the x-axis. At time $t = 0$, the right-moving shock is at $x = 40$ (units of c/ω_{pi}) and the left-moving shock is at $x = 120$. In Figure 27, n (normalized to the total number of initial simulation particles n_0) is the number of ions in $80 \leq x \leq 120$; thus, the full distributions result by multiplying those in Figure 27 by a factor of two. Ion energy E is normalized to $E_0 = m_i U_1^2/2$, the initial ram kinetic energy of the incident plasma as measured in the shock frame.

At $t = 0$ in Figure 27, most ions have $E/E_0 \leq 1$, since the plasma in the region between the converging shocks is initially stationary. However, there is a small population centered on $E/E_0 \sim 5$–6 that are those ions streaming toward the left after having been singly-reflected (as described above) from the left-moving shock. At $t = 3.68\Omega_i^{-1}$, some of these ions have encountered the right-moving shock and have been energized further to $E/E_0 \sim 10$ by drift acceleration. By $t = 6.84\Omega_i^{-1}$, the shocks have collided, and some ions have been further accelerated at the collision point. At $t = 8.64\Omega_i^{-1}$, the shocks start to propagate away from the collision point and out of the simulation box, accelerating ions out to $E/E_0 \sim 20$.

Cargill and Goodrich (1987) also studied collisions of $M_A = 8$ shocks for the two cases where both shocks had $\theta_1 = 60°$ or both had $\theta_1 = 90°$. At comparable times

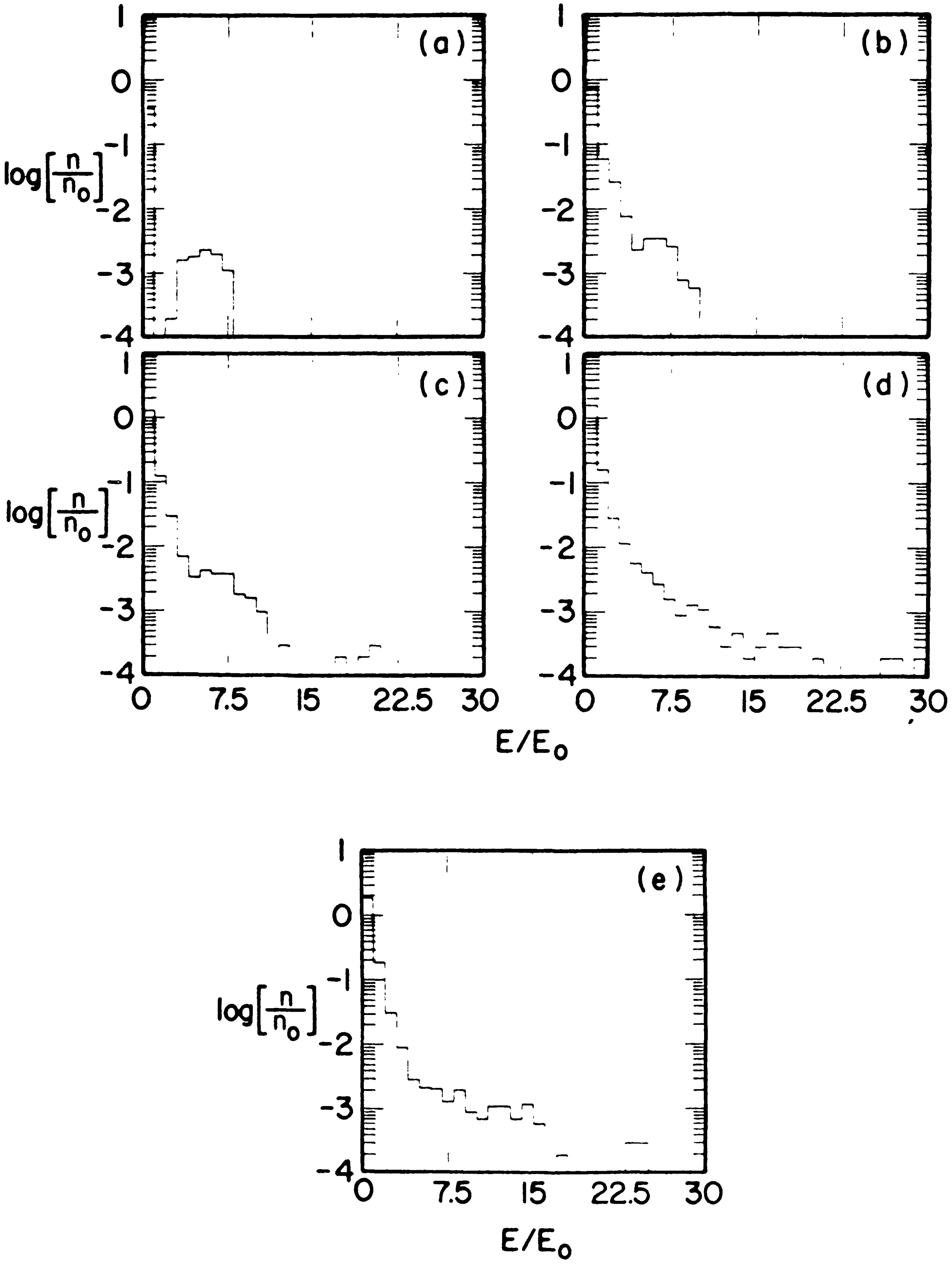

Fig. 27. Ion energy spectra at five times during a simulation run ($t = 0$, 3.68, 6.84, 8.64, and $10.44\Omega_i^{-1}$ for (a)–(e)) where two identical shocks, for which $\theta_1 = 45°$, $\beta_i = \beta_e = 1$, and $M_{A1} = 8$, propagate along the x-axis and collide head-on at about $t = 6.84\Omega_i^{-1}$ (from Cargill and Goodrich, 1987).

following the collision, these cases accelerate ~3% of ions beyond $E/E_0 = 4$, while at $\theta_1 = 45°$, ~2% are accelerated beyond $E/E_0 = 4$. However, the maximum energy increases from ~10 at $\theta_1 = 90°$ to ~20 at $\theta_1 = 45°$. The authors emphasize that the $\theta_1 = 45°$ results should be viewed with some caution for two reasons. First, ion-streaming instabilities that can be generated by and, in turn, scatter the reflected ions are possibly not operative in the simulations. Second, to study the collisions using reasonable computer resources, it is necessary to maintain relatively short simulation times (~ few ion gyroperiods). Thus, at $t = 0$ the shocks must already be within an ion gyroperiod or so of colliding. Wider shock separations would allow more time for ions to travel from one shock to the other and possibly reach higher energies before the shocks collide.

As the authors point out, these simulations are relevant to observations of plasma structures and energetic ion distributions made by spacecraft in the outer heliosphere. The interaction between high speed streams from coronal holes and the ambient solar wind produces corotating interaction regions, or CIRs (e.g., Burlaga, 1984). Beyond a few AU, these CIRs are often bounded by forward and reverse quasi-perpendicular shocks that are generally associated with high intensities of energetic ions. Beyond 10 AU or so, the forward shock of one CIR can collide head-on with the reverse shock of a preceding CIR. Assuming supercritical shocks with $U_1 \sim 200$ km s^{-1}, this implies that such collisions should be capable of accelerating protons from thermal energies to at least ~10–$20E_0$, or, ~2 to 4 keV. These protons represent a seed population for further acceleration by the drift and first-order Fermi processes at either of the colliding shocks, or at subsequent shocks.

6. Summary

We have reviewed the basic techniques and results of computer models used in the study of charged particle acceleration at oblique fast-mode shocks. Our emphasis was upon numerical codes that numerically integrate along the exact phase-space orbits of test particles. In Sections 3 and 4 we covered the acceleration of energetic particles at planar, infinitesimally thin shocks, and in Section 5 we reviewed examples of plasma simulations where low-energy ions are injected and accelerated at quasi-perpendicular shocks with internal structure.

Section 3 reviewed the case where both the electric and magnetic fields are static and uniform on both sides of the shock. Particles are accelerated by the scatter-free drift process at a single shock encounter. We showed how drift-associated energy and pitch angle changes as observed from either the shock or plasma frames vary with the shock angle θ_1. Results from numerical orbit integrations were shown to compare well with theoretical expressions based upon magnetic moment conservations, for $0° \leq \theta_1 \leq 90°$. Some basic results at quasi-perpendicular shocks are as follows.

(1) Energy gains and pitch angle changes are largest when the speed of incident particles, v_0, is comparable to the de Hoffmann-Teller speed, $V_1 = U_1 \sec \theta_1$. For $(v_0/c)^2 \ll 1$, peak fractional energy gains $(\Delta E/E_0)_m$ are about $4(r - 1)$ for reflected

particles, $2(r-1)$ for particles transmitted downstream, and somewhat less than this for those transmitted upstream (r = shock compression ratio). At perpendicular shocks ($\theta_1 = 90°$), or at quasi-perpendicular shocks for which $v_0 < r^{1/2} V_1$, all particles are transmitted downstream, and $(\Delta E/E_0)_m \simeq r - 1$.

(2) Particles can be reflected upstream only if their post-acceleration energy E exceeds the de Hoffmann-Teller energy $E_1 = mV_1^2/2$. Consequently, intensity peaks will shift from downstream to upstream as E increases from below to above E_1.

(3) Upstream, accelerated distributions exhibit large field-aligned, anti-shockward anisotropies. Downstream, peak intensities shift from shockward along the field at low energies ($E \gtrsim E_1$) to perpendicular to the field at high energies ($E \gg E_1$).

(4) Large intensity increases at a given energy can result from a single, scatter-free drift encounter if the energy spectrum of the ambient population below that energy has a large negative slope.

In Section 4 we reviewed how drift acceleration at a single encounter is modified when magnetic fluctuations are introduced. The fluctuations perturb particle drift orbits, causing a small fraction of particles to undergo episodes of intensive drift, and thereby gain much more energy in a single encounter. As compared with a single shock encounter in the scatter-free case, the inclusion of magnetic fluctuations at a quasi-perpendicular shock (1) increases the transmission of particles incident from upstream, (2) produces broader energy distributions with power-law tails extending to several times the peak energy gained in the scatter-free case, (3) reduces anisotropies near the shock, but does not eliminate them, and (4) destroys the invariance of the magnetic moment that is so useful in the scatter-free limit. For a single shock encounter at a quasi-parallel shock, we showed that average energy gains and the fraction of reflected particles increase with increasing levels of magnetic fluctuations.

In Section 4 we also reviewed the modeling of multiple shock encounters at oblique shocks. These models incorporate the drift and first-order Fermi acceleration processes. One study showed that, with all other parameters fixed, the acceleration rate increases dramatically with increasing θ_1. This is in qualitative agreement with theory. It was also shown that as θ_1 is increased from 15° to 75°, the average drift energy change remains positive and increases monotonically, which is contrary to theoretical predictions that the average drift energy change should become negative in the quasi-parallel regime. We also discussed how energy spectra derived from the modeling of $\theta_1 = 0°$ and 60° shocks compared with estimates derived from diffusive shock acceleration theory. The modeled and calculated spectral slopes and maximum energy gains were in reasonable agreement. It was suggested that such comparisons need to be performed for obliquities closer to 90°.

In Section 5 we discussed results from a simulation that used the time- and spatially-varying shock fields generated by a 1-D hybrid code to study the drift acceleration of low energy ($\gtrsim 1$ keV) protons at quasi-perpendicular shocks. It was shown that drift acceleration remains operative down to injection energies normally classified as superthermal. We also reviewed recent theoretical and numerical work concentrating on the $\mathbf{V}_p \times \mathbf{B}$ acceleration of ions at perpendicular and nearly perpendicular shocks. It has been shown that thermal ions can be resonantly accelerated in the cross-shock electric field to relatively high energies. The third example we discussed involved simulations of two supercritical, quasi-perpendicular shocks colliding head-on. This situation, which is probably rather common in the outer heliosphere, can accelerate ions to superthermal energies, thereby providing an essential seed population available for further shock acceleration.

There are several problems in shock-acceleration physics where computer modeling could play a major role. One of these, which was discussed in Section 4.5, is the theoretical prediction that the acceleration rate will rise rapidly with increasing θ_1 and peak at $\theta_1 = 90°$, provided the process is diffusive (Jokipii, 1987, 1988). However, on a more practical level, there is the question of whether shocks with $\theta_1 \lesssim 90°$ can support a spectrum of upstream waves produced, for example, by reflected ion beams and, therefore, maintain quasi-isotropic particle distributions. As discussed in Section 4.3, *in situ* observations indicate that this is unlikely, although more observations at higher resolution are needed to resolve this issue. Thus, unless the level of ambient magnetic fluctuations is sufficiently high, shocks with $\theta_1 \lesssim 90°$ will be unable to accelerate ions diffusively. Chiueh has investigated ion acceleration at a nearly perpendicular shock devoid of upstream turbulence. He showed theoretically (Chiueh, 1988b) and through numerical modeling (Chiueh, 1988a) that ions can undergo multiple-encounter acceleration if low-frequency, compressional MHD turbulence exists downstream of the shock. More work in this area is necessary to determine the characteristics of the ion energy spectrum.

Another area where much more work is needed is in comparing spacecraft observations with modeling predictions. The advantage of the modeling is that one can handle time-dependent acceleration at oblique shocks for particle injection energies and levels of turbulence not amenable to theoretical analysis. Murtha (1988) used data from the interplanetary probes Voyagers 1 and 2 to analyze energy spectra and pitch angle distributions of ions from 30 keV to 4 MeV during quasi-perpendicular shock events at ~ 5 AU. The anisotropies observed near the shock crossings compared well with results from multiple-encounter computer modeling that used as input the observed plasma parameters and levels of magnetic fluctuations.

The modeling can also help resolve questions concerning the parameter range within which theory is valid. For example, how do particle pitch angle distributions evolve with distance from the shock as a function of particle energy, shock obliquity, and amplitude of magnetic fluctuations? Under what conditions is the 'diffusive limit' realized? What happens to the acceleration process when the amplitude of fluctuations is extremely large? Under this condition we expect that particles will be strongly scattered and that the shock obliquity will fluctuate wildly. Drury (1987) has predicted that in the limit of strong scattering, there are no new effects beyond those expected from the standard theory of diffusive acceleration at oblique and perpendicular shocks; rather, new effects should occur for weak scattering at highly oblique shocks. Is this assertion true, and if so, what are these new effects and how weak must the scattering be for these effects to manifest themselves? How do ion composition ratios evolve at oblique shocks when different ion species are accelerated under conditions that are intermediate between the scatter-free and diffusive limits?

Acknowledgements

This work was supported in part by NASA grant NSG-7055, in part by Task I of Navy contraxt N00039-87-C-5301, and in part by NSF grant ATM-861135. I am grateful to Drs T. P. Armstrong, M. A. Forman, R. E. Gold, S. M. Krimigis, M. E. Pesses, E. C. Roelof, E. T. Sarris, and L. Vlahos for helpful discussions on various aspects of shock acceleration.

References

Achterberg, A. and Blandford, R. D.: 1986, *Monthly Notices Roy. Astron. Soc.* **218**, 551.
Alekseyev, I. I. and Kropotkin, A. P.: 1970, *Geomagnetizm Aeronomiya* **10**, 755 (English transl.).
Anagnostopoulos, G. C. and Sarris, E. T.: 1983, *Planetary Space Sci.* **31**, 689.
Armstrong, T. P., Chen, G., Sarris, E. T., and Krimigis, S. M.: 1977, in M. A. Shea and D. F. Smart (eds.), *Study of Traveling Interplanetary Phenomena*, D. Reidel Publ. Co., Dordrecht, Holland, p. 367.
Armstrong, T. P., Krimigis, S. M., and Behannan, K. W.: 1970, *J. Geophys. Res.* **75**.
Armstrong, T. P., Pesses, M. E., and Decker, R. B.: 1985, in B. T. Tsurutani and R. G. Stone (eds.), *Collisionless Shocks in the Heliosphere: Reviews of Current Research* (*Geophys. Monogr. Ser.* **35**, 271).
Axford, W. I.: 1981, *Proc. 17th Int. Cosmic Ray Conf. (Paris)* **12**, 155.
Axford, W. I.: 1987, in K. Szegö (ed.), *Proceedings of the International Conference on Collisionless Shocks*, Central Research Institute for Physics of the Hungarian Academy of Sciences, p. 296.
Balogh, A. and Erdös, G.: 1981, *Proc. 17th Int. Cosmic Ray Conf. (Paris)* **3**, 438.
Balogh, A. and Erdös, G.: 1985, *Proc. 19th Int. Cosmic Ray Conf. (La Jolla)* **4**, 178.
Bell, A. R.: 1978a, *Monthly Notices Roy. Astron. Soc.* **182**, 147.
Bell, A. R.: 1978b, *Monthly Notices Roy. Astron. Soc.* **182**, 443.
Bendat, J. S. and Piersol, A. G.: 1971, *Random Data: Analysis and Measurement Procedures*, Interscience, New York.
Blandford, R. and Eichler, D.: 1987, *Phys. Reports* **154**, 1.
Boyd, T. J. M. and Sanderson, J. J.: 1969, *Plasma Dynamics*, Barnes and Nobe, New York.
Brinca, A. L.: 1984, *J. Geophys. Res.* **89**, 115.
Burgess, D.: 1987a, *Ann. Geophys.* **5**, 133.
Burgess, D.: 1987b, *J. Geophys. Res.* **92**, 1119.
Burlaga, L.: 1984, *Space Sci. Rev.* **39**, 255.
Cargill, P. J. and Goodrich, C. C.: 1987, *Phys. Fluids* **30**, 2504.
Carnahan, N., Luther, H. A., and Wilkes, J. O.: 1969, *Applied Numerical Methods*, Wiley and Sons, Inc., New York.
Chen, G.: 1975, Ph.D. Thesis, University of Kansas.
Chiueh, T.: 1988a, in V. J. Pizzo, T. E. Holtzer, and D. G. Sime (eds.), *Proceedings of the Sixth International Solar Wind Conference, II*, NCAR/TN-306 + Proc., p. 497.
Chiueh, T.: 1988b, *Astrophys. J.* **333**, 366.
Colburn, D. S. and Sonett, C. P.: 1966, *Space Sci. Rev.* **5**, 439.
Decker, R. B.: 1981, *J. Geophys. Res.* **86**, 4537.
Decker, R. B.: 1983, *J. Geophys. Res.* **88**, 9959.
Decker, R. B.: 1987, in K. Szegö (ed.), *Proceedings of the International Conference on Collisionless Shocks*, Central Research Institute for Physics of the Hungarian Academy of Sciences, p. 224.
Decker, R. B.: 1988, *Astrophys. J.* **324**, 566.
Decker, R. B., Pesses, M. E., and Krimigis, S. M.: 1981, *J. Geophys. Res.* **86**, 8819.
Decker, R. B. and Vlahos, L.: 1985a, *Proc. 19th Int. Cosmic Ray Conf. (La Jolla)* **4**, 10.

Decker, R. B. and Vlahos, L.: 1985b, *J. Geophys. Res.* **90**, 47.

Decker, R. B. and Vlahos, L.: 1986a, *Astrophys. J.* **306**, 710.

Decker, R. B. and Vlahos, L.: 1986b, *J. Geophys. Res.* **91**, 13349.

Decker, R. B., Vlahos, L., and Lui, A. T. Y.: 1984, *J. Geophys. Res.* **89**, 7331.

de Hoffmann, F. and Teller, E.: 1950, *Phys. Rev.* **80**, 692.

Drury, L. O'C.: 1983, *Rep. Progr. Phys.* **46**, 973.

Drury, L. O'C.: 1987, *Proc. 20th Int. Cosmic Ray Conf. (Moscow)* **2**, 161.

Dryer, M., Smith, Z. K., Unti, T., Mihalov, J. D., Smith, B. F., Wolfe, D. S., Colburn, D. S., and Sonett, C. P.: 1975, *J. Geophys. Res.* **80**, 3225.

Earl, J. A.: 1974, *Astrophys. J.* **193**, 231.

Edmiston, J. P. and Kennel, C. F.: 1984, *J. Plasma Phys.* **32**, 429.

Eichler, D.: 1981, *Astrophys. J.* **244**, 711.

Ellison, D. C.: 1981, Ph.D. Thesis, Catholic University of America.

Ellison, D. C. and Eichler, D.: 1984, *Astrophys. J.* **281**, 691.

Forman, M. A. and Webb, G. M.: 1985, in P. G. Stone and B. T. Tsurutani (eds.), *Collisionless Shocks in the Heliosphere: A Tutorial Review* (*Geophys. Monogr. Ser.* **34**, 91).

Gary, S. P.: 1985, *Astrophys. J.* **288**, 342.

Gary, S. P., Gosling, J. T., and Forslund, D. W.: 1981, *J. Geophys. Res.* **86**, 6691.

Grazis, P. R., Lazarus, A. J., and Hester, K.: 1985, *J. Geophys. Res.* **90**, 9457.

Greenstadt, E. W. and Mellott, M. M.: 1985, *Geophys. Res. Letters* **12**, 129.

Hedgecock, P. C.: 1975, *Solar Phys.* **42**, 497.

Helfer, H. L.: 1952, *Astrophys. J.* **117**, 177.

Hoppe, M. M., Russell, C. T., Frank, L. A., Eastman, T. E., and Greenstadt, E. W.: 1981, *J. Geophys. Res.* **86**, 4471.

Hudson, P. D.: 1965, *Monthly Notices Roy. Astron. Soc.* **131**, 23.

Jokipii, J. R.: 1971, *Rev. Geophys. Space Phys.* **9**, 27.

Jokipii, J. R.: 1982, *Astrophys. J.* **255**, 716.

Jokipii, J. R.: 1987, *Astrophys. J.* **313**, 842.

Jokipii, J. R.: 1988, in V. J. Pizzo, T. E. Holtzer, and D. G. Sime (eds.), *Proceedings of the Sixth International Solar Wind Conference*, Vol. II, NCAR/TN-306 + Proc., p. 481.

Kantrowitz, A. R. and Petschek: 1966, in W. B. Kunkel (ed.), *Plasma Physics Theory and Application*, McGraw-Hill, New York.

Kennel, C. F., Scarf, F. L., Coroniti, F. V., Russell, C. T., Wentzel, K.-P., Sanderson, T. R., van Nes, P., Feldman, W. C., Parks, G. K., Smith, E. J., Tsurutani, B. T., Mozer, F. S., Temerin, M., Anderson, R. R., Scudder, J. D., and Scholer, M.: 1984, *J. Geophys. Res.* **89**, 5419.

Kennel, C. F., Edmiston, J. P., and Hada, T.: 1985, in R. G. Stone and B. T. Tsurutani (eds.), *Collisionless Shocks in the Heliosphere: A Tutorial Review* (*Geophys. Monogr. Ser.* **34**, 1).

Kessel, R. L.: 1986, Ph.D. Thesis, University of Kansas.

Kirk, J. G. and Schneider, P.: 1987, *Astrophys. J.* **322**, 1987.

Krimigis, S. M., 1987, in K. Szegö (ed.), *Proceedings of the International Conference on Collisionless Shocks*, Central Research Institute for Physics of the Hungarian Academy of Sciences, p. 3.

Lee, M. A.: 1982, *J. Geophys. Res.* **87**, 5063.

Lee, M. A.: 1983, *Rev. Geophys. Space Phys.* **21**, 324.

Lee, M. A. and Lerche, I.: 1974, *Rev. Geophys. Space Sci.* **12**, 671.

Legage, P. O. and Cesarsky, C. J.: 1983, *Astron. Astrophys.* **125**, 249.

Leroy, M. M. and Winske, D.: 1983, *Ann. Geophys.* **1**, 527.

Leroy, M. M., Winske, D., Goodrich, C. C., Wu, C. S., and Papadopoulos, K.: 1982, *J. Geophys. Res.* **87**, 5081.

Matthaeus, W. H. and Goldstein, M. L.: 1982, *J. Geophys. Res.* **87**, 6011.

McKenzie, J. F. and Westphal, K. O.: 1969, *Planetary Space Sci.* **17**, 1029.

Murtha, J.: 1988, M. S. Thesis, University of Calgary (in preparation).

Ohsawa, Y.: 1986a, *Phys. Fluids* **29**, 773.

Ohsawa, Y.: 1986b, *Phys. Fluids* **29**, 1844.

Ohsawa, Y.: 1987, *Geophys. Res. Letters* **14**, 95.

Ohsawa, Y. and Sakai, J.: 1987, *Astrophys. J.* **313**, 440.

Ostrowski, M.: 1988, *Monthly Notices Roy. Astron. Soc.* **233**, 257.

Owens, A. J.: 1978, *J. Geophys. Res.* **83**, 1673.
Papadopoulos, K.: 1985, in R. G. Stone and B. T. Tsurutani (eds.), *Collisionless Shocks in the Heliosphere: A Tutorial Review* (*Geophys. Monogr. Ser.* **34**, 59).
Parker, E. N.: 1958, *Phys. Rev.* **109**, 1328.
Pesses, M. E.: 1979, Ph.D. Thesis, University of Iowa.
Pesses, M. E.: 1981, *J. Geophys. Res.* **86**, 150.
Pesses, M. E. and Decker, R. B.: 1986, *J. Geophys. Res.* **91**, 4173.
Pesses, M. E., Decker, R. B., and Armstrong, T. P.: 1982, *Space Sci. Rev.* **32**, 185.
Pesses, M. E., Van Allen, J. A., Tsurutani, B. T., and Smith, E. J.: 1984, *J. Geophys. Res.* **89**, 37.
Potter, D. W.: 1981, *J. Geophys. Res.* **86**, 11111.
Ptuskin, V. S.: 1985, *Proc. 19th Int. Cosmic Ray Conf. (La Jolla)* **9**, 215.
Quenby, J. J.: 1986, *Mitteilungen der Astronomischen Gesellschaft* **65**.
Russell, C. R. and Greenstadt, E. W.: 1979, *Space Sci. Rev.* **23**, 3.
Russell, C. T. and Hoppe, M. M.: 1983, *Space Sci. Rev.* **34**, 155.
Russell, C. T., Smith, E. J., Tsurutani, B. T., Gosling, J. T., and Bame, S. J.: 1982, in M. Neugebauer (ed.), NASA Conf. Publ. 2280, p. 385.
Sakai, Y. and Ohsawa, J.: 1987, *Space Sci. Rev.* **46**, 113.
Sanderson, T. R.: 1984, *Adv. Space Res.* **4**, 305.
Sanderson, T. R., Reinhard, T., Van Nes, P., and Wentzel, K.-P.: 1985, *J. Geophys. Res.* **90**, 19.
Sarris, E. T. and Krimigis, S. M.: 1985, *Astrophys. J.* **298**, 676.
Sarris, E. T. and Van Allen, J. A.: 1974, *J. Geophys. Res.* **79**, 4157.
Sarris, E. T., Krimigis, S. M., and Armstrong, T. P.: 1976, *J. Geophys. Res.* **81**, 4689.
Schatzman, E.: 1963, *Ann. Astrophys.* **26**, 234.
Scholer, M.: 1985, in B. T. Tsurutani and R. G. Stone (eds.), *Collisionless Shocks in the Heliosphere: Reviews of Current Research* (*Geophys. Monogr. Ser.* **35**, 271).
Scholer, M.: 1988, in V. J. Pizzo, T. E. Holtzer, and D. G. Sime (eds.), NCAR/TN-306 + Proc., p. 465.
Schwartz, S. J., Thompsen, M. F., and Gosling, J. T.: 1983, *J. Geophys. Res.* **88**, 2039.
Sentman, D. D., Kennel, C. F., and Frank, L. A.: 1981, *J. Geophys. Res.* **86**, 4365.
Shabanskii, V. P.: 1962, *J. Experim. Theor. Phys.* **41**, 1107.
Singer, S. and Montgomery, M. D.: 1971, *J. Geophys. Res.* **76**, 6628.
Siscoe, G. L.: 1983, in R. L. Carovillano and J. M. Forbes (eds.), *Solar-Terrestrial Physics*, D. Reidel Publ. Co., Dordrecht, Holland, p. 11.
Sonnerup, B. U. Ö.: 1969, *J. Geophys. Res.* **74**, 1301.
Terasawa, T.: 1979, *Planetary Space Sci.* **27**, 193.
Tidman, D. A. and Krall, N. A.: 1971, *Shock Waves in Collisionless Plasmas*, Wiley and Sons, Inc., New York.
Toptyghin, I. N.: 1980, *Space Sci. Rev.* **26**, 157.
Tsurutani, B. T., Smith, E. J., and Jones, D. E.: 1983, *J. Geophys. Res.* **88**, 5045.
Van Nes, P., Reinhard, R., Sanderson, T. R., Wentzel, K.-P., and Zwickl, R. D.: 1984, *J. Geophys. Res.* **89**, 2122.
Vandas, M., Fischer, S., Lutsenko, V. N., Kudela, K., Slivka, M., Němeček, Z., and Šafránková, J.: 1986, *Adv. Space Res.* **6**, 49.
Vandas, M.: 1987, in K. Szegö (ed.), *Proceedings of the International Conference on Collisionless Shocks*, Central Research Institute for Physics of the Hungarian Academy of Sciences, p. 83.
Vasilÿev, V. N., Toptyghin, I. N., and Chirkov, A. G.: 1978, *Geomagnetism i Aeronomiya* **18**, 279 (Engl. transl.).
Webb, G. M., Axford, W. I., and Terasawa, T.: 1983, *Astrophys. J.* **270**, 537.
Wentzel, D. G.: 1974, *Ann. Rev. Astron. Astrophys.* **12**, 71.
Whipple, E. C., Northrop, T. G., and Birmingham, T. J.: 1986, *J. Geophys. Res.* **91**, 4149.
Winske, D.: 1985, *Space Sci. Rev.* **42**, 53.
Winske, D. and Leroy, M. M.: 1984, *J. Geophys. Res.* **89**, 2673.
Wu, C. S.: 1984, *J. Geophys. Res.* **89**, 8857.